UNIVERSITÀ DEGLI STUDI DI PADOVA

Dipartimento di Ingegneria Industriale

SCUOLA DI DOTTORATO DI RICERCA IN INGEGNERIA INDUSTRIALE
INDIRIZZO IN INGEGNERIA ELETTROTECNICA
CICLO XXV

Multi Polar Direct Drive Permanent Magnet Synchronous Machines for Renewable Energy

Direttore della Scuola:
Ch.mo Prof. Paolo Colombo ....

Coordinatore d'indirizzo:
Ch.mo Prof. Giovanni Martinelli ....

Supervisore:
Ch.mo Prof. Nicola Bianchi ....

Dottorando: Alessandro Fasolo

....

Co-Tutors:

Ing. Matteo Casazza   Head of Research and Development Leitwind SpA

Ing. Georg Folie   Leader of Generator Development Leitwind SpA

A chi mi ha insegnato
la tenacia nella vita
in questi tre anni

True progress is that which
places technology in
everyone's hands

Henry Ford

There is plenty of energy,
the problem is to sell it
with the right price...

Otto Pabst

... our duty is to use energy
that Earth gives us, with the
consciousness to respect Her

own reflection

Contents

Sommario

*Questa introduzione colloca brevemente questo studio nello scenario delle energie rin-
novabili. La necessità di progettare macchine elettriche per una conversione elettromec-
canica sostenibile è posta in evidenza. I contenuti della tesi e i suoi principali contributi
sono poi descritti.*

Scenario

Il grande sviluppo industriale avvenuto nell'ultimo secolo ha portato all'attuale con-
dizione globale, dove i Paesi Sviluppati hanno creato lo status tecnologico moderno.
I principali modelli cui si riferisce l'attuale società globale sono l'Europa e gli Stati
Uniti. Negli ultimi due decenni lo sviluppo di nuove realtà come Cina, India e altri
Paesi asiatici ha contribuito alla determinazione (ancora in via di sviluppo) di una so-
cietà globale in cui le Aziende trovano il loro mercato.
L'energia gioca un ruolo chiave in questa situazione, perchè il consumo globale continua
a crescere. La risorsa energetica tutt'ora preponderante a livello mondiale è il petrolio,
largamente impiegato nell'Industria, nei Trasporti e nella generazione di energia elet-
trica.

Vi sono principalmente due grandi svantaggi nell'elevato livello attuale di consumo
di petrolio:

- il livello di inquinamento prodotto sta danneggiando la Terra seriamente, a causa
  del ben noto Effetto Serra e del riscaldamento globale. La sostenibilità della vita
  sulla Terra è seriamente compromessa e affatto garantita per le generazioni future;

- il prezzo del petrolio cresce sempre di più. Questo è un problema per le attività
  economiche mondiali e per la popolazione: i vantaggi della tecnologia sono limitati
  a un numero sempre più esiguo di persone.

Conformemente alle richieste del mercato e della tecnologia l'energia è venduta in
gran parte sotto forma di elettricità, quindi la conversione elettromeccanica dalle fonti
primarie è un aspetto cruciale per la società globale nell'affrontare i problemi di una
vita sostenibile e dell'accessibilità alla tecnologia. Risulta quindi fondamentale l'utilizzo

di fonti primarie che non inquinino o che inquinino meno del petrolio. L'efficienza della conversione da queste fonti deve essere elevata in modo da ridurre il consumo globale di energia e migliorarne la generazione. La Normativa Internazionale e i clienti delle Aziende del settore richiedono la capacità di costruire macchine elettriche sempre più efficienti.

Una politica globale determinata a promuovere queste fonti alternative tutt'ora in crescita è la risposta ai problemi dell'inquinamento, della razionalizzazione dei consumi e dell'accessibilità alla tecnologia da parte di tutte le persone.

Diversi Governi, sia in Europa che negli Stati Uniti hanno sostenuto le Energie Rinnovabili con politiche di sviluppo ed incentivi finanziari alla Ricerca in questo campo, portando alla realizzazione concreta di soluzioni tecniche poi commercializzate e prototipali. L'Energia Eolica in particolare è cresciuta durante gli ultimi vent'anni ed è ora una grande realtà. Anche l'Energia Solare si è considerevolmente sviluppata. Altri esempi di Energie Rinnovabili sono la Fonte Geotermica e l'Energia Marina. Quest'ultimo tipo di Energia esiste in forma di moto ondoso, maree, correnti marine, gradiente termico o salino.

Motivazioni della tesi

Questo lavoro di dottorato considera principalmente la Risorsa Eolica e si focalizza sulle caratteristiche elettromagnetiche dei generatori a presa diretta per questa applicazione. Malgrado molti Costruttori di turbine eoliche usino configurazioni comprendenti il moltiplicatore di giri, la presenza di quest'organo di trasmissione causa una perdita di efficienza del sistema elettromeccanico che va a comprometterne la sostenibilità.

Una soluzione multipolare a bassa velocità di rotazione e presa diretta tra generatore e pale della turbina è quindi adottata. Si sceglie l'utilizzo del magnete permanente grazie alla sua compattezza e all'assenza di spazzole in paragone alle soluzioni di macchina sincrona tradizionale. L'avvolgimento frazionario è adottato per risparmiare materiale nell'avvolgimento di armatura della macchina.

Questo tipo di configurazione presenta evidenti vantaggi come la lunghezza ridotta delle testate, il buon fattore di riempimento delle cave, elevati rendimento e fattore di potenza. Essa si presta inoltre a soluzioni circuitalmente ridondanti che consentono una struttura modulare della parte attiva, con la capacità di tollerare i guasti.

D'altro canto, le armoniche spaziali della forza magneto motrice (MMF) dovuta all'avvolgimento frazionario causano perdite nel rotore di entità notevole.

I metodi tradizionali di calcolo delle perdite (formula di Steinmetz o modelli di corpi solidi in campo magnetico uniforme) non forniscono risultati soddisfacenti per queste perdite. La forza magneto motrice risulta non sincrona con il rotore della macchina, con conseguente indursi di correnti parassite in ogni parte conduttrice del rotore, come nel giogo metallico che sorregge i poli magnetici e nei magneti stessi (terre rare). Le perdite nei magneti ne causano il riscaldamento, con conseguente calo delle prestazioni della macchina. La riduzione del campo dei magneti dovuta all'aumento di temper-

atura aumenta il rischio di smagnetizzazione irreversibile.

L'ampiezza delle armoniche spaziali di forza magneto motrice e la loro frequenza vista dal rotore dipendono dalla particolare combinazione cave–poli dell'avvolgimento scelto. L'entità di queste perdite cresce notevolmente con l'aumentare delle dimensioni della macchina, divenendo un aspetto cruciale nella progettazione di macchine multipolari a presa diretta di grande diametro ($\lesssim 2m$) con magnete permanente.

Una scelta adeguata del rapporto cave–poli dell'avvolgimento, significa un notevole miglioramento della sostenibilità del processo di conversione elettromeccanica: le perdite vengono ridotte e il rendimento migliora. Se il rendimento migliora, significa che meno materiale è stato sprecato. Questa parte del lavoro di tesi si è svolta presso il Laboratorio di Azionamenti Elettrici nel Dipartimento di Ingegneria Industriale dell'Università di Padova nell'ambito di un contratto di ricerca voluto da Leitwind SpA (VIpiteno, Italia). Leitwind è un costruttore di turbine eoliche.

Lo scopo è progettare un generatore di grande diametro ($\backsim 4m$) per il prototipo di turbina eolica da 3 MW. Compresa l'importanza del fenomeno delle perdite rotoriche, la volontà di Leitwind è svilupparne calcolo per scegliere l'avvolgimento della nuova macchina. Il generatore Leitwind esitente, denominato LW15C, per la turbina LTW77 (potenza nominale 1.5 MW) è analizzato sia con modelli analitici che con gli elementi finiti. Questo generatore è la base di partenza di questo studio.

Viene applicato un metodo per il calcolo delle perdite rotoriche indotte dall'elevato contenuto armonico dell'avvolgimento frazionario. Le perdite così ottenute sono confrontate con i risultati dell'attività del banco prova su macchine reali.

Con lo stesso approccio si studia e si modella il motore diretto per trazione funiviaria SFA (500 kW di potenza nominale) negli impianti Leitner. Leitner e Leitwind appartengono al Gruppo Leitner Technologies. I risultati del banco prova sono confrontati con i valori calcolati. La progettazione del nuovo generatore LW30A è sviluppata a partire dai modelli creati per il generatore LW15C e il motore diretto SFA.

Vengono poi studiate differenti topologie di macchina a magnete permanente con avvolgimento frazionario per confrontarle con la configurazione switching flux (SFPM). Lo studio prende in considerazione sia magneti di terre rare, che di ferrite. La possibilità di integrare una notevole quantità di magnete nella parte di armatura della macchina SFPM e il principio di concentrazione di flusso portano ad una soluzione con un buon rapporto costi prestazioni, che però deve essere valutata non solo da un punto di vista di prestazioni. La struttura del rotore di questa macchina è semplice e robusta, come per le macchine a riluttanza. Il comportamento della topologia SFPM a smagnetizzazione dei magneti permanenti risulta un punto cruciale da indagare. Per allargare lo studio ad un'altra Fonte Rinnovabile, l'energia da moto ondoso è brevemente descritta e vengono confrontate alcune topologie di generatori lineari per questa applicazione. Uno struttura a doppio statore viene studiata con l'intento di massimizzare la spinta sulla parte mobile. Si considera inoltre l'utilizzo dei magneti in ferrite: malgrado il loro basso prodotto di energia rispetto ai magneti in terre rare, essi risultano meni nocivi per l'ambiente e la salute dell'uomo: il processo di estrazione delle terre rare coinvolge infatti elementi radioattivi, mentre l'estrazione della ferrite è in tutto simile a quella del ferro.

Contributi principali della tesi

I principali contributi di questo lavoro di tesi alla ricerca futura nell'ambito delle energie rinnovabili si possono così sintetizzare:

- L'applicazione del modello a strati e del metodo dei punti corrente nel calcolo delle perdite rotoriche di macchine elettriche a presa diretta di grande diametro, con magneti permanenti. I risultati dell'attività sperimentale su banco prova di grosse macchine reali sono confrontati con i valori calcolati.

- La scelta del numero di poli e di cave nella progettazione di macchine a presa diretta di grande diametro, con avvolgimento frazionario.

- Confronto della macchina switching flux con topologie di macchina note, comprendendo la smagnetizzazione del magnete e l'utilizzo della ferrite, materiale più sostenibile delle terre rare.

- Studio di diverse topologie di generatore lineare per generazione da moto ondoso, includendo la topologia switching flux a doppio statore.

Struttura della tesi

Capitolo 1 : presenta una breve panoramica sull'energia rinnovabile eolica e da moto ondoso e descrive l'azienda Leitwind SpA.

Capitolo 2 : descrive la modellazione e l'analisi delle macchine studiate, sia con metodi analitici che con gli elementi finiti: sono inclusi i risultati dell'attività sul banco prova. I modelli, sviluppati sul generatore LW15 e sul motore SFA sono poi applicati al nuovo generatore LW30A.

Capitolo 3 : affronta la tematica del calcolo delle perdite rotoriche, sviluppando i modello a strati e il metodo dei punti corrente. Viene descritto il calcolo delle perdite rotoriche. Si affronta la validazione dei metodi di calcolo al banco prova.

Capitolo 4 : ricava una legge di scala per le perdite rotoriche per macchine a magnete permanente ad avvolgimento frazionario.

Capitolo 5 : presenta la scelta del rapporto cave–poli nel progetto del nuovo generatore LW30A per la turbina da 3.0 MW LTW 101. Viene investigata la possibilità di applicare l'Indice delle Perdite Rotoriche, ricavato dal modello a strati.

Capitolo 6 : confronta diverse topologie di macchine ad avvolgimento frazionario con la configurazione switching flux, sia con terre rare che con ferrite. Si affronta il fenomeno della smagnetizzazione sulle diverse topologie di macchina.

Capitolo 7 : prende in considerazione topologie di macchina lineare per conversione da moto ondoso. Include la configurazione switchng flux a doppio statore.

Introduction

This introduction briefly places this study within the world energy scenario. The necessity to design high efficiency electrical machines for a sustainable electromechanical conversion is highlighted. Then, the motivation of the thesis and the main contributions are described.

Scenario

The large development of Industry, which has occurred in the last century, has led to a global situation, where the so called Developed Countries have created the technology status, which is typical of the modern society. Main models of this society are Europe and US.

In the last two decades, the development of new Countries like China, India, and other Asian countries has led to an economic scenario where companies find their market and their competitors.

Energy plays a key-role in this situation, because the global consumption keeps growing. The most employed world source of energy is oil. Petrol is largely used in Industry, transport, and generation of electrical energy.

There are two main drawbacks using oil as primary energy carrier:

- the high pollution level, which is produced by oil is damaging the Earth, due to the well-known greenhouse effect and global warming. The sustainability of life on Earth is gravely compromised and it does not guarantee next generations at all;

- the price of petrol is constantly increasing. This is a problem for the economical activities worldwide and for population: the advantages of technology will be accessible to an increasingly smaller number of people.

According the to the technology and market requirements, energy is largely sold in form of electricity. Thus,the conversion from primary sources is a crucial aspect of the global society facing the sustainability of life on Earth and accessibility to technology. It appears crucial to use more and more primary sources which potentially generates no pollution, or less pollution than oil. The conversion from those sources must be

increased in order to reduce the global energy consumption and improve energy generation.

If the electromechanical conversion of energy is considered international standards and customers require that industries produce more and efficient electrical machines. A strong global policy is necessary to promote new primary sources, to reduce the pollution and to rationalize the energy consumption worldwide, with the aim that a larger number of people may rightly have their little piece of progress. Many Governments in Europe and in the U.S. have supported renewable energies. Financial aids have been implemented to support research in this field. Companies have been supported as well to encourage the construction of prototypes and to develop the market with renewable energy sources.

In particular, the wind energy has grown during the last decades and it is now a big reality. Solar energy has considerably developed as well. Other examples of renewable energies are geothermal energy and marine (or ocean) energy.

This last type of energy exists in the forms of wave, tidal, marine currents, thermal (temperature gradient) and salinity difference.

Motivation of the thesis

This doctoral study mainly considers the Wind Energy resource and focuses on the electromagnetic aspects of generators for direct drive solutions in this field. Despite the strong employing by many constructor of geared technology in Wind Turbines Generators, a transmission/gear box reduces both, efficiency and reliability: the losses due to the transmission potentially compromise the sustainability of the electromechanical system.

A better solution is the multipolar low–speed direct drive train. Permanent magnet machines offer compactness and the absence of brushes with respect to traditional machines. Material in the armature can be saved using fractional slot windings. This type of machine exhibits many advantages such as short end windings, high slot fill factor, high efficiency and power density together with electrical redundancy, which allows the modularization of the active part and fault-tolerance capabilities. However, space harmonics of the magneto-motive force (MMF) in fractional slot windings lead to considerable rotor losses. The computation of these losses according to standard procedures (e.g. Steinmetz equation or models for massive body within homogeneous field) is not satisfactory.

The MMF harmonics move asynchronously with respect to the rotor, inducing currents in any conductive rotor parts, e.g. the metallic iron yoke which supports the magnetic poles and the rare earth permanent magnets (PMs), acting on their working temperature which is strictly related to the performance of PMs. The reduction of the residual flux density causes a decrease both in the back electromotive force (EMF) and in the electromagnetic torque. The reduction of the magnetic field increases the risk of an irreversible demagnetization of the PMs.

The MMF space harmonic amplitude and frequency depend on the particular combination of number of slots and poles. The amount of such losses increases dramatically with the size of the machine becoming a crucial aspect in the design of a large diameter ($\smile 2 - 3m$) multipolar direct drive generators with PMs. A proper selection of the winding of the machine, fixing the number of slot and poles represents an improvement

in the sustainability of the electromechanical conversion process: losses are limited and a higher efficiency is achieved. If efficiency is better even less active material is wasted. This part of the doctoral study has been accomplished at the Electric Drives Laboratory at the Department of Industrial Engineering of the University of Padova during a partnership with Leitwind A.G.(in Sterzing, Italy), which operates in the Wind Energy Market.

The aim is to design a large diameter generator ($\backsim 4m$), which will be employed in the prototype of a 3 MW wind turbine.

The will of Leitwind to implement a method to predict rotor losses in large machines with permanent magnet and fractional slot windings is the key basic point to be solved. The existing LW15C generator for LTW77 (1.5 MW rated power) wind turbine is analyzed by means of analytical relations and finite elements: it represents the starting point of this study. A method to calculate rotor losses due to the high harmonic contents of the fractional slot winding is applied. Such estimated losses are then compared with the results of experimental test benches with "full-scale" prototypes. The same study is then repeated on SFA motor (500 kW rated), employed in ropeways transport in Leitner A.G. plants. Both Leitner and Leitwind belong to the Leitner Technologies Group. Test bench results are finally compared with the values from the analysis. Starting from both the experience on LW15C generator and SFA motor the design of LW30A prototype generator for Leitwind 3MW wind turbine is chosen.

Different topologies of PM machines with fractional slot winding are then investigated and compared with the switching flux configuration (SFPM), both with rare earths and ferrite PMs.

The possibility to integrate a huge magnet quantity in the armature of the SFPM machine and the flux concentration principle can lead to a cost effective solution which must be carefully evaluated without considering the performance of the machine only. The structure of the rotor is robust and simple, like in classical reluctance machines. The robustness against PMs demagnetization is a crucial point to investigate.

To extend the scenario of renewable energy, the wave energy resource is briefly overviewed and some topologies for linear direct drive generator in this field are investigated. In order to increase the thrust density the possibility of employing a double-sided structure is analyzed. The employing of ferrite PMs is also considered: despite their low energy with respect to rare earth magnets they have a lower impact on environment and human health. The extraction process of ferrite is similar to the iron one, while rare earths must be separated from radio elements.

Main contributions of the thesis

To the knowledge of the author, the contributions of this thesis for the upcoming researchers in electrical machines for renewable energy field are:

- The application of straight–lined model and of the current sheet method to calculate rotor losses in large direct drive permanent magnet machines. The results of the test bench activity on real machines are then described and compared with the prediction.

- Selection of number of slots and poles for fractional winding direct drive large generators.

- Comparison of the switching flux machine with other well known machine topologies, including demagnetization behavior and ferrite PMs, more sustainable than rare earth ones.

- Investigation on different linear modules topologies for wave energy, including double–side switching flux topology.

Outline of the thesis

Chapter 1 provides an overview on renewable energy conversion field and presents the company Leitwind A.G.

Chapter 2 describes the analysis and modeling of the LW15C generator for 1.5 MW wind turbine. Then a similar study has been performed for the SFA motor for ropeways applications. Both analytical and finite elements model have been developed/implemented and are compared to the results of experimental test bench activities. The same models are applied to the analysis of the new LW30A generator.

Chapter 3 faces the topic of rotor losses in order to model them with the straight–lined model and the current sheet method. The rotor losses computation is considered and described. Predicted values are compared with the test bench ones.

Chapter 4 establishes a scaling law for rotor losses in fractional slot PM machines.

Chapter 5 provides the selection of the number of slots and poles to design the new LW30A generator for 3.0 MW wind turbine. The validity of the Index of Rotor Losses obtained from the straight–lined model is investigated and applied.

Chapter 6 describes the comparison of fractional winding machine with a small switching flux permanent magnet machine, both with rare earth and ferrite PMs. The demagnetization behavior of the different machine topologies is analyzed.

Chapter 7 considers linear drives for Wave energy conversion with different topologies, including the double–side switching flux machine.

Chapter 1

The Wind and Wave Energy Resource

This chapter briefly introduces the renewable energy resource dealing with wind and wave energy conversion. They contribute to reduce the environmental impact of human activity on Earth in energy conversion. The companies Leitwind A.G. and Leitner A.G. are presented. The future development of the offshore wind energy is going to lead to the employment of wave generators which are actually at a pre-serial stage.

1.1. The Wind Energy Resource

THE wind energy resource has growth more and more in the recent years and gives the possibility to gradually decarbonize the electromechanical conversion of energy in human activities. According to what declared by Danish Energy and Climate Minister Martin Lidegaard in Wind Directions magazine (April 2012):

'Wind energy is a pivotal element in the necessary transition to a green growth economy. The way I see it, decarbonization is a prerequisite to growth. Investments in energy system transformation will drive growth and employment in a wide range of sectors. Every euro spent on the green transition is an investment in European jobs'

The Wind energy and EU climate policy is achieving 30% lower emissions by 2020, as titled by the climate report of the European Wind Energy Association (EWEA). As written by EWEA in this climate report [1] in 2010 the total installed wind power capacity in the EU stood at 84 GW. In a normal wind year this would produce 181 TWh of electricity.
Wind energy production does not emit any greenhouse gases (GHG), unlike coal, gas and oil. Because of the way the electricity market operates, using marginal costs rather than full investment and operation costs, wind energy replaces a mix of gas, coal and oil generation. The European Commission estimates that these three technologies emit on average 696 g CO_2/kWh in 2010. 181 TWh of wind energy production would therefore have avoided a total of 126 million tonnes of CO_2 ($MtCO_2$) in 2010. EWEA's baseline scenario for wind power development to 2020 forecasts 230 GW of installed capacity, producing 581 TWh of electricity and avoiding 342 $MtCO_2$. As a proportion of the EU's emissions reduction target, EU wind energy production should avoid as much as:

- 31% of the EU's 20% emissions reduction target (77% of EU domestic reductions);

- 20% of a potential 30% emissions reduction target (51% of EU domestic reductions).

If the offshore wind energy is considered, 2010 saw strong market development with a much larger number of projects beginning construction than in 2009, under construction, expected to be completed, or completed during the course of the year [2]. The annual energy production (AEP) of an offshore wind plant is potentially greater than the one of an onshore one, thanks to stronger and more constant wind. Fig. 1.1 shows that in the recent years the installed capacity of wind power has remarkably growth, this trend will be maintained according to the forecasts [2,3].
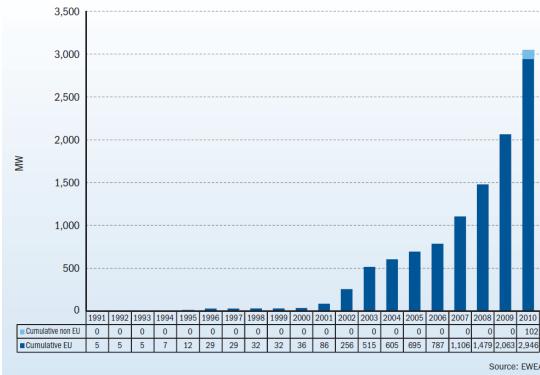
Figure 1.1: Cumulative offshore wind capacity: EU and NON EU (EWEA)

During the first half of 2011 (from 1 January to 30 June), 101 offshore wind turbines were fully grid connected in five wind farms in European waters totalling 348 MW. Total installed capacity at the end of June 2011 reached 3294 MW.
Fig. 1.2 shows the potential of onshore and offshore wind energy according to the upcoming years forecasts [3].
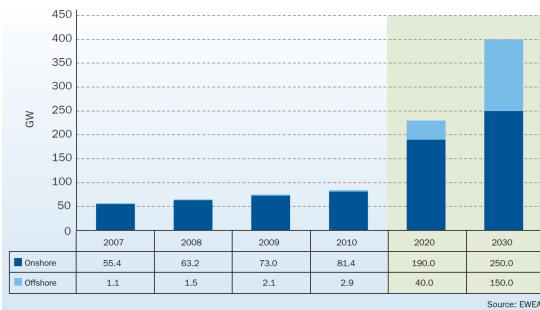
Figure 1.2: Cumulative onshore and offshore wind energy according to the forecasts by EWEA

1.1.1. Technical Challenges In Offshore Wind Energy

Gradually the offshore wind energy could replace the onshore ones, due to the difficult to obtain the permission to install the wind mills on lands. It will be easier to obtain permission to install over square miles of unemployed ocean. The main technical challenges related to the offshore wind energy are:

- reduce the cost, which are still at least double in respect to the onshore plants;

- vessels to transport the building materials and structures;

- fault tolerance, connection to the grid;

- sea environment and corrosion (wave, storm, salinity);

- maintenance, technical availability, reliability;

- building the foundation or the anchoring for the floater of the tower.

Direct drive solutions in offshore wind applications increase the reliability remarkably, due to the absence of the gearbox.

1.2. The Leitner Technologies group

The history of the Leitner technologies group can be found in [4,5] and it's here reported.

In 1888 the Sterzing mechanic Gabriel Leitner set up a workshop in his home town, where he produced agricultural machinery, material ropeways, water turbines and sawmill equipment, and within a hundred years the company developed into a global player in the field of ropeway engineering. The headquarters of today's LEITNER TECHNOLOGIES group still occupy the original site in Sterzing. By 1925 the business had grown from a workshop with just ten employees to a plant for the series production of agricultural machinery. After the 2nd World War, when tourism came to the Alps and generated demand for a modern mountain infrastructure there, the company switched from material to passenger ropeways, and in 1947 LEITNER built its first chairlift in Corvara, Italy.

LEITNER's decision to focus production on the winter mountain infrastructure quickly proved a winner. Agricultural machinery production was discontinued in 1970 and replaced by snow groomer engineering. At the end of the 20th century, the company started to develop new production facilities and agencies outside of Sterzing in other countries, and today LEITNER has works in Austria, France and Colorado in addition to Sterzing as well as over seventy sales and service outlets worldwide. In the meantime there has been rapid progress in ropeway engineering, too. Since 1983 high speed detachable systems have gradually replaced fixed-grip installations; the year 2000 saw the debut of the direct drive for ropeways, and ropeway systems have become a convincing solution to the problem of traffic congestion in urban areas. For that market, LEITNER has developed a rope-hauled light railway system by the name of

MiniMetro. Since 2003 LEITNER has made use of the synergies available from rope-way and wind power engineering to develop the LEITWIND wind turbine, in which the LEITNER direct drive is employed for the generator.

Leitner Group is active worldwide on the markets for ropeways, snow groomers and tracked utility vehicles, urban transportation systems and wind energy. The snowmaking division added at the end of 2010, will provide a complete offering for one-stop shop for all winter-based technologies.

With technological expertise and a clear strategic orientation, the different companies face the challenges of the market on the basis of the corporate values: social responsibility, ethics, quality and growth.

The group reported consolidated sales of 795 million euros in the financial year 2011. In 2011 the group invested 24.8 million euros in R&D and 24.3 million euros in corporate growth and construction of production buildings. In 2011 around 500 new jobs were created, so the headcount for the group reached a new record figure of 3269 employees in the facilities in Europe (Italy, France, Austria, Slovakia, Sweden, Germany), USA, Canada, India and China, and in the 70 subcompanies, 124 selling and service points.

1.2.1. The Company Leitwind A.G.

LEITWIND belongs to the Leitner group, and is presented in [4] as it follows.

The LEITWIND success story starts with ropeways, a core expertise of LEITWIND's parent company HTI. It has evolved from a group of ropeway builders which has, for decades, installed leading-edge technology into spectacular mountain terrain. One of the interesting features of ropeways is the electric direct drive: Its simple, rugged construction has proven its outstanding safety and reliability even in the most extreme conditions.

The LEITWIND success story began with the application of this technology in another, not obviously related, product: the wind turbine. Wind energy holds fascinating potential. But the company group will never launch a product unless it is competitive to all existing solutions. Therefore, LETWIND did not go about building 'some' wind turbine, but 'the' wind turbine.

To this end, the wind turbine was installed with permanent magnet direct drive generator, maximizing performance at all operating levels. The prototype of the first LEITWIND turbine was installed in 2003. In subsequent test runs the concept proved to be superior in every respect from simplified assembly and maintenance to operational reliability and profitability.

Making use of the synergies within the company group, LEITWIND started serial production of onshore wind turbines in 2007. Simplicity, combined with quality, has since convinced customers on three continents. Backed by intra–group synergies, LEITWIND can now offer not only turbines, but also complete wind farm construction as well as operation, maintenance and service packages. The group's synergies help us to cope with a steadily growing demand: producing in Italy, Austria and India, Leitwind has installed around 200 wind turbines on three continents.

In 2011, the company achieved a turnover of 163 million euros. This successful result, achieved through its around 700 skilled employees around the world, is accompanied by a 5.8 million euros investment in research and development. This is a clear indication of the company's special devotion to innovation and quality. 100 wind turbine generators have been installed by the end of 2011. This prestigious goal was successfully achieved by LEITWIND with the construction of wind farms in Europe, Asia and America and a total installed capacity of 138.2 MW.

1.2.2. The New LTW101/104 project

This doctoral thesis has developed within the design of the direct drive generator which is the basis to develop and install the new series of LEITWIND wind turbines with blades diameters of 101 m and 104 m. The design of the new so called LW30A generator (that will be mounted on LTW101 turbine) has been studied in this Phd work.

By completing this new direct drive generator design LEITWIND has enlarged its product portfolio: the new generation of wind turbines called LTW101 and LTW104, assures higher energy yields and improved availability. Hence the company is able to offer improved and superior wind turbines especially for both medium and low wind speed regions. The new turbines operates, like all other LEITWIND turbines, with the proven and patented direct drive technology with a synchronous generator using permanent magnets.

Multi Megawatt turbines are in demand and LEITWIND offers the right product for it. In response to market needs in increasingly powerful wind turbines with higher energy yields and improved availability and profitability, LEITWIND is moving ahead with the development of new turbines: the LTW101, a 3.0 MW wind turbine for medium wind sites and the LTW104 2.0 MW for medium low wind sites, with approx. 3500 full load hours and therefore one of the most efficient turbine on the market. Furthermore the project partner has a choice of two different hub heights, 95 and 143 m. In spite of the significant increase in performance, the turbines have still a compact design and noise levels remain as low as ever.

The first prototype of the LTW101 IIA will be installed this year in Lelystad, Netherlands on the Europeans largest wind turbines test side by the Dutch R&D Institute and Ecofys. Together with the new prototypes of the LTW104, LEITWIND has the right answer for the upcoming market needs. With all its proven wind turbines LEITWIND offers perfect solutions for every environment and wind condition. With nominal power, ranging from 1.0 MW to 3.0 MW, and a broad range of rotor blades and generators, LEITWIND is able to cover every project demand. LEITWIND has successfully installed 200 units worldwide, especially in the core markets Italy and India.

1.3. Wave Energy Conversion

One of the most studied sector of ocean energy is the wave energy. The wind energy has became a technologically consolidated field, where Companies compete adopting a limited number of technical solution.

On the other hand in the wave energy field, there are plenty of different solution which are still object of discussion, prototyping and research, without leading technical alternatives [6, 7]. Recently founding from Governments to ocean energy has been collected again and the research on this field has re-started [8]. This aspect can be related to the growing interest for the Off Shore Wind Power, which allows a bigger annual energy production in respect to the in shore plants [9].

1.3.1. Technical Challenges In Wave Energy

The future development of the Offshore wind energy will lead to an increasing interesting in the wave resource. It will be possible to plan the building and the maintenance or both wind and wave offshore plants which can operate together in order increase the total combined AEP. The main technical challenges related to wave energy are listed (some are in common with the wind energy offshore ones):

- distance from the coast;

- vessels to transport the building materials and structures;

- individuation of solutions with effective technical and commercial reliability;

- fault tolerance, connection to the grid;

- sea environment and corrosion (wave, storm, salinity);

- building a device suitable for staying on the seabed;

- maintenance, technical availability, access to submerge devices;

- building the foundation or the anchoring for the structure.

Direct drive in wave energy means no rotating machines, but linear direct drive modules. From this point of view the direct drive once again is better to reduce the necessity of service in difficult sea environment.

Chapter 2

Modeling Of Machines Under Study

This chapter describes the basic analytical and finite elements computations on the LW15C generator for Leitwind (LTW) LTW77 wind turbine. the prediction of the proposed models are compared with some data of the test bench activity. The same is then done on SFA motor of Leitner Ropeways. All the electrical machines considered are direct drive. It is shown that the models developed are suitable to study the machines considered because there is a good agreement with the results of the test bench activity. The same models are then taken as the base to develop the new LW30A direct drive generator for 3 MW wind turbine.

2.1. The LW15C Direct Drive Wind Generator

THE LW15C generator is used by the Company LTW in LTW77 1.5 MW wind turbine [4]. It is a permanent magnet (PM) synchronous machine with flux concentration and fractional slot winding. The active part of stator and rotor of the LW15C generator is presented in Fig. 2.1 and the general characteristics of the machine are listed in Table 2.1.

Figure 2.1: Active parts of the LW15C generator

Table 2.1: General Characteristics of LW15C Generator

Generator Characteristics	Symbol	Value	Unit
Number of Slots	Q	96	
Number of Poles	$2p$	104	
Number of Phases	m	3	
Stator Outer Diameter	D_{est}	3000	mm
Rated Power	P_{gen}	1575	kW

2.1.1. Analytical Model of the Generator

In this part of the work a simple analytical model of LTW LW15 C generator is used to analyze the machine. This approach will be repeated in the analytical computation of a direct drive motor for Leitner Ropeways and of the new generator for 3 MW wind power plant. The analytical model has been developed in order to have a fast instrument to analyze the machine. The more detailed model will be developed with finite elements. The classical equations used in the computation are shown including the meaning of the symbols for each part of the magnetic circuit of the machine. Some numerical values are not given due to confidentiality.

A master thesis about the model employed [10] has been supervised.

Geometry and material employed in the analytical model

To predict the performance of the LW15C generator, a simplified structure of the magnetic circuit is defined, according to Fig. 2.2. The parameters employed and their values are presented in Table 2.2. Table 2.3 collects the symbols used for the geometrical characteristics of the generator. Some values are given. The data which are presented in Table 2.4 are calculated starting from Table 2.2 and Table 2.3, as shown in the last column.

Table 2.2: General Parameters to Analytical Calculation of Generator

Generator Parameters	Symbol	Value	Unit
Number of Turns per Phase	N_{turns}	29	
Number of Parallels Paths	N_{pp}	4	
Number of Three Phase Systems	N_{line}	2	
Slot Filling Factor	K_{fill}	0.75	
Line Current	I_{line}	936	A
Speed	n	18.2	r/min
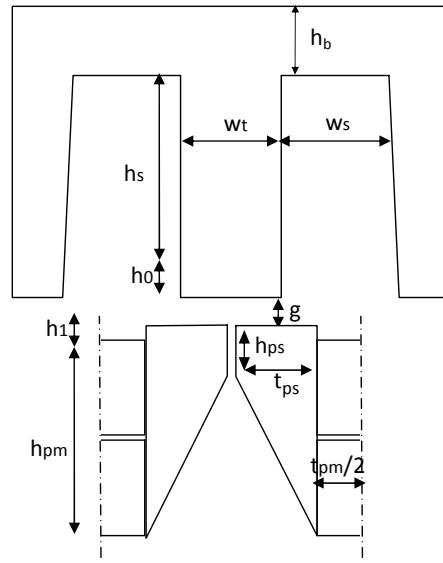
Figure 2.2: Simplified magnetic circuit of the LW15C generator

Table 2.3: General Data to Analytical Calculation of Generator

Geometrical Data	Symbol	Value	Unit
Stator Inner Diameter	D		
Airgap	g		
Width of Slot	w_s		
Height of Slot	h_s		
End Slot Thickness	h_0		
Insulation Thickness	t_{ins}		
Length of Machine	L_{stk}	~ 1000	mm
Inner Diameter of Rotor	D_{ir}		
Outer Diameter of Rotor	D_{gr}		
Length of PM	t_{pm}		
Height of PM	h_{pm}		
Remanence induction	B_{res}	1.09	T
Permeability	μ_{rec}	1.07	
Per Weight Losses (@ 1.5 T 50 Hz)	c_p	5.3	W/kg

Winding Factor and Electrical Load

The electrical load of the machine is used in the analytical calculation of the electromagnetic torque. The winding factor is required and it is possible to obtain it with the star of slot method, as described in [11]. The first step is to calculate the periodicity of the machine t, it is then possible to have the number of strokes of the star of slot and

Table 2.4: Main Generator Data calculated starting from table 2.1

Description	Symbol	Unit	Equation
End Winding Length	L_{ew}	mm	$2.95 \cdot \frac{D}{p}$
Slot Pitch	p_s	mm	$\frac{\pi D}{Q}$
Slot Angle	α_s	°	$\frac{360}{Q}$
Height of Teeth	h_t	mm	$h_s + h_0$
Thickness of Tooth	w_t	mm	$p_s - w_s$
Stator yoke	h_{bi}	mm	$\frac{D_{est} - D - 2h_t}{2}$
Diameter of Rotor	D_r	mm	$D - 2g$
Pole Pitch	τ_p	mm	$\frac{\pi D_r}{2p}$
Width of Polar Shoe	t_{ps}	mm	$\tau_p - t_{PM}$
Height of Polar Shoe	h_{ps}	mm	$h_p - t_{PM}$
Pole Angle	α_p	°	$\frac{360}{2p}$
Polar Shoe Electrical Angle	α_{ps}^e	°	$180\frac{t_{ps}}{\tau_p}$
Electrical frequency	f	Hz	$\frac{p \cdot n}{60}$
No of Slot per Pole and Phase	q		$\frac{Q}{2p \cdot m}$
No of Serial Conductor per Phase	N_s		$\frac{N_{turns} \cdot Q}{N_{pp} \cdot m \cdot N_{line}}$
No of Serial Conductor per Slot	n_{cs}		$\frac{N_{turns}}{N_{pp} \cdot N_{line}}$

the related angular shifting. The star of slot is represented in Fig. 2.3.

$$t = M.C.D.\{Q, p\} = M.C.D.\{96, 52\} = 4 \tag{2.1}$$

$$\frac{Q}{t} = 24 \tag{2.2}$$

$$\alpha_{stroke} = \frac{360}{24} = 15\,el.deg \tag{2.3}$$

The sum of the vector voltage for each coil is expressed by the pitch factor k_p, while the single layer connection employed leads the distribution factor k_d. The total winding factor k_w is then calculated and the electrical load $\hat{K}_s$ is defined considering the total current in slot $\hat{I}_{slot} = \sqrt{2}I_{line}n_{cs} = 9925A$ (with p_s and n_{cs} reported in Table 2.4).

$$k_p = \cos(\frac{\alpha_{stroke}}{2}) = 0.991 \tag{2.4}$$

$$k_d = \frac{\sqrt{2}}{2}\sqrt{1 + \cos(2\alpha_{stroke})} = 0.966 \tag{2.5}$$

$$k_w = k_p k_w = 0.991 * 0.966 = 0.958 \tag{2.6}$$

$$\hat{K}_s = k_w \frac{\hat{I}_{slot}}{p_s} = 106\frac{kA}{m} \tag{2.7}$$
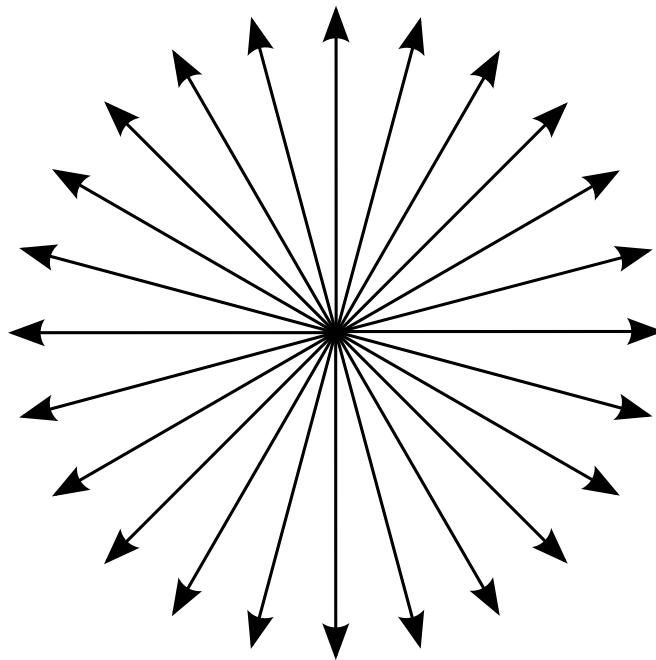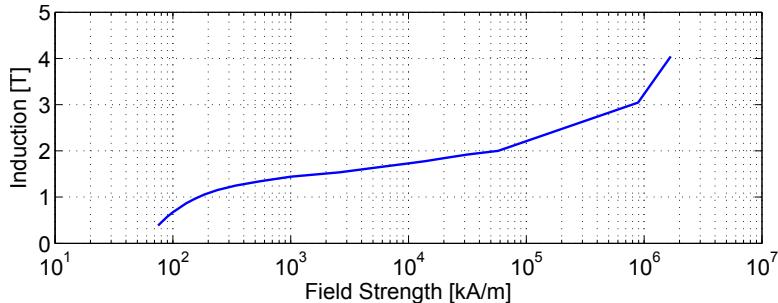
Figure 2.3: Star Of Slot for LW15 generator

No load magnetic circuit

To calculate the magneto motive force MMF in the magnetic circuit of the generator at no load condition the B(H) characteristic of Fig. 3.11 is considered. Four main parts are considered in the analysis: airgap, stator tooth, polar shoe and stator yoke.

Figure 2.4: $B(H)$ semilogarithmic characteristic of the laminated steel

Airgap According to Gauss and Ampére Laws the airgap induction is calculated. The second of the(2.8) is then considered together with the magnetic characteristics of the vacuum and magnets, i.e. $H_g = B_g/\mu_0$ and $H_{PM} = (B_{PM} - B_{rem})/(\mu_0\mu_{rec})$. It is possible to calculate B_g according to the parameters of Table 2.1. In order to calculate the airgap MMF $(NI)_g$ the Carter factor $K_c = 1.409$ is computed according to equation (2.11) and the airgap MMF $(NI)_g$ is obtained:

$$\begin{cases} B_{pm}h_{pm} = B_g \frac{\tau_p - t_{pm}}{2} \\ H_{pm}t_{pm} + 2H_g g = 0 \end{cases} \tag{2.8}$$

$$\begin{cases} B_{pm}h_{pm} = B_g \frac{\tau_p - t_{pm}}{2} \\ \frac{B_{pm} - B_{rem}}{\mu_{rec}} t_{pm} + 2B_g g = 0 \end{cases} \tag{2.9}$$

$$B_{g0} = \frac{B_{rem}}{\frac{\tau_p - t_{pm}}{2h_p m} + \frac{2g\mu_{rec}}{t_{pm}}} \tag{2.10}$$

$$Kc = \frac{1}{1 - \frac{w_s}{p_s} + [\frac{4}{\pi}\frac{g}{p_s}\ln((1 + \frac{pi}{4})\frac{w_s}{g})]} \tag{2.11}$$

$$(NI)_g = \frac{B_{g0}}{\mu_0} K_c g \tag{2.12}$$

Stator tooth according to the Gauss Law the flux density in the stator teeth $B_t w_{t,\frac{1}{3}}$ is calculated at one third of the tooth height to obtain the MMF $(NI)_t$:

$$B_t w_{t,\frac{1}{3}} L_{stk} = B_g t_{ps} L_{stk} \Rightarrow B_t = B_g \frac{t_{ps}}{w_{t,\frac{1}{3}}} \tag{2.13}$$

$$(NI)_t = H_t h_t \tag{2.14}$$

Polar Shoe the polar shoe B_{ps} is the laminated iron portion of the rotor, it is assumed that $B_{ps} = B_{g0}$. The polar shoe MMF $(NI)_{ps}$ is then calculated.

$$(NI)_{ps} = H_{ps} h_{pm} \tag{2.15}$$

Stator yoke The stator yoke is crossed by half the tooth flux. The stator yoke MMF $(NI)_{bi}$ is calculated according to the length of the iron path in yoke $l_{abi} = \frac{1}{2}\frac{\pi(D_{est} - h_{bi})}{2p}$.

$$B_{bi}h_{bi}L_{stk} = \frac{1}{2}\phi = \frac{1}{2}B_{g0}t_{ps}L_s tk \Rightarrow B_{bi} = \frac{1}{2}B_g 0\frac{t_{ps}}{h_{bi}} \tag{2.16}$$

$$(NI)_{bi} = H_{bi} l_{abi} \tag{2.17}$$

The results of the computation of the magnetic circuit of the machine are listed in Table 2.5. It is now possible to calculate the saturation factor $k_{sat} = 1.17$ and the equivalent airgap $g'' = 4.9mm$ to be considered if the permeability of iron were infinite.

The computation of the magnetic circuit is completed after an iterative process where k_{sat} is calculated at each step.

$$k_{sat} = \frac{(NI)_g + (NI)_t + (NI)_{ps} + (NI)_{bi}}{(NI)_g} \tag{2.18}$$

$$g'' = K_c k_{sat,1} g \tag{2.19}$$

Table 2.5: Flux density and MMF, no load, first iteration

Portion	B [T]	NI [A]
Airgap	1.79	6018
Stator Tooth	1.82	1682
Polar Shoe	1.79	1012
Stator yoke	1.49	76

No load voltage

The value of the fundamental $B_{g0,1}$ of no load flux density in airgap is computed starting from equation 2.10. The magnetic flux in the airgap of the generator ϕ_m is used to compute the flux linkage Λ. The no load rms phase voltage is finally obtained $E_0 = 344V$, considering the rated electrical angular speed $\omega = 2\pi f = 99s^{-1}$

$$B_{g0,1} = \frac{2}{\pi} B_{g0} \sin(\alpha^e_{ps}/2) \tag{2.20}$$

$$\phi_m = B_{g0,1} \frac{D L_{stk}}{p} \tag{2.21}$$

$$\Lambda = \frac{k_w N_s}{2} \phi \tag{2.22}$$

$$E_0 = \sqrt{2}\omega\Lambda \tag{2.23}$$

No load losses in stator iron

The no load iron losses with are calculated through classical Steinmetz equation: the flux density has been obtained with equation (2.13) and (2.16). The specific loss c_p is given in Table 2.3. The masses of laminated iron in stator $G_{t,tot}$ and G_{bi} are computed with the specific iron mass $\gamma_{Fe} = 7800 \ kg/m^3$ and geometrical parameters in Table 2.2 and 2.3.

Total losses in the laminated iron of the stator are $P_{Fe,s,0} \sim 10$ kW: a factor 1.5 to estimate the effect of cutting the iron steel is considered.

$$p_{sp,t} = c_p \left[0.7 \left(\frac{f}{50} \right) \left(\frac{B_t}{1.5} \right)^2 + 0.3 \left(\frac{f}{50} \right)^2 \left(\frac{B_t}{1.5} \right)^2 \right] \tag{2.24}$$

$$p_{sp,bi} = c_p \left[0.7 \left(\frac{f}{50} \right) \left(\frac{B_{bi}}{1.5} \right)^2 + 0.3 \left(\frac{f}{50} \right)^2 \left(\frac{B_{bi}}{1.5} \right)^2 \right] \tag{2.25}$$

$$G_{t,tot} = \gamma_{Fe} Q \frac{w_t + w'_t}{2} h_t L_{stk} \tag{2.26}$$

$$G_{bi} = \gamma_{Fe} \pi D_{abi} h_{bi} L_{stk} \tag{2.27}$$

$$P_{Fe,s,0} = 1.5(p_{sp,t} G_{t,tot} + p_{sp,bi} G_{bi}) \tag{2.28}$$

Magnetic circuit at load

In this section the magnetic circuit is calculated at load condition. The electrical load of the machine, while the rated current is flowing into the slot is $K_s(\theta_s) = -\hat{K}_s \sin(p\theta_s)$, where θ_s is the mechanical angle between stator and d axis. The magnetic potential due to the stator current is computed in equation (2.29) and the reaction due to stator current is shown in equation (2.31), considering the way go and the way back of the flux path trough the equivalent airgap calculated in equation (2.30):

$$U_s = \int_0^{\frac{\pi}{p}} -\hat{K}_s \sin(p\theta_s)\frac{D}{2}d\theta_s = \frac{\hat{K}_s D}{p} \tag{2.29}$$

$$\phi = \frac{U_s}{2\mathcal{R}_g} \Rightarrow B_{curr}S_g = U_s \frac{\mu_0 S_g}{2g''} \text{ con } S_g = \frac{\pi D L_{stk}}{2p} \tag{2.30}$$

$$B_{curr} = U_s \frac{\mu_0}{2g''} \tag{2.31}$$

Like in the no load case,the magnetic circuit of the machine is divided into four sections to be analyzed:

Airgap The value of the flux density in airgap at load is expressed as per equation (2.32), then the same procedure of the no load case is followed.

$$B_{g,load} = B_{g0} + B_{curr} \tag{2.32}$$

Stator tooth the component of the flux density due to current is considered. B_{gap} is computed according to Gauss Law then. The magnetic voltage drop is obtained using the magnetic curve of the material.

$$\begin{aligned} B_{gap} &= B_{g0} + \frac{1}{p\alpha_s} \int_0^{p\alpha_s} B_{curr} \cos\theta d\theta \tag{2.33} \\ &= B_{curr}\frac{\sin p\alpha_s}{p\alpha_s} \end{aligned}$$

$$B_{t,load} = B_{gap}\frac{p_s}{w_{t,\frac{1}{3}}} \tag{2.34}$$

Polar Shoe the component of the flux density due to current is considered in the polar shoe also:

$$B_{ps,load} = B_{g0} + \frac{2}{\pi}B_{curr} \tag{2.35}$$

Stator yoke it is assumed that:

$$B_{bi,load} = B_{bi} \tag{2.36}$$

With the same iterative process used in the no load case the magnetic circuit at load is then computed.

Load EMF

It is pointed out that the back EMF at load condition $E_{0,load}$ is lower than at no load condition E_0. The value of the ratio $k = \frac{E_{0,load}}{E0}$ is ~ 0.9.

Load losses in stator iron

The stator iron losses in lamination are recalculated at load condition $P_{Fe,load} \sim 14kW$. They increase in respect to the no load values; this is due to the saturation in the magnetic circuit of the machine.

Inductances calculation

The following equations are employed to calculate the synchronous inductances of the generator.

Magnetization inductance The magnetization inductance is the inductance of the three phase system of the generator supposing that the rotor is isotropic:

$$L_m = \frac{3}{\pi}\mu_0 \left(\frac{k_w N_s}{2p}\right)^2 \frac{DL}{g''} \qquad (2.37)$$

Leakage inductances The leakage inductance is due to three main causes:
slot leakage inductance

$$L_{\sigma,slot} = \mu_0 n_{cs}^2 q 2p L_{stk} k_{slot} \qquad (2.38)$$

where k_{slot} depends on slot shape:

$$k_{slot} = \frac{h_s}{3w_s} + \frac{h0}{w_s} \qquad (2.39)$$

airgap leakage inductance

$$L_{\sigma,gap} = \mu_0 n_{cs}^2 q^2 2p L_{stk} 0.88 \qquad (2.40)$$

end winding leakage inductance

$$L_{\sigma,ew} = \mu_0 n_{cs}^2 q^2 2p L_{ew} 0.44 \qquad (2.41)$$

The machine considered to be isotropic, it is then possible to calculate the q-axis and d-axis inductances:

$$L_d = L_q = L_s = 1.35mH \qquad (2.42)$$

The total reactance is obtained by the sum of the inductances times the rated electrical pulsation:

$$X_s = \omega L = 2 \cdot \pi \cdot f \cdot L_s = \Omega \cdot L_s \sim 0.1\Omega \qquad (2.43)$$

Analytical results are listed in Table 2.6.

Table 2.6: Analytical calculation of inductances

Part	Value [mH]
$L_{\sigma,slot}$	0.50
$L_{\sigma,gap}$	0.16
$L_{\sigma,ew}$	0.02
L_m	0.67
L_s	1.35

Copper losses and phase resistance

The formula in equation (2.44) is employed to calculate copper losses. $\gamma_{Cu} = 8900 Kg/m^3$ is the specific weight of the copper and the resistivity is $\rho_{Cu(140C)} = \rho_{Cu(20C)}(1+\alpha T) = 0.018(1+4{\cdot}10^{-3}) = 0.027 \mu\Omega m$. The mass of copper and the current density are calculated in equation (2.46) and (2.47).

$$P_{Cu} = \rho_{Cu@140C} J^2 Volume = \frac{\rho_{Cu@140C}}{\gamma_{Cu}} Peso_{Cu} J^2 \tag{2.44}$$

$$\rho_{Cu@140C} = \rho_{Cu@20C}(1 + \alpha T) = 0.018(1 + 4{\cdot}10^{-3}) = 0.027 \mu\Omega m \tag{2.45}$$

$$Peso_{Cu} = \gamma_{Cu} S_{cond,cava}(L_{stk} + L_{ew}) \tag{2.46}$$

$$J = \frac{I_{linea}}{\underbrace{w_c h_c N_{spire} n_{c,turn}}_{S_{cond,cava}}} \tag{2.47}$$

The current in copper slot is not uniformly distributed at load condition, so a factor to increase copper losses is calculated k^* :

- Calculation of the coefficient $\xi = \alpha h_c = 2\pi\sqrt{\frac{w_c f}{w_s 1{\cdot}10^5 \rho_{Cu@140C}}}$

- Reading from table 2.7 of coefficients y e z

- listing the conductors as $c_n = \{1, \ldots, N_{spire}\}$ coefficients are obtained $K(c_n) = y + (c_n^2 - c_n)z$ and their average value K'

- The coefficient to increase losses is K^* according to the formula $K^* = \frac{K' L_{stk} + L_{ew}}{L_{stk} + Lew}$

The final value is $K^* = 1.078$ and so the final value for Cu losses is $P_{Cu} \sim 55kW$. The equivalent resistance is then:

$$R_s = \frac{55{\cdot}10^3}{3{\cdot}I_{line}^2 * N_{line}} = 10m\Omega \tag{2.48}$$

Table 2.7: Correction coefficients y e z

ξ	0	0.2	0.3	0.4	0.5	0.6
y	1	1	1	1	1	1.01
z	0	0.00053	0.0027	0.0085	0.021	0.043

ξ	0.7	0.8	1.0	1.2	1.5	2.0	3.0
y	1.02	1.035	1.086	1.18	1.38	1.89	3
z	0.079	0.134	0.32	0.64	1.41	3.25	6.25

Generator Equivalent Circuit and Voltage at load

The equivalent single phase circuit of the generator is represented in Fig. 2.1.1. The equivalent synchronous impedance is calculated as $\dot{Z}_s = R_s + jX_s$. The phasor diagram of the generator is in Fig. 2.1.1, where V is obtained starting from X_s according to equation (2.43) and $E_{0,load}$ according to equation (2.49) and the line current I_{line}. The power factor $\cos\phi$ is also computed.

$$E_{0,load} = \sqrt{E_{load}^2 - (X_s I_{line})^2} = 300\text{V} \tag{2.49}$$

$$\cos\phi = \frac{E_{0_{load}}}{E_{load}} = 0.77 \tag{2.50}$$
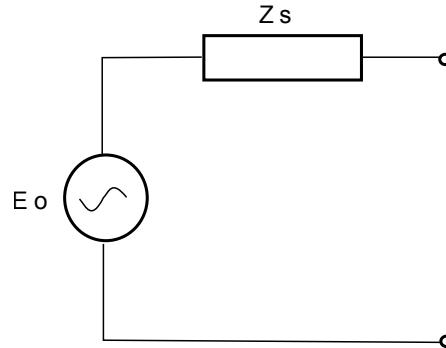
Figure 2.5: Generator Equivalent circuit
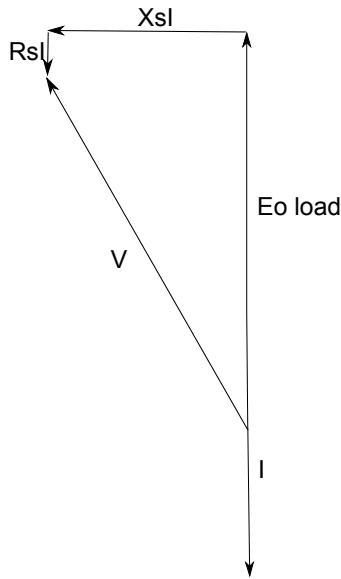
Figure 2.6: Generator Phasor Diagram

Electromagnetic Torque and Power

The electromagnetic power can be calculated as per equation (5.6), in order to obtain the electromagnetic torque T_{el}. The output power P_{out} is finally computed. Result for torque is then $T_{el} \simeq 0.96$MNm.

$$P_{el} = 3E_{0,load}I_{line}N_{line} \sim 1.78MW \qquad (2.51)$$

$$T_{el}\frac{2\pi}{60}n = 3E_{0,load}I_{line}N_{line} = P_{el} \qquad (2.52)$$

$$T_{el} = \frac{P_e l}{\frac{2\pi}{60}n} \qquad (2.53)$$

$$P_{out} = 3VI_{line}cos\phi \sim 1.72MW \qquad (2.54)$$

Rotor losses calculation

There are four kinds of rotor materials in the rotor of LW15C generator:

- permanent magnets
- laminations
- aluminium profile
- the rotor yoke

Each of them produces losses due to:

- slot opening of the stator, which gives losses not related to the current in slots

- load reaction of the machine due to the fractional slot winding. This reaction consist in subharmonics and harmonics of the airgap MMF which enter the massive materials in rotor.

The rotor losses in the laminated steel can be calculated with analytical approach, with Steinmetz relations, in the same way used for stator lamination in equation (2.24) and equation (2.25). This represents an over–estimation.

Considering a polar shoe induction of 1.9 T the results is $P_{Fe,r,load} = 6kW$ they are calculated at load.

It is possible to deeply analyze the topic of the rotor losses thanks to finite element simulations: Chapter 3 is specifically dedicated to this issue.

Analytical Results Summary

According to Table 2.8 main results presented in this section are listed. They are the updated results for the analytic model of LW15 C generator at 18.2 r/min speed and 2x968 A current. The parameters for single phase equivalent circuit are given.

Table 2.8: Analytical Results Summary

Description	Symbol	Result
Total winding factor	k_w	0.958
No Load BEMF	E_0	343 V
Load BEMF	$E_0 load$	307 V
Load Voltage	V	400 V
Power factor	$\cos\phi$	0.77
Electromagnetic torque	T	937 kNm
Electromagnetic power	P_{el}	1780 kW
Losses in stator iron load	$P_{Fe,s,load}$	11 kW
Copper losses 140 °C	P_{Cu}	55 kW
Losses in rotor iron load	$P_{Fe,r,load}$	6 kW
Synchronous inductance	L_s	1.35 mH
Phase resistance 140 °C	R_s	10 $m\Omega$

2.1.2. Finite Element Model of the Generator

The finite element (FEM) model of the generator has been built in order to deep analyze the behavior of the generator under study. The computation of the electromagnetic outputs for LW15 C LTW generator has been performed by modeling one eight of the machine, with 13 magnetic poles and 12 slots. The software employed is FEMM [12]. Fig. 2.1.2 represents the model with field lines at no load.
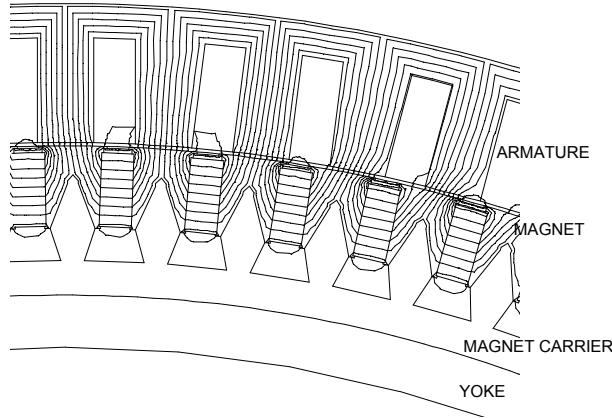
Figure 2.7: FE model used for the calculation of generator electromagnetic outputs

Assumptions of the model

The FEM study of the LW15 C generator has been done both at load and no load. When the load analysis is done the FEM model is fed with the three phase system of currents in equation (2.55), where $I_{line}N_{line}$ represents the total rms current as in 2.1.1, α_{ie} is the angle of the current in respect to the d-axis of the rotor frame reference and θ is the position of the rotor.

$$
\begin{aligned}
i_a &= \sqrt{2}I_{line}N_{line}\cos(\theta - \alpha_{ie}) \\
i_b &= \sqrt{2}I_{line}N_{line}\cos(\theta - 120 - \alpha_{ie}) \\
i_c &= \sqrt{2}I_{line}N_{line}\cos(\theta - 240 - \alpha_{ie})
\end{aligned}
\tag{2.55}
$$

The following aspects must be considered:

- For geometry and material characteristic refer to section 2.1.1;

- Rated armature current is 1936 A (q-axis current, i.e. $\alpha_{ie} = 90$ *el.deg.*);

- Generator speed is 18.2 *r/min*;

- Magnets remanence is 1.09 T;

- Copper temperature is 140 °C;

- The magnet pole carrier is not magnetic;

- The iron yoke is magnetic.

Basic No Load Computation

The no load simulation has been performed. The results the basic computations of flux linkage, phase voltages and cogging torque are given in Fig. 2.8, Fig. 2.9 and Fig. 2.10.
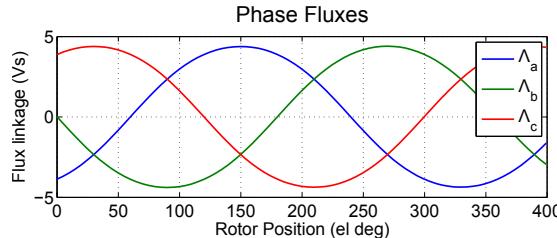
Figure 2.8: Flux linkage at no load
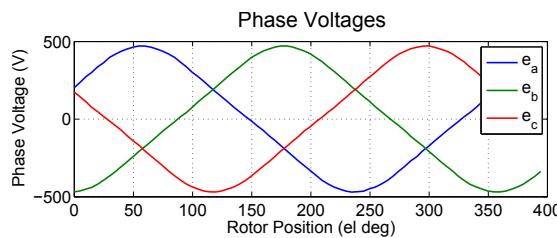
Figure 2.9: Phase voltage at no load
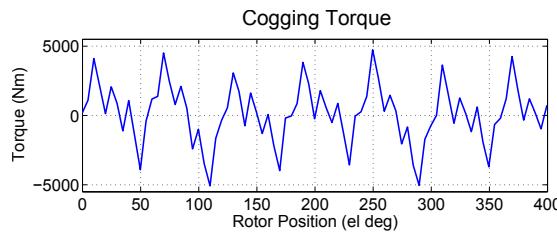
Figure 2.10: Cogging torque

Basic Load Computation

The results the basic computations of load simulation are now presented. The flux linkage, phase voltages and cogging torque are given in Fig. 2.11, Fig. 2.12 and Fig. 2.13.

The machine is fed with q-axis current only: it is then possible to threat it as an isotropic rotor machine. The synchronous inductance is consider to be equal to the q-axis inductance. It is calculated in equation (2.56).

The power factor is calculated according to in equation (2.57), where $arctan\frac{I_q}{I_d} = \frac{\pi}{2}$.

$$L_s = L_q = \frac{\Lambda_q}{I_q} \tag{2.56}$$
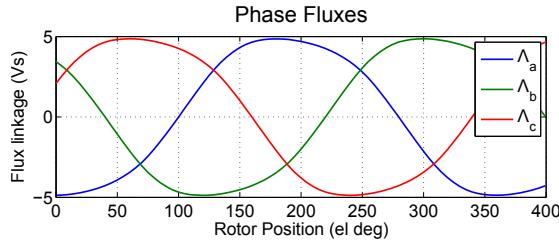
Figure 2.11: Flux linkage at load
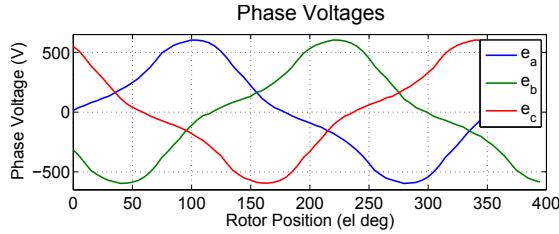
Figure 2.12: Phase voltage at load
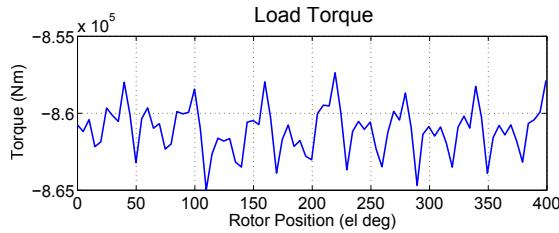
Figure 2.13: Load torque

$$\cos \phi = \cos \left(\frac{\pi}{2} + \arctan \frac{\Lambda_q}{\Lambda_d} - \arctan \frac{I_q}{I_d} \right) \tag{2.57}$$

Basic FEM Results Table

According to Table 2.9 main results presented in this section are listed: they are the updated results for the FEM model of LW15 C generator. It is worth noticing that the rotor of the machine has been considered to be isotropic. The values marked with " $*$ " are analytically calculated in section 2.1.1, but the values of the remanence in tooth B_t and stator back iron B_{bi} have been computed with FEM both at load and no load.

Table 2.9: Updated Results FEM Simulation

Description	Symbol	Result
No Load phase BEMF rms	E_0	317 V
No Load Flux linkaged rms	Φ_{nl}	3.18 Wb
Load Flux linkaged rms	Φ_l	3.68 Wb
Load phase Voltage rms	V	370 V
Power factor	$\cos\phi$	
Cogging torque peak	T_cog	4 kNm
Electromagnetic torque	T	861 kNm
Electromagnetic torque ripple	dT/T	1%
Electromagnetic power	P_{out}	1640 kW
Synchronous inductance	L_s	1.2 mH
Power factor	$\cos\phi$	0.78
Total losses at load*	$P_{tot,s,load}$	71 kW
Phase resistance* 140 °C	R_s	10 $m\Omega$

A structural aspect: forces on magnetic poles

The forces acting on magnetic poles has been computed in this FEM analysis. Fig. 2.14 shows the paths used to calculate forces in the middle of the airgap of the generator: one path is on the right side of the pole, while the other one is on the left side. These paths are lines in a 2–D domain, but they represents surfaces in a real 3–D space. The equations of Maxwell Stress Tensor (2.58) are applied by the FEM code on such lines in order to compute both the tangential dF_t and the normal component dF_n to the line (2.59).

The frequency of the forces under study is $29.12 Hz$ (equal to the number of slots, 96, multiplied by the rotation speed, 18.2 r/min and divided by 60 s): it is called 'slotting frequency' and it corresponds to the frequency seen by a rotor element due to the alternation between teeth and slots.

$$d\mathbf{F} = -\frac{\mu_0}{2} H^2 \mathbf{n} dS + \mu_0 \left(\mathbf{H} \cdot \mathbf{n} dS\right) \mathbf{H} \tag{2.58}$$

$$dF_t = \left(\mu_0 H_t H_n\right) dS$$
$$dF_n = \frac{\mu_0}{2} \left(H_n^2 - H_t^2\right) dS \tag{2.59}$$

The calculation has been done in three load cases, some remarks must be considered:

- The first simulation is at no load;

- The second simulation is at load with 9925 A peak in slot (Load1);

- The third simulation is at load with 10860 A peak in slot (Load2);
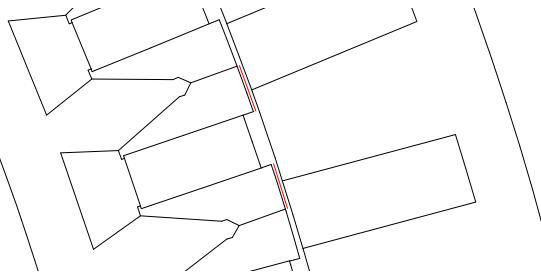
Figure 2.14: Paths used to calculate radial forces

- The integration lines chosen for Maxwell stress tensor in Fig. 2.14 extend above the iron part of the magnet pole element;

- Such integration lines move together with the rotor;

- The computed force are given per length.

The no load simulation has been performed. Fig. 2.15 shows the behavior of the radial force calculated both on the right integration path and on the left integration path. Fig. 2.16 shows the behavior of the tangential force calculated both on the right integration path and on the left integration path . To complete the monitoring of the field on those paths, the absolute value of the flux density is shown in Fig. 2.17.

The total radial and tangential forces calculated on the magnet pole is obtained in
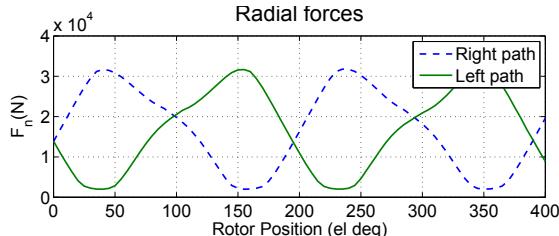
Figure 2.15: behavior of the radial force at no load
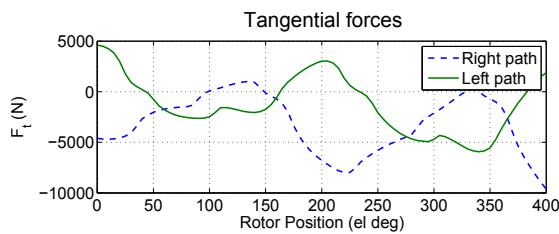
Figure 2.16: behavior of the tangential force at no load

Fig. 2.18: this is the sum of the forces calculated on the right and left paths.

The load simulation is then studied. Fig. 2.19 shows the behavior of the radial force calculated both on the right integration path and on the left integration path. The total current in slot is 9925 A peak (Load1). Fig. 2.20 shows the behavior of the tangential force calculated both on the right integration path and on the left integration
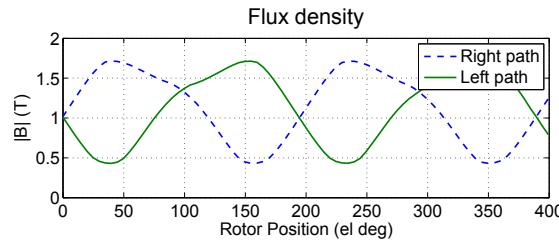
Figure 2.17: Flux density in the airgap at no load
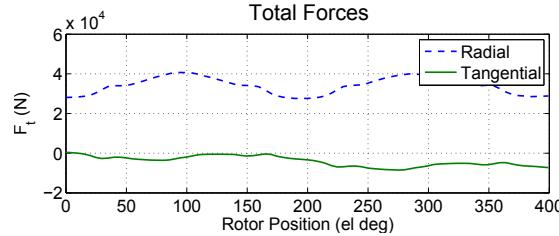
Figure 2.18: behavior of forces on a single magnet pole at no load

path . It is worth noticing that the absolute value of the flux density (Fig. 2.21) is very unbalanced in respect to no load case. This is due to the fact that half pole partially demagnetized while half pole is magnetized if the machine is fed with q-axis current. This behavior is then presented in the force waveform also of Fig. 2.19 and Fig. 2.20 and it is more evident in the radial force, which depends on the square of the flux density in the airgap.

Fig. 2.22 shows the behavior of the radial force with 9925 A peak in slot (Load A).
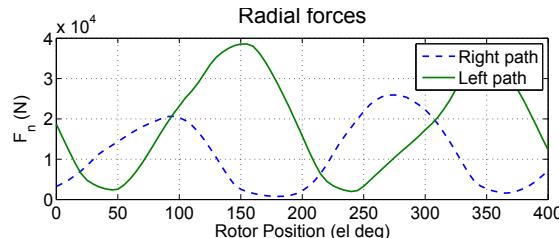
Figure 2.19: behavior of the radial force with 9925 A in slot
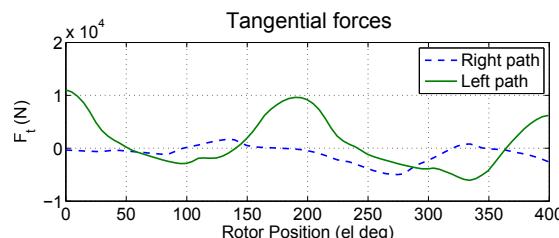
Figure 2.20: behavior of the tangential force with 9925 A in slot

A clear difference in respect to the no load case is the force ripple: it is higher at load than at no load, and it increases with the total current in slot. The peak value of the
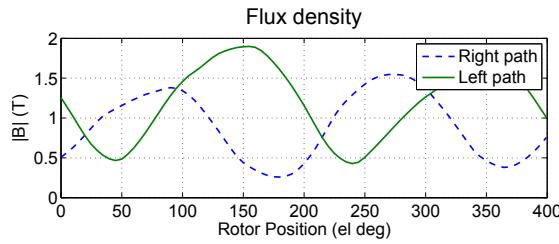
Figure 2.21: Flux density in the airgap with 9925 A in slot
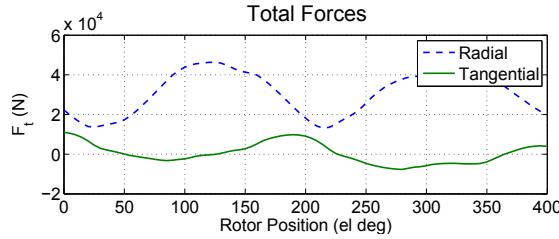
Figure 2.22: behavior of the radial force with 9925 At peak in slot

force increases at load, while the minimum value is lower at load than at no load.

The average, the maximum and minimum values of the radial forces calculated on a single magnetic rotor element are now collected. Table 2.10 shows that the average force on rotor poles is higher at no load than at load. This is caused by the reaction of the stator field of the machine, due to the q-axis current feeding.

Table 2.10: Radial Forces Calculation

Load case	Average Force (kN/m)	Maximum Force (kN/m)	Minimum Force (kN/m)
No Load	35.0	44.0	28.2
Load1	31.8	47.3	15.2
Load2	32.3	50.9	12.8

A control aspect: anisotropy of the rotor

Fig. 2.23 represents the model with field lines at load. It results to be $L_d \neq L_q$ if $\alpha_{ie} \neq 90$ *el.deg.*: a slight anisotropy between the direct axis a the quadrature axis is present. A little reluctance torque component appears on the MTPA (maximum torque per ampere) trajectory.

To compute the inductances in this load situation equations (2.60) are used. Results of the simulation are presented in Table 2.11.

$$L_d = \frac{\Lambda_{d,0} - \Lambda_d}{I_d}$$
$$L_q = \frac{\Lambda_q}{I_q}$$

(2.60)
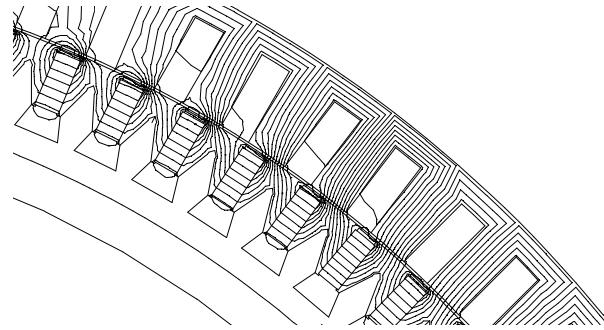
Figure 2.23: FE model of the generator at load

The power factor is then computed again according to in equation (2.57). The new

Table 2.11: Value of inductances with MTPA feeding

Direct-axis L_d	1.09	mH
Quadrature-axis L_q	1.17	mH

value $\cos\phi$=0.79 is more than 1% higher than the previous one (0.78): the same improvement results in torque as well.

Detailed Computation of Rotor Losses

The detailed computation of the Rotor Losses is possible by mean of Finite Element. The stator of the machine is replaced by a current sheet. A series of time-harmonic simulations have been performed in order to evaluate the impact of each harmonic of the MMF due to the armature reaction of the machine on each part of the structure of the rotor.

The so called Current Sheet Method is described and validated on Large Direct Drive machines in Chapter 3.

2.1.3. Comparison Between Analytical and FEM

The main analytical and FEM results of Table 2.9 and Table 2.8 are collected in Table 2.12 which provides an overview of the two computations.

The analytical values are generally bigger than the FEM ones. This is mainly due to the presence of holes in the real magnetic structure of the machine, which are modeled with FEM only. The analytical model gives a greater value for the synchronous inductance L_s in respect to the FEM model. This is due to the fact that the FEM model does not take the end winding 3–D effect into account.

Table 2.12: Comparison between main analytical and FEM results

Description	Symbol	Analytical	FEM
No Load BEMF	E_0	344 V	317 V
Load Voltage	V	400 V	370 V
Power factor	$\cos\phi$	0.77	0.78
Electromagnetic torque	T	937 kNm	861 kNm
Electromagnetic power	P_{el}	1780 kW	1640 kW
Total losses at load	$P_{tot,s,load}$	72 kW	71 kW
Synchronous inductance	L_s	1.35 mH	1.2 mH

2.2. Back to Back Test Bench in Telfs

Fig. 2.24 shows the Back to back (B2B) test bench built in Telfs, in Fig. 2.25 a detail of the shaft which connects the two machines is presented. Telfs is in North–Tirol, Austria, where the Leitner Technologies Group has recently developed a new factory for wind mills production. One machine runs as a generator, while the other one runs as a motor. Images are courtesy of Leitwind A.G.

Figure 2.24: B2B test bench in Telfs
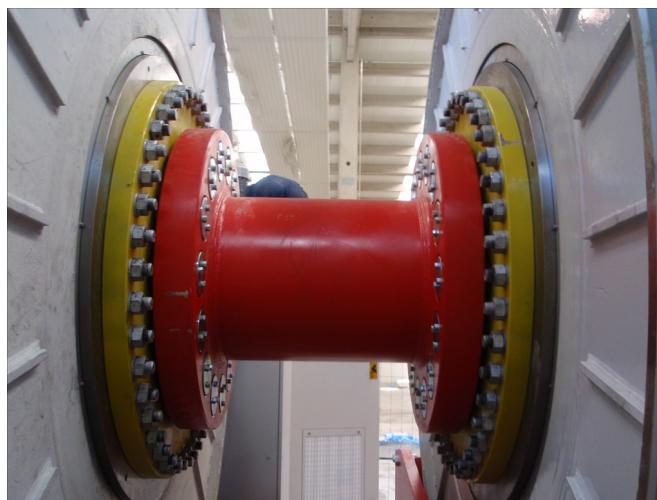
Figure 2.25: Detail of the B2B test bench in Telfs

2.2.1. Testing activity on LW15C

The testing activity done by Leitwind on the B2B test bench has covered a large period and it is still on going in Telfs. The different generator models, each of them design for a specific wind turbine are tested at the bench.

The LW15 C generator represents the basis of the majority of LTW generators types and it is more tested Leitwind machine. References for the method used are given by the standards in [13–15].

In this section an overview of the testing activity is given considering the following tests:

- the machine runs at no load;

- the machine runs at load;

- the machine is characterized at different rotor speed at no load;

- the machine is characterized at full load according to Leitwind LTW77 power curve [4];

- the synchronous inductance of the machine is measured;

- the thermal rise run of the machine is performed in order to measure losses in the rotor.

Electrical Layout of the test bench

The test bench consists in two twins LW15 C generators. They are fed by power converters (two for each machine): measure boxes are placed at the converter terminals in order to measure the power developed by the electrical machines, one working as a motor, the other one working as a generator, and the power on the grid side.

The grid must provide the losses of the whole system. A sketch of the electrical layout is presented in Fig. 2.26.
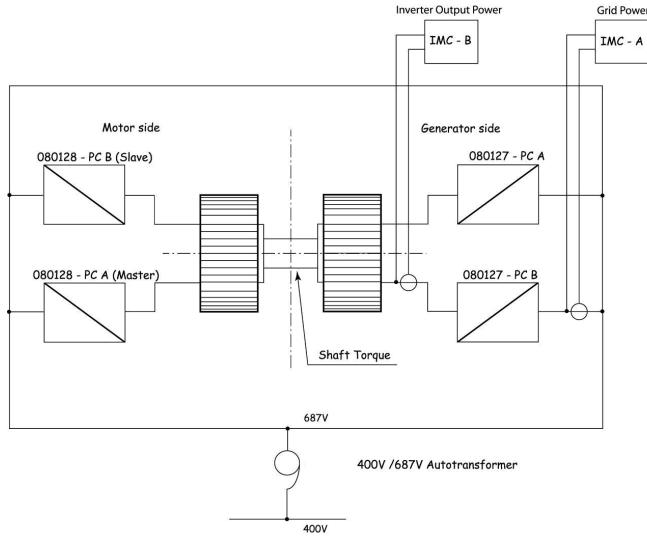
Figure 2.26: Sketch of the electrical layout of the B2B test bench

No load characteristic of the generator

The no load characteristic of the generator is shown in Fig. 2.27. The value of the phase voltage at 18.2 min^{-1} is E_0=311 V and it is comparable with the value (317 V). obtained with finite element in Table 2.9.
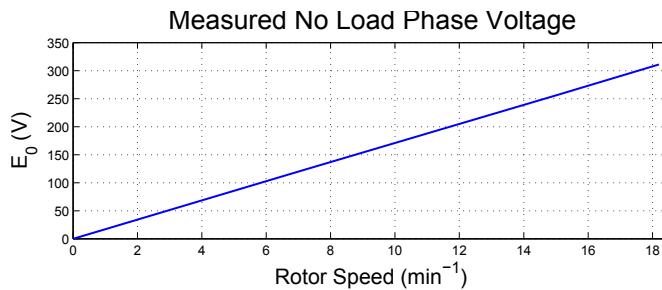
Figure 2.27: Measure no load characteristic of the generator

Load characteristic of the generator along LTW77 power curve

The power curve of the LTW77 wind turbine can be found in [4]: it is the reference for the building of the load characteristic of the generator at the B2B. The obtained load characteristic is presented in Fig. 2.28. It is worth noticing that the output power P_{turb} given in the power curve refers to the whole turbine. The electrical power of the generator is given by equation (2.61), where P_{out} is the electrical power at the terminals of the generator, P_{conv} represents the losses of the power electronics modules and P_{cab} is due to the cables in the tower of the wind turbine.

$$P_{out} = P_{turb} + P_{conv} + P_{cab} \tag{2.61}$$

The value of the output power at 18.2 min^{-1} rotor speed is 1556 kW with a copper temperature around 120/°C. That means that the copper losses are almost P_{Cu}=50 kW. The iron losses at load obtained with finite element in Table 2.9 are P_{iron}=17 kW. The generator output power predicted with FEM analysis is then $P_{out} \approx P_{el} - P_{cu} - P_{iron}$=1640-67=1573 kW.
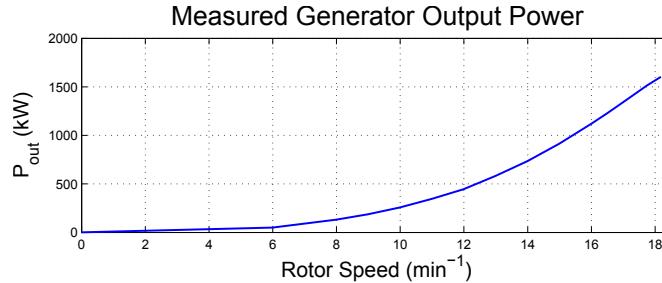
Figure 2.28: Measure output power of the generator

Measure of the synchronous inductance

It is possible to perform the measure of the synchronous inductance of the machine starting from the hypothesis of isotropic rotor machine, because it has been verified that $L_s = L_d \approx L_q$ via previous FEM analysis.

The machine is fed according to equation (2.62), the quadrature–axis current is negligible, because the no-load losses only must be provided.

$$\begin{aligned} I_d \neq 0 \\ I_q \approx 0 \end{aligned} \tag{2.62}$$

In this situation the inductance of the machine is well–approximated the equation (2.63), where symbols are the same employed in section 2.1.2.

$$L_s \approx L_{meas} = \frac{E_0 - \sqrt{V^2 - R_s^2 I_d^2}}{\omega I_d} = 1.28\text{mH} \tag{2.63}$$

Comparison between FEM model and B2B test at rated speed

A summary of the prediction of the FEM model against the results of the measures at B2B test bench is given in Table 2.13. It is worth noticing that the generator output power calculated with FEM does not take the rotor losses in massive materials into account yet: the method to compute them will be explained and applied in Chapter 3, losses in iron only are considered.

Table 2.13: Comparison between main B2B and FEM results

Description	Symbol	FEM	B2B
No Load BEMF	E_0	317 V	311 V
Load Voltage	V	370 V	367 V
Power factor	$\cos \phi$	0.78	0.75
Output power	P_{out}	1573 kW	1556 kW
Synchronous inductance	L_s	1.2 mH	1.28 mH

Measure of Rotor Losses

A large part of B2B testing activity has been dedicated to the measure of the losses in the rotor of the machine. The calorimetric method has been employed according to the standards in [13–15]. This activity is described in in Chapter 3 and compared with the so called Current Sheet Method.

2.3. A Direct Drive Motor for Ropeways Traction

The Company Leitner AG has developed the first Drive Drive motor for ropeways traction, the concept is presented in [16] The so called SFA direct drive motors is presented in Fig. 2.29. Fig. 2.30 shows a detail of the inner structure. The general characteristics of the machine are listed in Table 2.14. The analytical and FEM study of a prototype SFA motor is now briefly described. Test bench activity on B2B test bench in Telfs is then considered.

Table 2.14: General Characteristics of the SFA direct drive

Ropeways Motor	Symbol	Value	Unit
Number of Slots	Q	96	
Number of Poles	$2p$	80	
Number of Phases	m	3	
Stator Outer Diameter	D_{est}	2160	mm
Rated Power	P_{gen}	550	kW

Figure 2.29: SFA direct drive motor of Leitner Ropeways
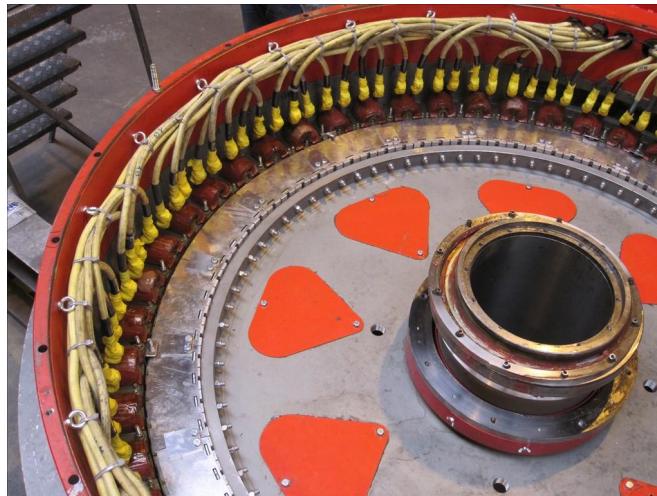
Figure 2.30: Detail of the inner structure of the SFA direct drive motor

2.3.1. Analytical and FEM Model of the Motor

The analytical study of the motor is done following the same guidelines and models used for LW15 C generator. To predict the performance of the SFA motor, the same simplified structure of Fig. 2.2 is used. The parameters employed and their values are presented in Table 2.15. Some numerical values are not given due to confidentiality. The winding is a single–layer one. Table 2.16 collects the symbols used for the geometrical characteristics of the motor,some values are given. The relations presented in Table 2.4 are then used again.

The FEM study of the SFA motor has been done both at load and no load. Once again the load analysis is done by feeding the FEM model with the three phase system of currents in equation (2.55), where $I_{line}N_{line}$ represents the total rms current as in 2.1.1, α_{ie} is the angle of the current in respect to the d-axis of the rotor frame reference

Table 2.15: General Parameters to Analytical Calculation of Motor

Generator Parameters	Symbol	Value	Unit
Number of Turns per Phase	N_{turns}	18	
Number of Parallels Paths	N_{pp}	4	
Number of Three Phase Systems	N_{line}	4	
Slot Filling Factor	K_{fill}	0.75	
Line Current	I_{line}	274	A
Total Current	$N_{line}I_{line}$	1095	A
Speed	n	19.5	r/min

Table 2.16: General Data to Analytical Calculation of Motor

Geometrical Data	Symbol	Value	Unit
Stator Inner Diameter	D		
Airgap	g		
Width of Slot	w_s		
Height of Slot	h_s		
End Slot Thickness	h_0	5.6	mm
Insulation Thickness	t_{ins}		
Length of Machine	L_{stk}	~ 750	mm
Inner Diameter of Rotor	D_{ir}		
Outer Diameter of Rotor	D_{gr}		
Length of PM	t_{pm}		
Height of PM	h_{pm}		
Remanence induction	B_{res}	1.09	T
Permeability	μ_{rec}	1.07	
Per Weight Losses (@ 1.5 T 50 Hz)	c_p	5.3	W/kg

and θ is the position of the rotor. Fig. 2.31 represents the map of induction of the model with field lines at load on a stator tooth. It results to be $L_d \neq L_q$ if $\alpha_{ie} \neq 90 \ el.deg.$: an anisotropy between the direct axis and the quadrature axis is present, together with a reluctance torque component on the MTPA trajectory.

To compute the inductances in this load situation equations (2.60) are used again. The phase voltages at load are shown in Fig. 2.32.
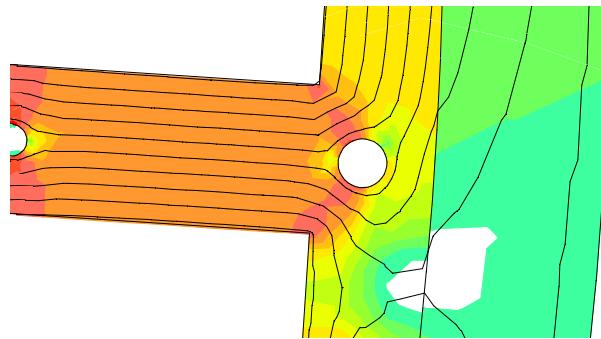
Figure 2.31: Stator tooth at load: field map
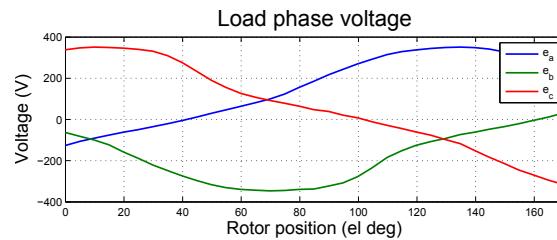
Figure 2.32: Phase Voltages at load

Effect of the holes on the magnetic circuit

The necessity to assemble the active of the machine leads to the presence of stator holes in the magnetic circuit. They causes lack of flux linkage and so of torque: this is due to extra–saturation, as can be noticed in Fig. 2.31. The voltage of one stator coil at no-load is shown in Fig. 2.33.

The machine is then simulated again at no load after erasing all the holes. The effect of the holes of the machine on flux linkage is presented in Fig. 2.34: the peak value is more than 5% lower.
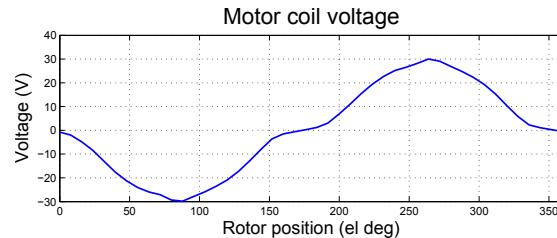
Figure 2.33: Voltage at no load of one coil
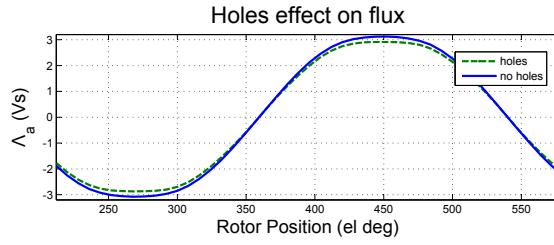
Figure 2.34: Effect of the holes at no load on flux linkage

Two different connections of the stator coils

The SFA motor has been calculated with two different connection of the stator coils, called 'Connection A' and 'Connection B'. Considering the three phase system A-B-C, the winding scheme of each connection for six stator coils is:

- 'Connection A' according to the sequence +A +C +B -A -C -B;

- 'Connection B' according to the sequence +A +A -B -B +C +C;

'Connection B' has been computed via finite elements only, while 'Connection A' is the correct one for this machine and it is considered both in FEM and in analytical model also. Computations of torque for 'Connection B' can be found in Chapter 5.
The back electro motive force (BEMF) which correspond to each connection at load is presented in Fig. 2.35 and Fig. 2.36. The electromagnetic torque which correspond to 'Connection A' results to be almost 15% greater than the torque obtained with 'Connection B'.
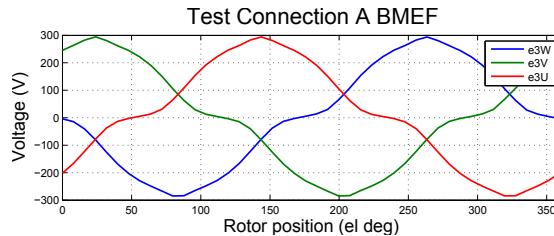
Figure 2.35: BEMF with 'Connection A'
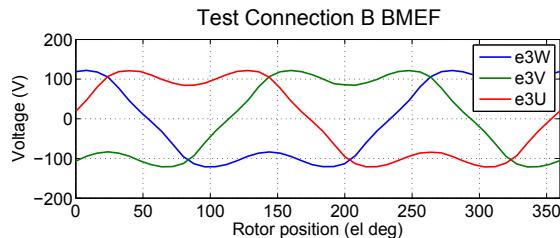
Figure 2.36: BEMF with 'Connection B'

Comparison Between Analytical and FEM

The main analytical and FEM results are collected in Table 2.17 which provides an overview of the two computations ('Connection A').

The analytical values are generally bigger than the FEM computed ones. This is mainly due to the presence of holes in the real magnetic structure of the machine, whose influence is not negligible as it has been shown. It is worth noticing that the analytical model gives a greater value for the synchronous inductance L_s in respect to the FEM model. This is due to the fact that the FEM model does not take the end winding effect into account.

Table 2.17: Comparison between main analytical and FEM results for SFA Motor

Description	Symbol	Analytical	FEM
No Load BEMF	E_0	193 V	180 V
Load Voltage	V	218 V	195 V
Power factor	$\cos\phi$	0.79	0.8
Electromagnetic torque	T	276 kNm	258 kNm
Electromagnetic power	P_{el}	563 kW	526 kW
Total losses at load	$P_{tot,s,load}$	41 kW	40 kW
Synchronous inductance ($\alpha_{ie} = 90$ $el.deg.$)	L_s	1.47 mH	1.20 mH
Q axis inductance $\alpha_{ie} \neq 90$ $el.deg.$	L_q	–	1.16 mH
D axis inductance $\alpha_{ie} \neq 90$ $el.deg.$	L_d	–	0.96 mH
Electromagnetic torque (1160 A)	T	290 kNm	273 kNm

Test Bench Activity Coupled with LW15C

The SFA direct drive motor has been coupled with a LW15 C well known (refer to 2.2) wind generator and tested in Telfs. The torque-current characteristic of the LW15 C generator results to be defined by a second–order relation as per equation (2.64), where T is the torque and I is the current, a and b are two constants which characterizes the machine. The test bench is run and the current which flows in the windings of the SFA motor is chosen. The shaft torque can be obtained by reading the current of the LW15 C generator.

$$I = a * T + b * T^2 \qquad (2.64)$$

In Fig. 2.37 a detail of the measure box used in the rotor of the motor is presented. The temperature of each part of the rotor structure is then read, especially in PMs. In such a way the torque of the motor versus current has been obtained starting from 1100 A up to 1800 A: it is presented in Fig. 2.38. The shaft torque measured at test bench with 1160 A is 270 kNm, while the prediction of FEM model of Table 2.17 is 273 kNm.
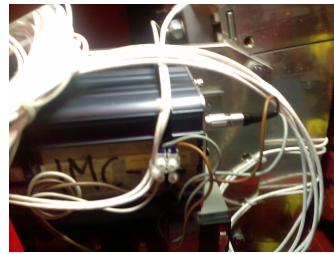
Figure 2.37: Detail of the measure box which rotates together with the rotor
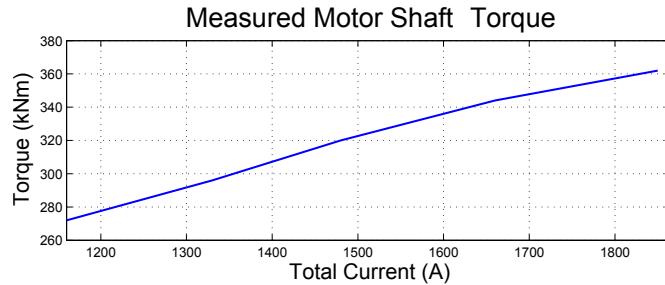
Figure 2.38: Torque characterization of the motor with reference LW15 generator

Modeling and Measure of Rotor Losses

The modeling and measure of the rotor losses are described in in Chapter 3. The Current Sheet Method is employed in FEM analysis. Results and measures are compared.

2.4. LW30A: The New Direct Drive Wind Generator

The structure of the LW30A active part is shown in Fig. 2.39 and Fig. 2.40. This is the new machine developed within this doctoral study. This generator will be installed on the new Leitwind LTW 101 3 MW (Fig. 2.41) wind turbine in Lelystad, the Netherlands, in 2013. More details can be found in [4].

The developing of the magnetic circuit of the new machine has been based on the machine structure with 12 slots in the stator and 10 magnetic poles in the rotor with single layer winding. A proper periodicity has then been chosen in order to fit the large diameter ($\approx 4\ m$).

The main issue which has been considered is the modeling of the rotor losses in order to choose the proper basic machine structure. Some results of the simulations done to define the final structure of the machine are given in this section. The detailed study of the new design will be shown in Chapter 5.

The general characteristics of the machine are listed in Table 5.26.

Figure 2.39: Stator active parts of the LW30A generator

Figure 2.40: Rotor active parts of the LW30A generator

Figure 2.41: Render of Leitwind LW101 wind turbine

Table 2.18: General Characteristics of New LW30A Generator

Generator Characteristics	Symbol	Value	Unit
Number of Slots (basic machine)	Q	12	
Number of Poles (basic machine)	$2p$	10	
Number of Phases	m	3	
Stator Outer Diameter	D_{est}	≈ 4000	mm
Rated Power	P_{gen}	3150	kW

2.4.1. Analytical and FEM Model of the LW30A Generator

The analytical study of the motor is done following the same guidelines and models used for LW15 C generator and SFA motor. To predict the performance of the LW30A generator, the same simplified structure of Fig. 2.2 is used. The winding is a single–layer one. Table 2.19 collects the general inputs to the model.

The FEM study of the final structure of LW30A generator has been done both at load

Table 2.19: General Inputs to Analytical Calculation of LW30A generator

Generator Parameters	Symbol	Value	Unit
Number of Three Phase Systems	N_{line}	1	
Slot Filling Factor	K_{fill}	0.8	
Line Current	I_{line}	4000	A
Total Current	$N_{line}I_{line}$	4000	A
Speed	n	14.3	r/min

and no load. Once again the load analysis is done by feeding the FEM model with the three phase system of currents in equation (2.55), where $I_{line}N_{line}$ represents the total rms current as in 2.1.1, α_{ie} is the angle of the current in respect to the d-axis of the rotor frame reference and θ is the position of the rotor.

Fig. 2.42 represents the map of induction of the model with field lines at load on a stator tooth. It results to be $L_d \neq L_q$ if $\alpha_{ie} \neq 90$ *el.deg.*: an anisotropy between the direct axis and the quadrature axis is present, together with a reluctance torque component on the MTPA trajectory.

To compute the inductances in this load situation equations (2.60) are used. The phase fluxes linkage at no load are shown in Fig. 2.43. The phase fluxes linkage at load are shown in Fig. 2.44. Fig. 2.45 shows the load torque.
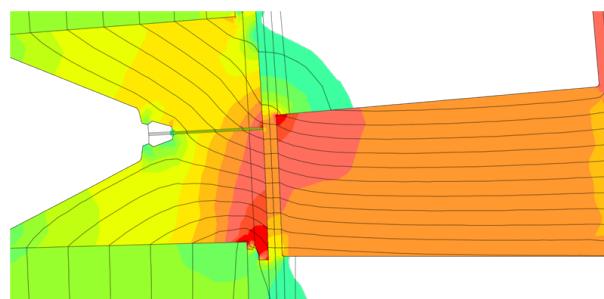
Figure 2.42: LW30A load field map
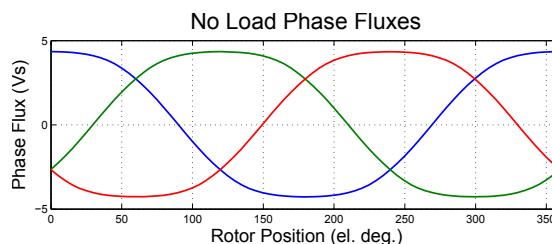
Figure 2.43: Phase Fluxes Linkage at no load
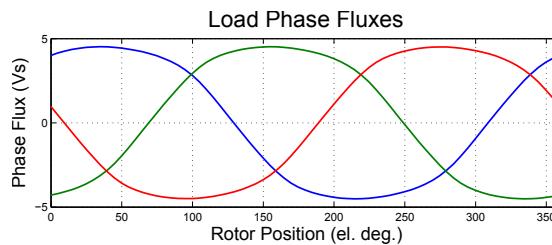
Figure 2.44: Phase Fluxes Linkage at load
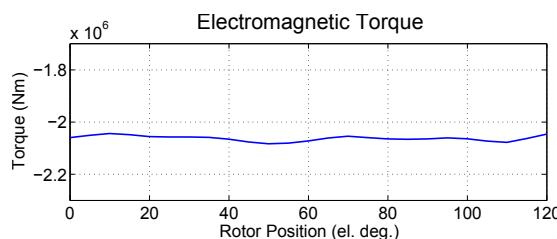
Figure 2.45: Phase Fluxes Linkage at load

Comparison Between Analytical and FEM

The main analytical and FEM results are collected in Table 2.20 which provides an overview of the two computations. More details on the design of this machine will be presented in Chapter 5.

Table 2.20: Comparison between main analytical and FEM results for LW30A generator

Description	Symbol	Analytical	FEM
No Load BEMF	E_0	330 V	306 V
Load Voltage	V	382 V	342 V
Power factor	$\cos\phi$	0.79	0.81
Electromagnetic torque	T	2200 kNm	2030 kNm
Electromagnetic power	P_{el}	3315 kW	3060 kW
Synchronous inductance ($\alpha_{ie} = 90$ $el.deg.$)	L_s	0.95 mH	0.78 mH
Q axis inductance $\alpha_{ie} \neq 90$ $el.deg.$	L_q	–	0.72 mH
D axis inductance $\alpha_{ie} \neq 90$ $el.deg.$	L_d	–	0.61 mH

Test Bench Activity on LW30A generator

The L30A direct drive motor will be tested at B2B test bench in Telfs in the first months of 2013. The previous experience on LW15C generator and SFA motor will be the background to go on with the complete testing of the new machine.

Modeling and Measure of Rotor Losses

The modeling of the rotor losses is described in in Chapter 3. More details on the rotor losses of this machine will be presented in Chapter 5.

Chapter 3

Modeling Of Rotor Losses With The Current Sheet Method

This chapter describes the analysis of the rotor losses in fractional slot permanent magnet machines starting from the analytical point of view and then considering the finite element modeling with the current sheet method. The aim is to focus on large multi polar machine for direct drive applications.

Both the analytical and FEM method are applied first to Halbach rotor structure, then to surface mounted rotor structure (SPM). The topology with interior permanent (IPM) is finally included in the study. Practical example on large permanent magnet motors and generators are considered: they shows that methods employed are suitable to predict rotor losses on large multi polar machine for direct drive applications.

3.1. Analytical relationships on rotor losses

PERMANENT magnet machines with fractional slot winding are usually employed in order to have less active material in the stator, with a considerable cost reduction in respect to full-pitch wound machine. The rotor results to be compact and suitable for placing an high number of poles [11, 17].

In such machines the rotor is built using massive materials like permanent magnets (PMs) themselves, back iron yoke and other structure to support the magnetic elements, especially if modular structure is chosen [18–20]. Parasitic losses are not negligible during machine operations [21, 22].

They are mainly induced by two phenomenon:

- losses induced by slot opening or slotting addendum;
- losses induced by airgap magneto motive force distribution, or MMF addendum;

Solutions with slot openings larger than classical machines ones are often used: the impact of the slotting addendum must be then considered in fractional winding machines [23, 24].

The fractional winding employed leads to harmonic content in term of airgap MMF which includes both higher and lower order harmonic in respect to the fundamental electrical one. During load operations they move asynchronously in respect to the rotor of the machine and then cause parasitic losses in the materials employed in the magnetizing part: the evaluation of the MMF addendum is crucial since the design state in fractional slot PM machines. The basic equation for parasitic losses is the volume integral of the induced joule losses density (3.1):

$$P_{ec} = \int \rho J_r^2 dV = \rho \cdot (-\sigma \cdot \frac{\partial A}{\partial t})^2 \cdot \int dV \qquad (3.1)$$

where J_r is the induced current density, A is the magnetic vector potential, σ is the electric conductivity of the material and the partial derivative of A refers to the time. The study of this phenomenon results to be complex, it can be analytically solved considering simple geometrical configurations and periodical time variations. The basic machine winding with 12 slots and 10 poles in Fig. 4.1 is considered to introduce the study. Table 3.1 summarizes the main characteristics of the geometry of the basic machine.
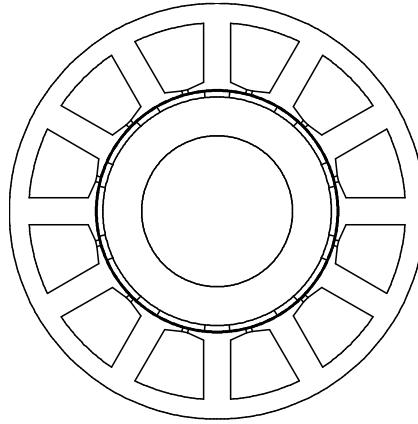
Figure 3.1: Basic machine with 12 slots and 10 poles.

Table 3.1: geometry of the basic 12-10 machine

Quantity		Value
Number of slots Q	–	12
Number of poles 2p	–	10
Stator inner diameter	(mm)	125
Rotor inner diameter	(mm)	77.6
Length	(mm)	100
PM width	(mm)	24.6
PM thickness	(mm)	2.71
Airgap thickness	(mm)	1
Torque	(Nm)	85

3.1.1. Slotting addendum

When the machine runs, the rotor reference frame see a variation of flux density in laminated iron and others massive material parts. This is due to the fact that the equivalent permeability of the magnetic circuit depends on the mechanical position of the rotor. The flux density is then not constant but oscillates around an average value, inducing losses. These losses are due both to hysteresis and eddy current in the laminated iron, and to eddy current only in massive materials. A method to take the slotting addendum into account is proposed in [25]. Basically the frequency of the main harmonic which characterizes this phenomenon is related to the number of slot Q and to the rotational speed n:

$$f_{\Delta B} = \frac{Q \cdot n}{60} \tag{3.2}$$

An analytical estimation of the flux density drop is obtained by adding to the equivalent airgap the thickness of PM t_m:

$$\Delta B = \frac{B_{rem}}{1 + \frac{\mu_r \ g}{t_m}} \left(1 - \frac{1}{1 + \frac{\mu_r \ w_s}{2 \ (t_m + \mu_r \ g)}} \right) \tag{3.3}$$

where B_{rem} is the PM remanent flux, μ_r the PM relative permeability, g is the airgap thickness and w_s is the slot width as in Chapter 2. An equivalent current distribution can be used instead of the actual slot opening geometry starting from ΔB estimated in (3.3). The peak current of the sine wave current density distribution results to be $I_{\Delta B}$ and so the peak value of the corresponding electric load is $\hat{K}_{\Delta B}$:

$$I_{\Delta B} = \frac{\Delta B}{\mu_0} \ \left(g + \frac{t_m}{\mu_r} \right) \tag{3.4}$$

$$\hat{K}_{\Delta B} = \pi \ \frac{I_{\Delta B}}{p_s} \tag{3.5}$$

An evaluation of the impact of the slotting addendum on total losses will be presented in 3.6.2

3.1.2. MMF addendum

The impact of the MMF addendum on losses can be considered starting from literature: many authors studied the phenomenon of the induced losses in the rotor of fractional slot PM machine [11, 26–28].

Special thanks are given to the authors of [25, 29, 30] for providing the straight–lined model and some images. The aim of this study is applying them to large direct drive PM machines. Fig. 3.2 shows the presence of the lower order (sub-harmonic) and higher order (harmonic) terms if the basic 12 slots 10 poles fractional slot PM machine is considered.

The mechanical speed of the generic ν–th MMF harmonic in the stator reference frame
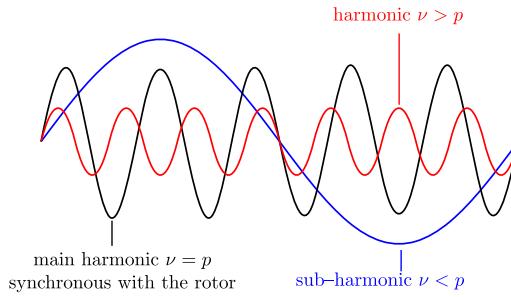
Figure 3.2: MMF harmonics for a basic 12–slot 10–pole machine.

can be computed as

$$\omega_{\nu s} = \frac{\omega}{sgn \cdot \nu} \tag{3.6}$$

where ν is considered without sign, as in [25]. The function sgn assumes the value $+1$ or -1 depending on the ν–th harmonic moves forwards or backwards with respect to the rotor speed. The speed of ν–th MMF harmonic in the rotor reference frame results in

$$\omega_{\nu r} = \left(\frac{\omega}{sgn \cdot \nu} - \frac{\omega}{p} \right) \tag{3.7}$$

The effect on rotor losses is then study for each harmonic starting from the differential formulation of the Ampere's law (3.8) where the magnetic field H is impressed as the source of the induced current density J_r:

$$\nabla H = J_r \tag{3.8}$$

this leads to the following diffusion equation (3.9) in a medium with homogeneous magnetic permeability μ and electrical conductivity σ:

$$\nabla \frac{B}{\mu} - \sigma \cdot \frac{\partial B}{\partial t} = 0 \tag{3.9}$$

considering that $B = \nabla A$ the equation can be rewritten as (3.10)

$$\nabla^2 A - \sigma \mu \cdot \frac{\partial \nabla A}{\partial t} = 0 \tag{3.10}$$

 if a sinusoidal time varying magnetic potential is considered it is then possible to use the phasor transformation (3.11)

$$\nabla^2 \dot{A} - \jmath \omega \mu \sigma \dot{A} = 0 \tag{3.11}$$

basing on [30] a simple straight–lined two–dimensional model is shown in Fig. 3.3. This model considers a medium of height y_m with infinite depth, the reference length is L_x (border effects are neglected). A linear current density $K_s(x)$ with amplitude $\hat{K}_s$ and a wavelength $\tau_\nu = L_x/(2\nu)$ is imposed along the lower surface of the medium, at $y = 0$ in the z–axis direction. The harmonic order ν indicates the number of wavelengths
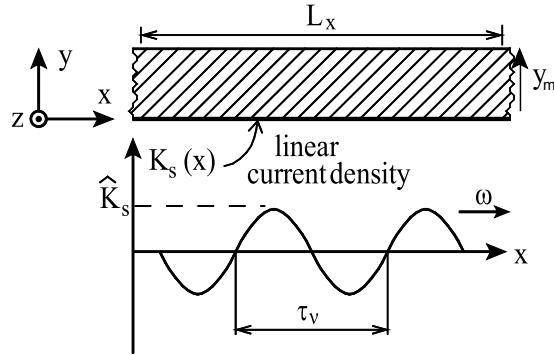
Figure 3.3: Straight–line model for induced losses

contained in the reference length L_x. The speed of the waveform is $v = \omega L_x/(2\pi)$. The linear current density is written using the complex notation is in (3.12).

$$\dot{K}_s(x) = \hat{K}_s e^{\jmath \pi x/\tau_\nu} \tag{3.12}$$

The mathematical solution of the problem can be found in [29]. The specific induced losses per surface unit q on the medium is written as (3.13)

$$q = \frac{\xi^4}{\sqrt[4]{(\pi^4 + \xi^4)^3}} \frac{1}{\cos(\varphi/2)} \frac{\hat{K}_{s\nu}^2}{4\sigma\tau_\nu} k_{ym} \tag{3.13}$$

where ξ is the specific wavelength ($\xi = \sqrt{2}\tau_\nu/\delta$) and δ is the skin depth ($\delta = 1/\sqrt{\pi f_{r\nu}\mu\sigma}$). The angle φ is defined by $\tan \varphi = (\xi/\pi)^2$ and the factor in (3.14)represents a reduction of the power loss density. It decreases towards zero as the wavelength τ_ν decreases with respect to the height of the medium y_m.

$$k_{ym} = 1 - e^{-2\sqrt[4]{\pi^4+\xi^4}\cos(\varphi/2)y_m/\tau_\nu} \tag{3.14}$$

The simple straight–lined model is the elementary layer used to build multi–layers
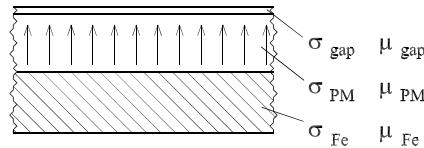
Figure 3.4: Multi–layers model for induced losses

model which are obtained extending the same mathematical equation [29]. The three layers model in Fig. 3.4 explains that concept.

It has been shown that a three–layers model can be easily used to predict the losses in the of a SPM machine with a continuous PM magnet ring and a back iron [27, 29]. Such a structure is shown in Figure Fig. 3.5.

It is possible to use this analytical model even in the computation of the slotting addendum. The corresponding electric load of the related MMF distribution $\hat{K}_{\Delta B}$ has been defined in (3.5), the harmonic order the is equal to the number of slot, i.e. $\nu = Q$, according to (3.2).
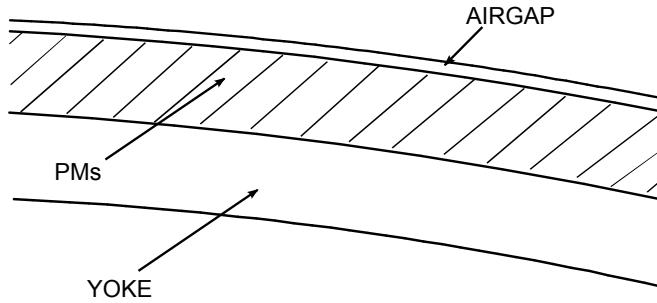
Figure 3.5: Rotor structure with continuous magnetic ring for three-layers model

The aim of the analysis proposed in this chapter is to apply the straight–lined model to large direct drive PMs machine with fractional slot windings. First a large machine with a continuous magnet ring (Halbach structure) is built and losses are computed. The finite element modeling (FEM) of the current sheet is considered and compared with the analytical computations.

In the second step the transition to more realistic surface mounted permanent magnet (SPM) and interior permanent magnet (IPM) topologies is done.

The results of direct measure of the rotor losses on real large machine are then shown and explained. The calorimetric method is employed. Values of the test bench are finally compared with the predicted ones.

3.2. Finite Element modeling of the current sheet

The basic 12 slots, 10 poles machine is considered to introduce the calculation of rotor losses. FEM is applied to model the current sheet: the stator is removed and replaced by a plurality of current points. A time-harmonic FEA simulation is performed and the obtained sheet inject the stator magnetomotive force to the rotor harmonic by harmonic. The winding chosen for the basic machine is the single–layer one with three phases: magnetomotive force, electrical loading harmonics and frequencies seen by the rotor are shown in Fig. 5.3. The material properties used in this first simulation are listed in Table 4.2. From Fig. 4.2, it is worth noticing that back iron has been split in two parts, so as to decrease the size of the mesh elements according to the skin depth of the iron.

Each MMF harmonic is imposed independently and the corresponding rotor losses are computed. Then, the total rotor losses P_{rl} result as the sum of the rotor losses computed for each harmonic order ν, that is:

$$P_{rl} = \sum_{\nu} P_{rl,\nu} \tag{3.15}$$

As an example of computation, Fig. 3.8 shows the flux lines in the rotor of the 12–slot 10–pole PM machine due to the MMF harmonics.

When the machine operates with 78 $\frac{kA}{m}$ electrical loading and 25 r/min speed the computed losses in rotor due to the subharmonic are 18.6 W.
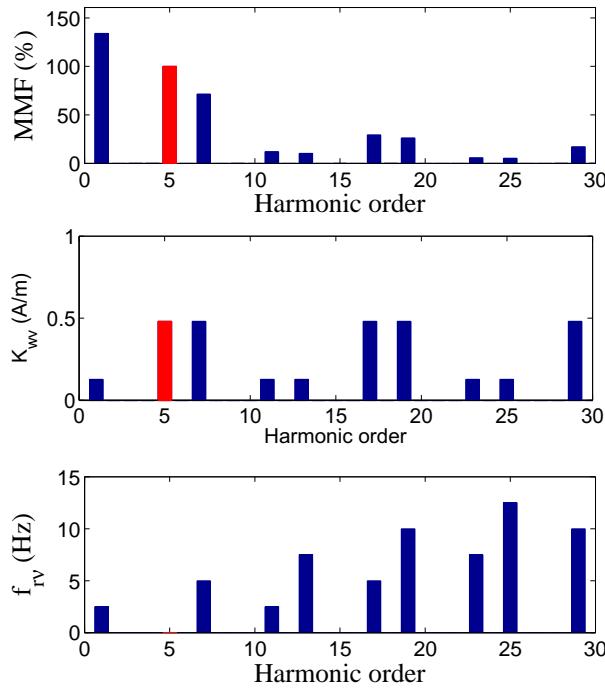
Figure 3.6: Basic winding harmonics characteristics
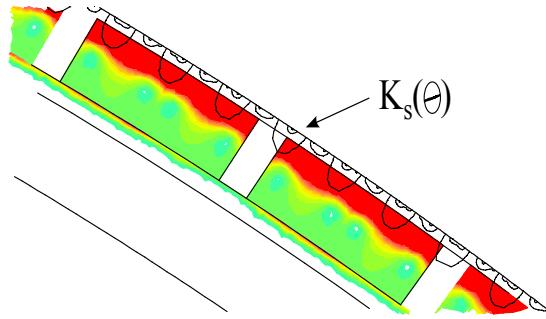
Figure 3.7: The stator is replaced by an equivalent current sheet.

Table 3.2: Material properties used in the model.

Material		PMs	back iron
		NdFeB	linear massive
σ	(MS/m)	0.67	10
μ_r	$(-)$	1.05	5000

In Table 3.3 rotor losses have been calculated for each harmonic and they have been expressed in relation to the losses due to the subharmonic. The frequency f_r seen by the rotor is presented for each harmonic also. It is worth noticing that the losses induced in rotor by harmonics are negligible in respect to the losses induced by the

subharmonic. According to the superimposition in (4.5) the total computed losses are 18.9 W.

An extend study of the rotor losses of the basic machine is presented in Chapter 4, relating this phenomenon to the size of the electrical machine.

Table 3.3: Amount of rotor losses for basic 12–10 machine due to each harmonic

ν	$f_{r\nu}$	$Losses[W]$
1	2.5	18.6
5	0	0
7	5.0	0.19
11	2.5	0
13	7.5	0
17	5.0	0
19	10.0	0.02
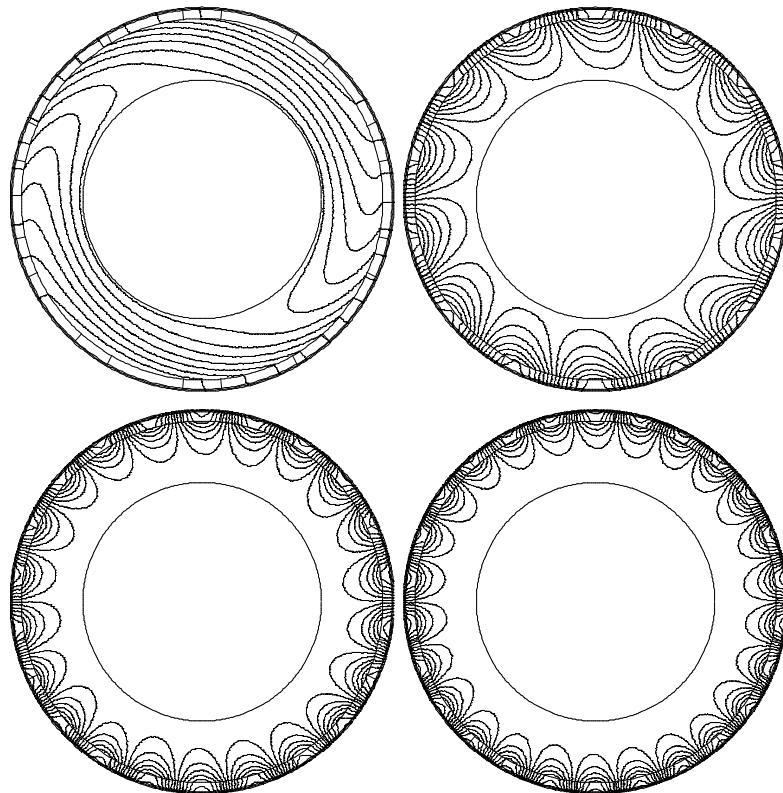
Figure 3.8: Field lines due to the various harmonics.

3.3. FEM model of rotor losses on large SPM machine

In this section the finite element model of the current sheet is applied to the rotor of a large PM machine model based on 12 slots, 10 poles winding. SPM rotor structure is considered as well as single–layer and double–layer winding.

As a first model a structure with a continuous PM ring, surfaced mounted on the rotor yoke with single–layer winding is chosen. The characteristics of materials initially considered are the same presented in Table 4.2. Table 3.4 summarizes the main characteristics of the geometry of the machine. The winding chosen for the basic machine is the single–layer one with three phases: In respect to the 12–10 base one it shifts according to a proper machine periodicity t in order to fit the structure to Table 3.4. Fig. 3.9 shows a detail of the current points employed to build the current

Table 3.4: geometry of the employed 12-10 based SPM machine

Quantity		Value
Number of slots Q (basic winding)	–	12
Number of poles 2p (basic winding)	–	10
Stator inner radius	(mm)	1900
Rotor inner radius	(mm)	1821
Length	(mm)	1000
PM width	(mm)	76
PM thickness	(mm)	29
Airgap thickness	(mm)	5
Current in slot	(A)	9800
Rated Power	(W)	1870000
Speed	(r/min)	14.3
Torque	(Nm)	1250000

sheet and the field lines due to the subharmonic. In this example the machine operates with a 9800 A total current in slot and 14.3 r/min speed. In Table 3.5 rotor losses have
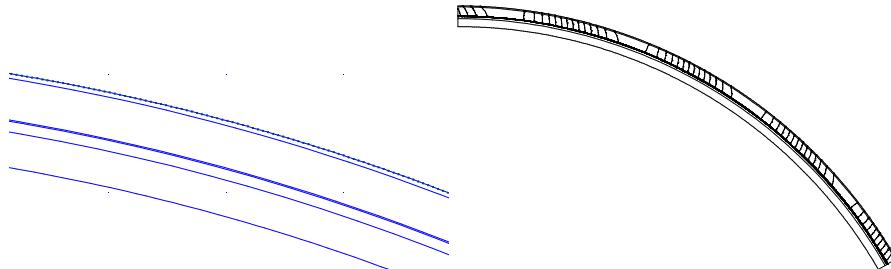
Figure 3.9: Model of the current sheet on large SPM machine

been calculated for each harmonic. The harmonic order has increased according to the machine periodicity. The highest part of the losses are still due to the subharmonic: 173000 W. The total computed losses are 204000 W: the subharmonic causes the 86%

of the total amount of losses.

Others relevant contribute to the losses is given by the first harmonic: it is nearly 13% in respect to the total losses. Almost the 75% of the total losses are induced in the PM ring by the subharmonic. The ring shields the iron yoke from induced losses.

Table 3.5: FEM computed rotor losses, SPM, continuous ring, 12–10 based

$\frac{\nu}{t}$	$f_{r\nu}$ [Hz]	Total [W]	Yoke [W]	PM [W]
1	17.16	172666	22125	150541
5	0	0	0	0
7	34.32	26249	1598	24651
11	17.16	89	10	79
13	51.48	370	14	356
17	34.32	1002	144	858
19	68.64	2235	161	2074
23	51.48	56	11	45
25	85.8	93	12	81
29	68.64	636	159	477
31	103.0	889	165	724
35	85.8	40	12	28
37	120.1	50	12	38
	total	204375	24423	179952

Table 3.6: Analytical computed rotor losses SPM, 12–10 based

$\frac{\nu}{t}$	$f_{r\nu}$ [Hz]	Total [W]	Yoke [W]	PM [W]
1	17.16	169387	17338	152050
5	0	0	0	0
7	34.32	22996	786	22210
11	17.16	68	1	67
13	51.48	319	1	317
17	34.32	694	1	693
19	68.64	1782	1	1781
23	51.48	33	0	33
25	85.8	64	0	64
29	68.64	298	0	298
31	103.0	494	0	494
35	85.8	14	0	14
37	120.1	21	0	21
	total	196298	18128	178170

Other harmonics induce losses which are lower than 100 W (i.e. 0.25% of the total

computed losses) if the harmonic order ν doesn't satisfy equation 3.16:

$$\nu = k \cdot Q \pm p \tag{3.16}$$

where the factor k is a not negative integer number. Harmonics with such an harmonic order are the slot harmonics [31] and their impact can be not negligible because their electrical loading $\hat{K}_s$ is the same of the one of the fundamental. The analytical model of Fig. 3.4 is now employed to perform the same calculation at the same frequency and electrical loading: the results for each harmonics are presented in Table 3.6. The results of the comparison between the finite elements and the analytical model are presented in Table 3.7.

The same procedure is then repeated considering:

- half the current in slot and half the rotor speed (4.9 kA and 7.15 r/min);

- one third of the current in slot and one third of the rotor speed (3.27 kA and 4.76 r/min);

In Table 3.8 rotor losses have been calculated for each harmonic via FEM analysis. The analytical model of Fig. 3.4 is now employed to perform the same calculation at the same frequency and electrical loading. The results for each harmonics are presented in Table 3.9. The results of the comparison between the finite elements and the analytical model are presented in Table 3.10.

Table 3.7: Difference between FEM and analytical losses SPM, 12–10 based

$\frac{\nu}{t}$	Total [%]	Yoke [%]	PM [%]
1	1.9	21.7	-1
5	-	-	-
7	12.4	50.9	9.9
11	23.6	90	15.2
13	13.8	92.9	11
total	4	25.8	1

In Table 3.11 rotor losses have been calculated for each harmonic via FEM analysis. The analytical model of Fig. 3.4 is now employed to perform the same calculation at the same frequency and electrical loading: the results for each harmonics are presented in Table 3.12. The results of the comparison between the finite elements and the analytical model are presented in Table 3.13.
  The comparisons between FEM models and analytical models shows a good accordance in the computed values if the sub-harmonic is considered. The difference between the two computations increases if higher harmonics order are consider.

On the other hand, the sub-harmonic causes the majority of the rotor losses, the difference between total losses computed with FEM and with the analytical model is

Table 3.8: FEM computed rotor losses SPM, 12–10, 4.9 kA and 7.15 r/min

$\frac{\nu}{t}$	Total [W]	Yoke [W]	PM [W]
1	28475	4361	24114
5	0	0	0
7	1693	129	1564
11	7	2	5
13	26	3	23
17	93	28	65
19	183	36	147
23	6	2	4
25	9	3	7
29	83	36	47
31	106	38	68
35	6	3	3
37	7	3	4
total	30694	4643	26051

Table 3.9: Analytical computation of rotor losses SPM, 12–10, 4.9 kA and 7.15 r/min

$\frac{\nu}{t}$	Total [W]	Yoke [W]	PM [W]
1	26977	3761	23217
5	0	0	0
7	1470	70	1399
11	4	0	4
13	20	0	20
17	43	0	43
19	111	0	111
23	2	0	2
25	4	0	4
29	19	0	19
31	31	0	31
35	1	0	1
37	1	0	1
total	28692	3832	24860

within 4% at rated set point, then increases up to 6.5% when half the speed and half the load are considered. If one third the load and one third the speed are chosen the agreement is within 8%.

It is possible to observe that the agreement between FEM and analytical generally gets worse with the reduction of the load of the machine.

Table 3.10: Difference between FEM and analytical SPM, 12–10, 4.9 kA and 7.15 r/min

$\frac{\nu}{t}$	Total [%]	Yoke [%]	PM [%]
1	5.3	13.8	3.7
5	0	0	0
7	13.2	45.7	10.5
total	6.5	17.5	4.6

Table 3.11: FEM computed rotor losses SPM, 12–10, 3.27 kA and 4.76 r/min

$\frac{\nu}{t}$	Total [W]	Yoke [W]	PM [W]
1	8396	1486	6910
5	0	0	0
7	344	33	312
11	2	1	1
13	6	1	5
17	26	10	15
19	47	14	33
23	2	1	1
25	3	1	2
29	28	14	14
31	35	16	19
35	2	1	1
37	2	1	1
total	8893	1579	7314

3.3.1. Different slots–poles configuration

In this example the machine operates with 9.8 kA total current in slot and 14.3 r/min speed: the number of slot is still the same but the number of poles is increased. The basic winding becomes the 24 slots 26 poles one: it will be called basic 12–13. The same permanent magnet mass of the 12–10 configuration is employed. SL winding is chosen at the beginning.

In Table 3.14 rotor losses have been calculated for each harmonic. The analytical model of Fig. 3.4 is now employed to perform the same calculation at the same frequency and electrical loading: the results for each harmonics are presented in Table 3.15. The results of the comparison between the finite elements and the analytical model are presented in Table 3.16.

  Again the same procedure is repeated considering:

- half the current in slot and half the rotor speed (4.9 kA and 7.15 r/min);

- one third of the current in slot and one third of the rotor speed (3.27 kA and 4.76 r/min);

Table 3.12: Analytical computation of rotor losses SPM, 12–10, 3.27 kA and 4.76 r/min

$\frac{\nu}{t}$	Total [W]	Yoke [W]	PM [W]
1	7837	1300	6538
5	0	0	0
7	294	17	277
11	1	0	1
13	4	0	4
17	9	0	9
19	22	0	22
23	0	0	0
25	1	0	1
29	4	0	4
31	6	0	6
35	0	0	0
37	0	0	0
total	8180	1317	6863

Table 3.13: Difference between FEM and analytical SPM, 12–10, 3.27 kA and 4.76 r/min

$\frac{\nu}{t}$	Total [%]	Yoke [%]	PM [%]
1	6.7	12.5	5.4
5	0	0	0
7	14.5	48.5	11.2
total	8	16.6	6.2

The results of the comparison between the finite elements and the analytical model are presented in Table 3.17 and Table 3.18. The sub-harmonics cause the majority of the rotor losses, the difference between total losses computed with FEM and with the analytical model is within 7% in all the load condition considered.

It is possible to observe that the agreement between FEM and analytical is similar in respect to the 12–10 based configuration one.

Table 3.14: FEM computed rotor losses, SPM, continuous ring, 12–13 based

ν	$f_{r\nu}$ [Hz]	Total [W]	Yoke [W]	PM [W]
1	17.16	48792	6323	42470
5	25.74	19449	2183	17266
7	8.58	1322	175	1147
11	34.32	68391	5285	63107
13	0	0	0	0
17	42.9	842	39	804
19	8.58	16	3	13
23	51.48	139	5	135
25	17.16	14	2	12
29	60.06	123	5	118
31	25.74	38	6	32
35	68.64	2940	161	2779
37	34.32	773	141	633
41	77.22	95	7	88
43	42.9	19	4	15
47	85.8	27	3	24
49	51.48	11	3	9
53	94.38	33	4	29
55	60.06	28	7	21
59	102.9	1006	163	843
61	68.6	563	157	406
65	111.5	39	8	32
67	77.2	14	4	10
71	120.1	13	3	10
73	85.8	9	3	6
total		144698	14691	130007

3.3.2. Effect of the erasing of the continuous magnet ring

The amount of losses is extremely huge in the models with continuous magnet ring, because it represents the 10.7% of the rated power. The effects of materials and geometry are then investigated to define a realistic SPM configuration for large direct drive generators. The continuous magnet ring is then replaced by discrete permanent magnets blocks in order to study the difference in the induced losses. The machine still operates with 9.8 kA total current in slot and 14.3 r/min speed. In Table 3.19 losses for each harmonic are computed: the shielding effect of the ring on the yoke is now practically erased because it has the majority of losses now. The total amount of losses has decreased in respect to the continuous magnet ring case: 144000 W instead of 204000 W which corresponds to -29%.

Almost the whole losses are induced by the subharmonic in the rotor yoke (85%) while half the losses in PMs are induced by the harmonic with $\frac{\nu}{t} = 7$. In rotor yoke the losses results to be confined in a very tight region immediately below the PMs. Slot

Table 3.15: Analytical computed rotor losses SPM, 12–13 based

$\frac{\nu}{t}$	$f_{r\nu}$ [Hz]	Total [W]	Yoke [W]	PM [W]
1	17.16	48770	5048	43721
5	25.74	17987	1414	16573
7	8.58	1245	148	1097
11	34.32	63270	2996	60273
13	0	0	0	0
17	42.9	785	17	767
19	8.58	12	0	12
23	51.48	129	1	128
25	17.16	10	0	10
29	60.06	111	0	111
31	25.74	27	0	27
35	68.64	2577	2	2575
37	34.32	517	0	517
41	77.22	80	0	80
43	42.9	12	0	12
47	85.8	21	0	21
49	51.48	6	0	6
53	94.38	24	0	24
55	60.06	14	0	14
59	102.9	653	0	653
61	68.6	250	0	250
65	111.5	23	0	23
67	77.2	6	0	6
71	120.1	7	0	7
73	85.8	3	0	3
total		137000	9600	127000

Table 3.16: Difference between FEM and analytical losses SPM, 12–13 based

$\frac{\nu}{t}$	Total [%]	Yoke [%]	PM [%]
1	0	20.2	-2.9
5	7.5	35.2	4
7	5.8	15.4	4.4
11	7.5	43.3	4.5
13	0	0	0
17	6.8	56.4	4.6
total	5.6	34.5	2.4

harmonics have still an higher contribute in respect to other harmonics, especially in PMs where they cause the 58% of the total losses.

Table 3.17: Difference between FEM and analytical SPM, 12–13, 4.9 kA and 7.15 r/min

$\frac{\nu}{t}$	Total [%]	Yoke [%]	PM [%]
1	1.6	10.4	-0.1
5	6.7	20.1	4.6
7	5.7	13.3	4.1
11	6.8	29.9	4.6
13	0	0	0
17	9.1	50	5.9
total	4.8	19.7	2.4

Table 3.18: Difference between FEM and analytical SPM, 12–13, 3.27 kA and 4.76 r/min

$\frac{\nu}{t}$	Total [%]	Yoke [%]	PM [%]
1	1.9	8.1	0.5
5	5.9	13	4.7
7	5.6	25	0
11	6.8	26.7	4.7
13	0	0	0
17	9.1	100	0
total	4.5	15.5	2.3

Table 3.19: Amount of rotor losses SPM, discrete PMs blocks, 12–10 based

$\frac{\nu}{t}$	$f_{r\nu}$ [Hz]	Total [W]	Yoke [W]	PM [W]
1	17.16	122267	109626	12641
5	0	0	0	0
7	34.32	15665	1806	13860
11	17.16	71	16	55
13	51.48	304	36	269
17	34.32	944	347	597
19	68.64	2091	547	1545
23	51.48	62	32	30
25	85.8	100	41	59
29	68.64	836	525	310
31	103.0	1139	615	523
35	85.8	59	41	18
37	120.1	75	48	27
total		143613	113679	29934

3.3.3. Effect of the segmentation of PMs

In order to reduce the amount of losses in PMs they are electrically segmented in two parts, along the radial direction, results are presented in Table 3.20. It is worth noticing

Table 3.20: Impact of the segmentation of PMs, SPM, 12–10 based

$\frac{\nu}{t}$	$f_{r\nu}$ [Hz]	Total [W]	Yoke [W]	PM [W]
1	17.16	114456	111180	3277
5	0	0	0	0
7	34.32	7507	1799	5708
11	17.16	51	16	36
13	51.48	241	36	205
17	34.32	905	354	551
19	68.64	2050	576	1474
23	51.48	61	33	28
25	85.8	98	44	54
29	68.64	809	551	258
31	103.0	1107	664	443
35	85.8	57	44	13
37	120.1	72	52	20
	total	127000	115000	12000

that losses in PMs are -60% lower in respect to the previous case with integer magnets (Table 3.19). The losses induced in the iron yoke tend to remain constant instead. Results are presented in Table 3.20. The evaluation of the impact of the segmentation of PMs is done on 12–13 configuration as well, results are presented in Table 3.21.

3.3.4. Effect of the saturation of the iron yoke

In order to establish the effect of the saturation of the iron yoke the relative permeability is set down to $\mu_r = 50$: if the frequency of each harmonic is fixed (i.e. the machine is running at a constant speed) the related skin depth increases by a $\sqrt{\frac{5000}{50}}$ factor, which is 10 times the skin depth with $\mu_r = 5000$. Magnets are still split in two segments along the radial direction.

Losses decrease and tend to have a more uniform distribution in the rotor yoke on a larger surface with a realistic value of magnetic induction. In Table 3.22 the total losses (yoke and PMs) are computed again and compared: if the subharmonic is considered they have -41% reduction, while the losses induced by the first harmonic strongly increase(+63%). This is due to the fact that this harmonic can now penetrates deeper, inducing losses in a very tight area of the yoke.Losses induced by other harmonics tend to be constant in PMs, while they reduces in the yoke: the sum of the two contributions finally tends to reduce. Table 3.23 presents the computed losses with $\mu_r = 50$ yoke permeability for the different part of the rotor.

Table 3.21: Impact of the segmentation of PMs, SPM, 12–13 based

$\frac{\nu}{t}$	$f_{r\nu}$ [Hz]	Total [W]	Yoke [W]	PM [W]
1	17.16	140341	139718	623
5	25.74	3256	2866	390
7	8.58	215	175	41
11	34.32	11859	5563	6296
13	0	0	0	0
17	42.9	249	51	198
19	8.58	7	4	4
23	51.48	66	11	55
25	17.16	9	4	5
29	60.06	77	14	63
31	25.74	29	13	16
35	68.64	2264	551	1713
37	34.32	711	353	358
41	77.22	85	27	58
43	42.9	20	11	9
47	85.8	27	11	16
49	51.48	13	8	5
53	94.38	36	17	19
55	60.06	34	23	11
59	102.9	1193	677	515
61	68.6	746	546	201
65	111.5	51	32	18
67	77.2	20	16	5
71	120.1	18	13	5
73	85.8	13	11	2
	total	161000	151000	10000

3.3.5. Effect of using the double layer winding

A double–layer (DL) stator winding is then considered starting from the case of a saturated iron yoke ($\mu_r = 50$): magnetomotive force and electrical loading harmonics are shown in Fig. 3.10. The total slot current is fixed, while the electrical loading of the fundamental of the configuration with double layer reduces in respect to the single–layer one. This is due to the fact that the winding factor k_w reduces from 0.966 down to 0.933. It is worth noticing that the subharmonic deeply decreases both in MMF content and electrical loading $\hat{K}_s$, as per Table 3.24.

In Table 3.24 the total losses (yoke and PMs) are computed again and compared: if the subharmonic is considered they have -93% reduction. Generally, the losses induced by slot harmonics have -7% reduction, the other harmonics have -93% reduction. Losses have -77% reduction in total. The total rotor losses computed for the machine in Table 3.4 with double–layer winding, the segmented magnet and saturated yoke represent the 1% of the rated power.

Table 3.22: Impact of saturation, SPM, 12–10 based: comparison with Table 3.20, total losses

$\frac{\nu}{t}$	$f_{r\nu}$ [Hz]	$u_r = 500$ [W]	$u_r = 50$ [W]	$Difference$ [W]
1	17.16	114456	67745	-41%
5	0	0	0	
7	34.32	7507	12263	63%
11	17.16	51	49	-5%
13	51.48	241	224	-7%
17	34.32	905	635	-30%
19	68.64	2050	1582	-23%
23	51.48	61	35	-43%
25	85.8	98	64	-35%
29	68.64	809	379	-53%
31	103.0	1107	584	-47%
35	85.8	57	23	-60%
37	120.1	72	32	-56%
	total	127000	84000	-34%

Table 3.23: Impact of the saturation: $u_r = 50$ yoke permeability, 12–10 based

$\frac{\nu}{t}$	$f_{r\nu}$ [Hz]	$Total$ [W]	$Yoke$ [W]	PM [W]
1	17.16	67745	67285	460
5	0	0	0	0
7	34.32	12263	6820	5443
11	17.16	49	14	36
13	51.48	224	21	203
17	34.32	635	93	542
19	68.64	1582	141	1441
23	51.48	35	8	27
25	85.8	64	11	53
29	68.64	379	130	250
31	103.0	584	164	419
35	85.8	23	11	12
37	120.1	32	13	18
	total	84000	75000	8900

If the rotor yoke is massive it is mandatory to choose the double–layer winding instead of the single layer one in order to have an acceptable level of rotor losses.
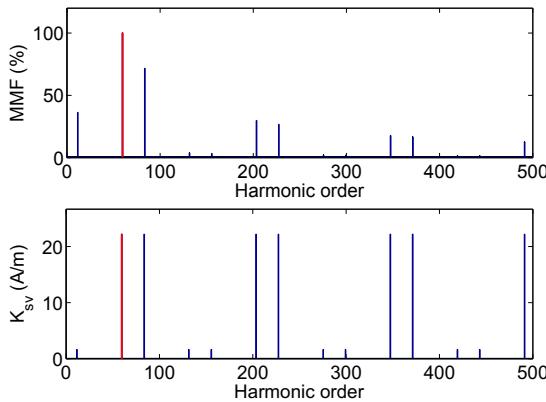
Figure 3.10: Chosen double layer winding harmonics characteristics, 12–10 based

Table 3.24: Impact of the DL winding SPM, 12–10 based

$\frac{\nu}{t}$	$\hat{K}_s$ DL [%]	$TotalDL$ [W]	$TotalSL$ [W]	$Difference$ [%]
1	-27	4538	67745	-93%
5	-4	0	0	
7	-4	11441	12263	-7%
11	-27	3	49	-93%
13	-27	15	224	-93%
17	-4	593	635	-7%
19	-4	1476	1582	-7%
23	-27	2	35	-93%
25	-27	4	64	-93%
29	-4	354	379	-7%
31	-4	545	584	-7%
35	-27	2	23	-93%
37	-27	2	32	-93%
	total	19000	84000	-77%

3.3.6. Model for laminated magnetic yoke

The FEM model for losses adopted for machine in Table 3.4 is then modified: the non-linear characteristic of M–530 magnetic steel is chosen for the rotor yoke. SL winding is employed. The corresponding $B(H)$ characteristic is shown in Fig. 3.11, material is still massive. Once again magnets are segmented and single–layer winding are employed in order to compute rotor losses. Results of the computation are shown in Table 3.25. The histogram of total losses related to Table 3.25 is shown in Fig. 3.12 for each harmonic. Result for total losses is within the values obtained for $u_r = 5000$ and $u_r = 50$: that means that the equivalent saturation of the iron yoke is within these values. The closest value is the one obtained with $u_r = 5000$, which is the highest one. The thickness of the lamination of the iron yoke is then set to $1mm$ and simulation is repeated. Results of the computation are shown in Table 3.26. The rotor losses represent the 1.5% of the rated power of the machine. This is a reasonable value if compared with the case of
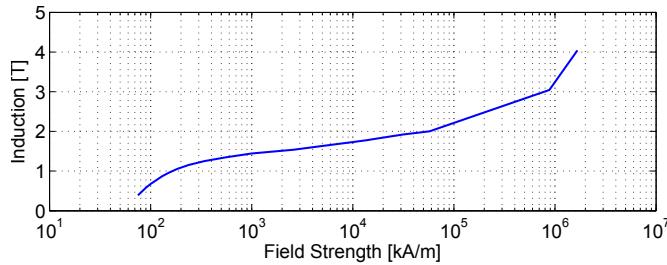
Figure 3.11: $B(H)$ semilogarithmic characteristic of the laminated steel

Table 3.25: Model with nonlinear yoke for 12–10 based SPM machine, M–530 steel

$\frac{\nu}{t}$	$f_{r\nu}$ [Hz]	$Total$ [W]	$Yoke$ [W]	PM [W]
1	17.16	101455	100765	690
5	0	0	0	0
7	34.32	7485	1793	5691
11	17.16	51	15	36
13	51.48	239	35	205
17	34.32	868	317	551
19	68.64	2046	570	1475
23	51.48	59	32	28
25	85.8	97	43	54
29	68.64	806	548	258
31	103.0	1109	665	444
35	85.8	56	43	13
37	120.1	71	51	20
	total	114342	104877	9465
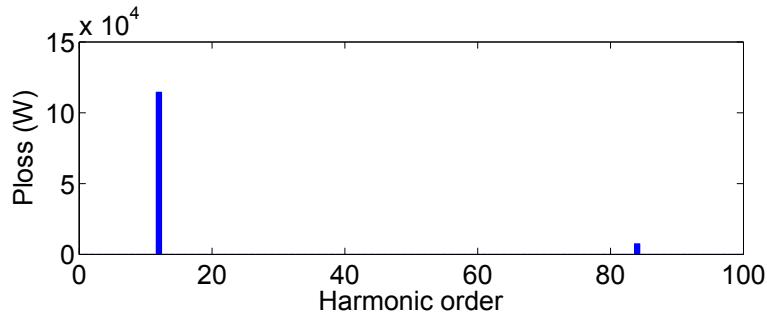
Figure 3.12: Histogram of losses related to Table 3.26 for not-linear yoke model

the massive saturated iron yoke in Table 3.23: rotor losses are the 4.5% of the rated power.

It is worth noticing that the lamination of the rotor yoke is mandatory if single layer winding is employed in this machine. This model will be called SPMA: the histogram of total losses related to Table 3.26 is shown in Fig. 3.13 for each harmonic. The

Table 3.26: Model with nonlinear yoke for 12–10 based SPM machine, laminated

$\frac{\nu}{t}$	$f_{r\nu}$ [Hz]	$Total$ [W]	$Yoke$ [W]	PM [W]
1	17.16	5902	1054	4848
5	0	0	0	0
7	34.32	7742	2000	5741
11	17.16	83	47	36
13	51.48	368	161	207
17	34.32	2546	1983	563
19	68.64	4499	2918	1581
23	51.48	191	161	30
25	85.8	271	211	60
29	68.64	3217	2918	300
31	103.0	4020	3451	569
35	85.8	230	211	19
37	120.1	278	247	31
	total	29348	15363	13984
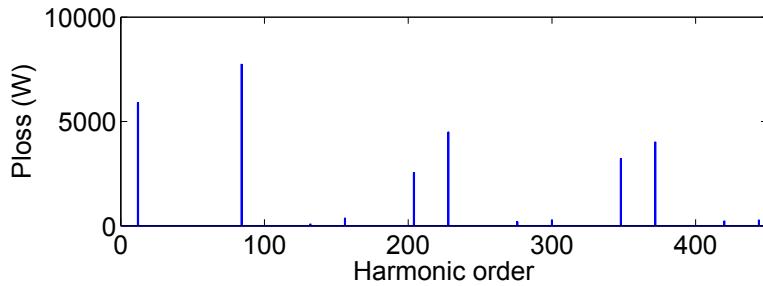
Figure 3.13: Histogram of losses related to Table 3.26 for SPMA model

lamination of the magnetic steel yoke is then considered to be made with infinitesimal thickness sheets: this is simulated by setting the electrical conductivity of the material down to $0MS$. Results are presented in Table 3.27: losses in PMs are induced only. This model will be called SPMB. It is worth noticing that losses in the PMs of SPMA model and SPMB model are nearly the same for each harmonic order.

A different assumption on the structure of the rotor yoke is then made in model SPMC. The yoke is hybrid: half laminated (the part which is closer to PMs) and half massive in order to obtain an intermediate structure, which is more reliable from a technical point of view.

Lamination is here simulated through infinitesimal thickness sheets: like in SPMB this is simulated by setting the electrical conductivity of the material down to $0MS$. Fig. 3.14 presents the rotor structure of SPMC. Computed losses for each harmonic are presented in Table 3.28: it is worth noticing that losses in iron yoke tend to be negligible in respect to the losses in PMs for independently from the harmonic order. It is worth noticing that in SPMA–B–C the subharmonic does not induce the majority of losses as

Table 3.27: Comparison losses in PMs, SPM, 12–10, zero conductivity vs laminated yoke

$\frac{\nu}{t}$	$f_{r\nu}$ [Hz]	Laminated [W]	0conductivity [W]	Difference [%]
1	17.16	4848	4851	0.04%
5	0	0	0	
7	34.32	5741	5741	-0.01%
11	17.16	36	36	0.00%
13	51.48	207	207	0.02%
17	34.32	563	563	-0.09%
19	68.64	1581	1580	-0.10%
23	51.48	30	30	0.12%
25	85.8	60	60	0.29%
29	68.64	300	298	-0.40%
31	103.0	569	567	-0.25%
35	85.8	19	19	0.91%
37	120.1	31	32	1.50%
total		13984	13982	-0.02%

in the SPM structure presented in Table 3.25 (with massive not linear magnetic rotor back iron): this is due to the fact that losses are limited in yoke by lamination or by the reduction to zero of the electrical conductivity.
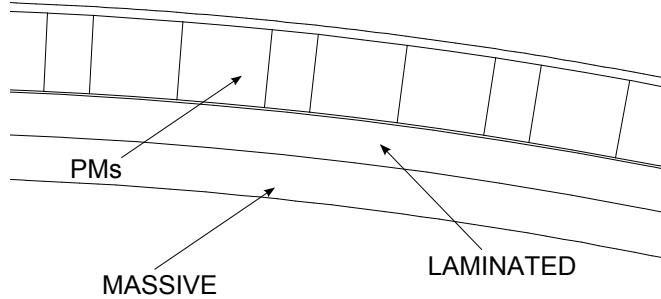
Figure 3.14: Hybrid rotor structure for SPMC model

3.3.7. Impact of the total current in slot

In this paragraph the models for SPMA–B–C (12–10 configuration) are considered at fixed $14.3 r/min$ rotor speed. The total current in slot varies to one third and half of the initial value which is $9800A$. Fig. 3.15 shows the behavior of total rotor losses at fixed rotor speed in SPM models. The quantities due to the subharmonic ($\nu = 1$) and to the first harmonic ($\nu = 7$) are also shown. Table 3.29 presents the total computed values in each material of the rotor. The total losses in PMs are the same in each model under study if the same total current in slot is considered. In model SPMA losses in the iron yoke are almost half of the total losses, while they are negligible in

Table 3.28: Model with hybrid yoke for 12–10 based SPM machine

$\frac{\nu}{t}$	$f_{r\nu}$ [Hz]	$Total$ [W]	$Yoke$ [W]	PM [W]
1	17.16	4825	23	4802
5	0	0	0	0
7	34.32	5775	37	5738
11	17.16	38	3	36
13	51.48	209	3	207
17	34.32	598	37	562
19	68.64	1611	37	1575
23	51.48	32	3	29
25	85.8	62	3	60
29	68.64	332	37	295
31	103.0	596	37	559
35	85.8	21	3	19
37	120.1	34	3	32
total		14134	222	13913
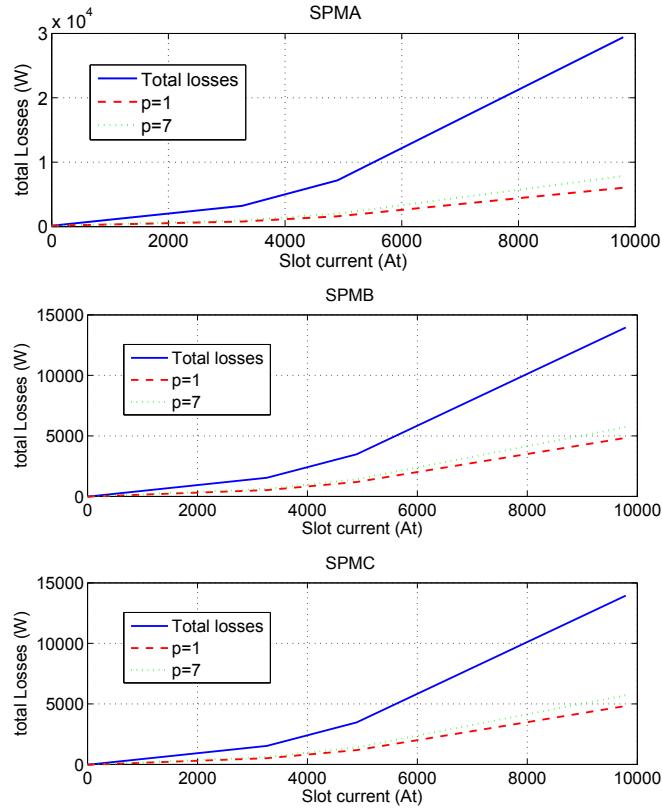
Figure 3.15: Behavior of rotor losses at fixed rotor speed in SPMA–B–C models

model SPMC. It is possible to notice that the behavior of losses in PMs is proportional (i.e. similar) to the total losses computed for SPMA model: they vary with the second

Table 3.29: Computed rotor losses at fixed rotor speed in SPM models

Slot Current [kA]	Yoke [W]	PMs [W]	Total [W]
SPMA			
0	0	0	0
3267	1545	1553	3098
4900	3563	3494	7057
9800	15363	13984	29348
SPMB			
0	0	0	0
3267	0	1554	1554
4900	0	3497	3497
9800	0	13982	13982
SPMC			
0	0	0	0
3267	24	1549	1574
4900	54	34885	3541
9800	222	13913	14134

power of the total current in slot.

Then model SPMB is suitable to describe a qualitative characteristic of losses against the total current in slot. Fig. 3.16 shows the behavior of total rotor losses at fixed rotor speed in SPM models including the quantities due to each material of the rotor.
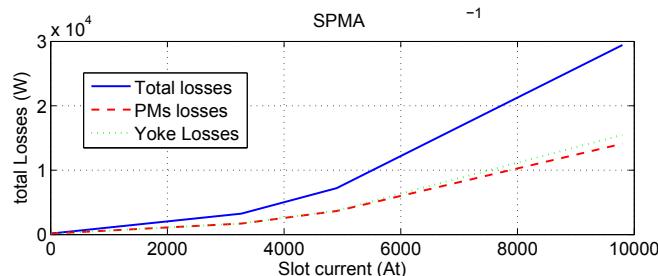
Figure 3.16: Losses contributions at fixed rotor speed in SPMA model

3.3.8. Impact of the rotor speed

In this paragraph the models for SPM are considered at fixed $9800At$ total current in slot. The rotor speed varies to one third and half of the initial value which is $14.3 r/min$.

Fig. 3.17 shows the behavior of total rotor losses at fixed total current in slot for SPMA–B–C models. The quantities due to the subharmonic ($\nu = 1$) and to the first harmonic ($\nu = 7$) are also shown. Table 3.30 presents the total computed values in each material of the rotor.   The total losses in PMs are the same in each model under study if the same rotor speed is considered. In model SPMA only losses in the iron yoke are almost half of the total losses at $14.3 r/min$.
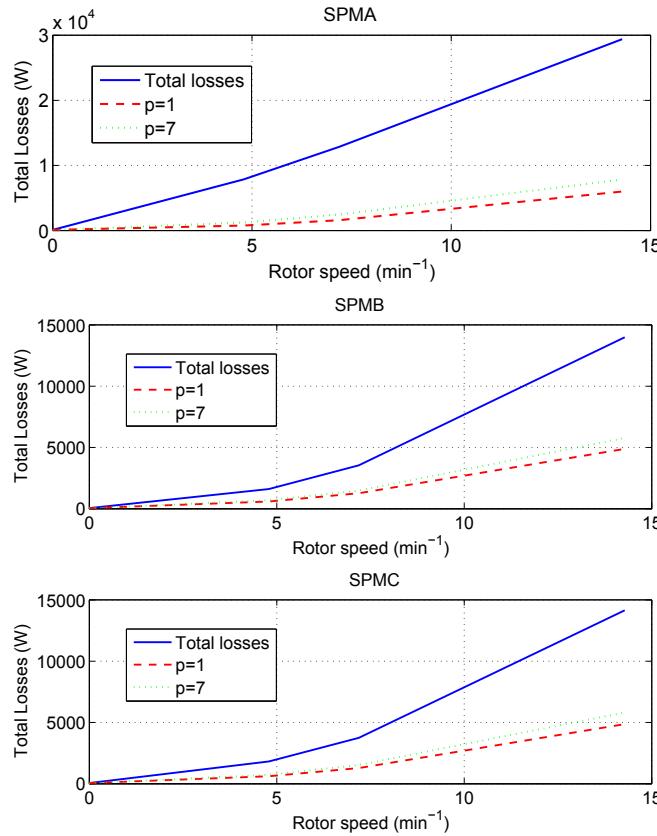
Figure 3.17: Behavior of rotor losses at fixed total current in slot in SPMA–B–C models

Table 3.30: Computed rotor losses at fixed total slot current in SPMA–B–C models

Slot Current [kA]	Yoke [W]	PMs [W]	Total [W]
SPMA			
0	0	0	0
4.8	6208	1556	7763
7.2	9285	3499	12784
14.3	15364	13984	29348
SPMB			
0	0	0	0
4.8	0	1554	1554
7.2	0	3497	3497
14.3	0	13982	13982
SPMC			
0	0	0	0
4.8	219	1547	1766
7.2	221	3480	3700
14.3	222	13913	14134

If another rotor speed is considered, they tend to decrease much slower with speed in respect to the losses in PMs. The losses in rotor yoke vary with the square of the rotor speed, while losses in PMs are linear in respect to the square root of the rotor speed. It can be also noticed that in model SPMC (hybrid iron yoke) losses in the iron yoke are almost constant in respect to the rotor speed: they are not negligible at low speed (Table 3.30).

Fig. 3.18 shows the behavior of total rotor losses at fixed total Current in Slot in SPMA model including the quantities due to each material of the rotor. This time the behavior of total losses in PMs is not proportional to the total losses computed for SPMA model, because the losses in rotor yoke decreases slower with speed in respect to the losses in PMs.
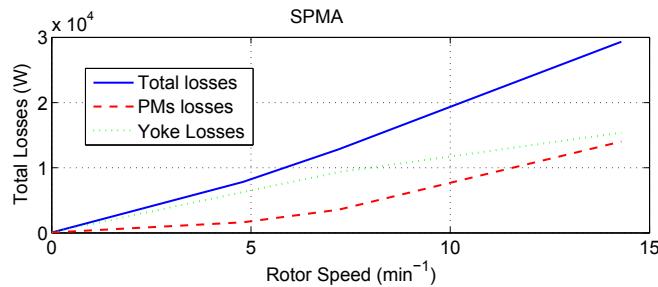
Figure 3.18: Losses contributions at fixed total current in slot in SPMA model

3.4. Finite Element Modeling of Rotor Losses on large IPM machine model

In this section the finite element model of the current sheet is applied to the rotor of a large interior permanent magnet (IPM) machine model with based on 12–10 structure. Both single–layer and double–layer windings are considered. The single–layer winding is used in the first model as well as the segmentation of PMs in two blocks, along the circumferential direction (Fig. 3.19). The winding and the permanent magnets of the IPM model are the same used in the SPM model of section 3.3:the machine operates with 9800 A total current in slot and 14.3 r/min rotor speed. Materials characteristic initially considered are the presented in Table 3.31. Table 3.32 summarizes the main

Table 3.31: Material properties used in the IPM model.

Material	PMs	yoke	aluminium
	NdFeB	linear massive	linear massive
σ (MS/m)	0.67	10	25
μ_r $(-)$	1.05	5000	1

characteristics of the geometry of the machine. The rated torque increases up to 30% more in respect to the SPM topologies with the same mass of PMs.

Table 3.32: geometry of the employed 12-10 based IPM machine

Quantity		Value
Number of slots Q (basic winding)	–	12
Number of poles 2p (basic winding)	–	10
Stator inner radius	(mm)	1900
Rotor inner radius	(mm)	1800
Length	(mm)	1000
PM width	(mm)	76
PM thickness	(mm)	29
Airgap thickness	(mm)	5
Current in slot	(A)	9800
Rated Power	(W)	2410000
Speed	(r/min)	14.3
Torque	(Nm)	1610000
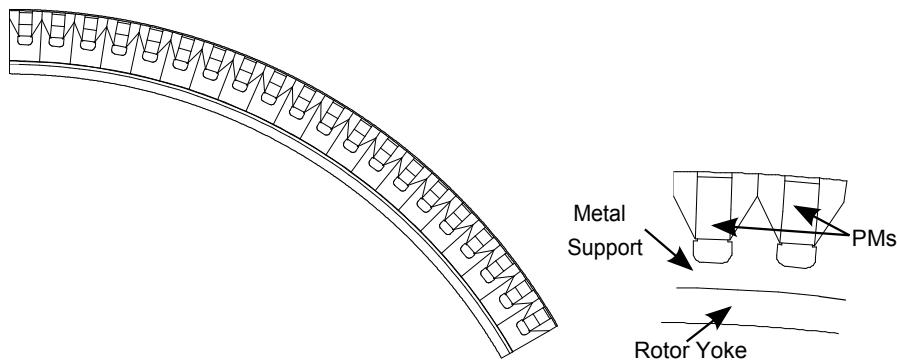
Figure 3.19: Model of the IPM structure

The histogram of total losses related to Table 3.33 is shown in Fig. 3.20 for each harmonic. Rotor losses have been calculated for each harmonic. The highest part of the losses are due to the subharmonic, 7000 W, and to the first harmonic, 7600 W. The total computed losses are 15000 W: the subharmonic causes the 44% of the total amount of losses, while the first harmonic provides half the total amount. Other contributions which are higher than 0.5% are given by the slot harmonics $\nu = 17$ and $\nu = 19$. The highest amount of losses is induced in the aluminium support of the magnetic poles: 66% of the total losses. The remaining losses are almost induced in PMs, while losses in the magnetic iron yoke are not presented in Table 3.33 because they are negligible. This is due to the shielding effect of the aluminium support, which does not allow any harmonic to seriously penetrate in the yoke.
It is worth noticing that the subharmonic does not induce the majority of losses as in the SPM structure presented in Table 3.25 (with not linear magnetic rotor back iron). The first harmonic gives a slightly higher contribute to the losses in rotor. A double–layer stator winding is then considered starting from the case of a saturated iron yoke: the total slot current is fixed, while the electrical loading of the fundamental of the

Table 3.33: FEM computed rotor losses, IPM, 12–10 based

$\frac{\nu}{t}$	$f_{r\nu}$ [Hz]	Total [W]	Support [W]	PM [W]
1	17.16	6979	5631	1345
5	0	0	0	0
7	34.32	7606	4032	3544
11	17.16	13	3	8
13	51.48	36	2	31
17	34.32	152	29	93
19	68.64	343	28	285
23	51.48	10	2	6
25	85.8	15	3	10
29	68.64	78	12	36
31	103.0	111	17	65
35	85.8	6	1	3
37	120.1	8	1	4
	total	15356	9760	5430
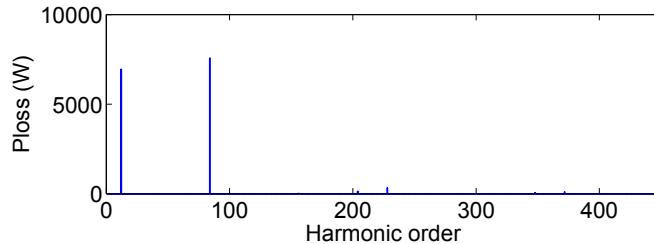
Figure 3.20: Histogram of losses related to Table 3.33 for IPM model

configuration with double layer reduces in respect to the single–layer one because the winding factor k_w drops from 0.966 down to 0.933. It is worth noticing again that the subharmonic deeply decreases both in MMF content and electrical loading $\hat{K}_s$.

In Table 3.34 the total losses (yoke and PMs) are computed: if the subharmonic is considered they have -93% reduction. Losses due to the first harmonic tend to be constant. Losses have -48% reduction in total. The histogram of total losses related to Table 3.34 is shown in Fig. 3.21 for each harmonic. It highlights that once again with the double–layer winding the effect of the sub-harmonic is practically erased in comparison to the single–layer solution.

Table 3.34: FEM computed rotor losses, IPM, DL, 12–10 based

$\frac{\nu}{t}$	$f_{r\nu}$ [Hz]	Total [W]	Support [W]	PM [W]
1	17.16	470	379	90
5	0	0	0	0
7	34.32	7067	3758	3307
11	17.16	1	0	1
13	51.48	2	0	2
17	34.32	115	27	87
19	68.64	294	26	266
23	51.48	1	0	0
25	85.8	1	0	1
29	68.64	46	11	33
31	103.0	77	16	60
35	85.8	0	0	0
37	120.1	0	0	0
total		8074	4217	3848
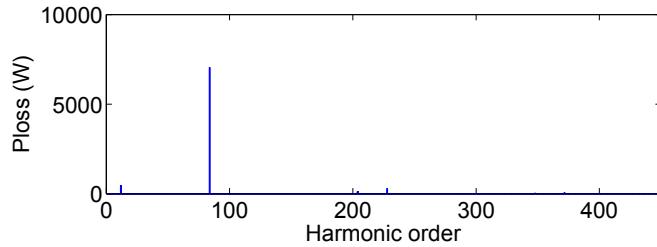
Figure 3.21: Histogram of losses related to Table 3.34 for IPM model with double–layer

3.4.1. Impact of the airgap thickness

The effect of the airgap thickness g is here considered using SL winding: losses are computed again with $g' > g$. The difference between the two airgap thicknesses employed is 2 mm. There is "low pass" effect of the airgap: the reduction on the losses due to the subharmonic is lower than 5% and the main effect is on the first harmonic, whose induced losses are almost 30% lower.

The sum of the losses due to both the harmonics is almost 30% lower in PMs and 10% lower in the metal yoke. It is worth noticing that losses in PMs are the more affected by the employing a larger airgap because they are mainly due by the first harmonic. Results of the comparison are shown in Table 3.35 and Table 3.36.

Table 3.35: Impact of the airgap thickness: harmonic order

$\frac{\nu}{t}$	Part	Losses g	Losses g'	Difference
		(kW)	(kW)	(%)
1	PM	1.4	1.36	-3
1	SUPPORT	5.6	5.35	-4.5
1	PM+SUPPORT	7.0	6.71	-4.1
7	PM	3.5	2.1	-40.0
7	SUPPORT	4.0	2.2	-45.0
7	PM+SUPPORT	7.5	4.5	-36.0

Table 3.36: Impact of the airgap thickness: material

Part	Losses g	Losses g'	Difference
	(kW)	(kW)	(%)
PM	4.9	3.5	-30.0
SUPPORT	9.6	8.6	-10.0
PM+SUPPORT	14.5	12.1	-17.0

3.4.2. Impact of the total current in slot

In this paragraph the models for IPM are considered at fixed $14.3 r/min$ rotor speed. The total current in slot varies to one third and half of the initial value which is $9800 At$. Fig. 3.22 shows the behavior of total rotor losses at fixed rotor speed in IPM model. The quantities due to the subharmonic ($\nu = 1$) and to the first harmonic ($\nu = 7$) are also shown.

Table 3.37 presents the total computed values in each material of the rotor. It is worth noticing that losses in PMs are almost due to the harmonic $\nu = 7$ while losses in the metal support are almost due to the subharmonic $\nu = 1$. This is due to the fact that the subharmonic can penetrate deeply in the structure of the rotor.

Both losses in PMs and support vary almost with the second power of the total current in slot.

Table 3.37: Computed rotor losses at fixed rotor speed in IPM model

Slot Current [A]	Support [W]	PMs [W]	Total [W]
	IPM		
0	0	0	0
3267	1084	603	1706
4900	2440	1357	3838
9800	9760	5430	15356
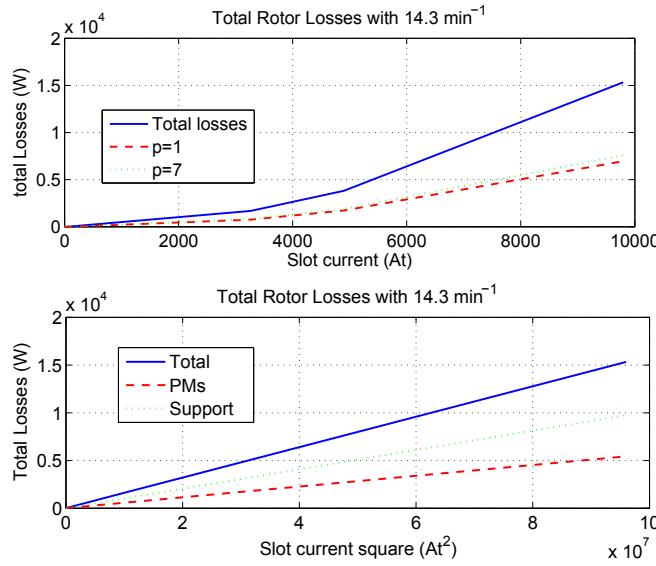
Figure 3.22: Behavior of rotor losses at fixed rotor speed in IPM model

3.4.3. Impact of the rotor speed

In this paragraph the models for IPM are considered at fixed $9800At$ total current in slot. The rotor speed varies to one third and half of the initial value which is $14.3r/min$. Fig. 3.23 shows the behavior of total rotor losses at fixed rotor speed in IPM models. The quantities due to the subharmonic ($\nu = 1$) and to the first harmonic ($\nu = 7$) are also shown. Table 3.38 presents the total computed values in each material of the rotor.

Fig. 3.23 shows the behavior of total rotor losses at fixed total Current in Slot in IPM model including the quantities due to each material of the rotor as well: the square root of the rotor speed is considered. It is worth noticing that losses in the metal support are proportional to the square root of the rotor speed and that the losses in PMs varies proportionally to the rotor speed (i.e. square with the root).

Table 3.38: Computed rotor losses at fixed total slot current in IPM model

Slot Current [A]	Support [W]	PMs [W]	Total [W]
	IPM		
0	0	0	0
4.8	4654	600	5422
7.2	5931	1352	7451
14.3	9760	5430	15356
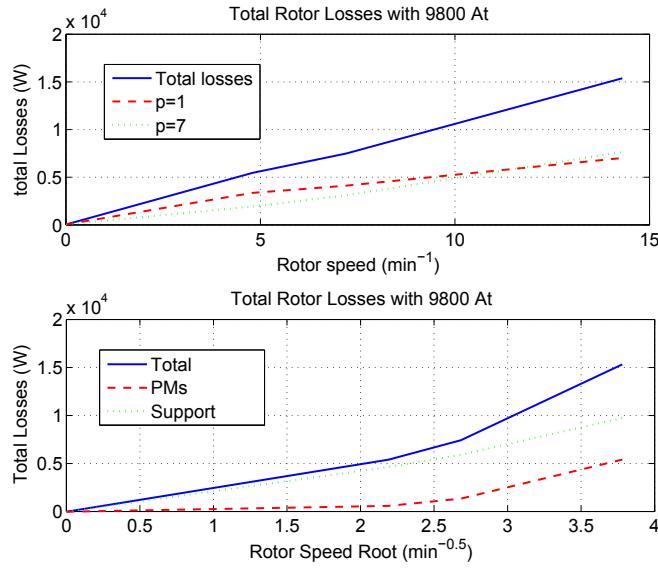
Figure 3.23: Behavior of rotor losses at fixed total current in slot in IPM model

3.5. Considerations about losses in SPM and IPM models

The behavior of losses in the rotor of the IPM and SPMA topologies have been considered both with SL and DL winding at rated set point. The total current in slot (9800 A) have been fixed at the beginning, then the rotor speed (14.3 r/min) has been fixed.

It can be noticed that:

- if the rotor speed is fixed both in the SPM structure and IPM structure losses in PMs are proportional to the second power of the total current in slot;

- if the rotor speed is fixed both in the SPM structure and IPM structure the sum of the losses in the other parts of the rotor (no PMs) is proportional to the second power of the total current in slot;

- if the current in slot is fixed in the SPM structure losses in PMs are almost proportional to the second power of the rotor speed;

- if the current in slot is fixed in the IPM structure losses in PMs are almost proportional to the rotor speed;

- if the current in slot is fixed in the SPM structure the sum of the losses in the other parts of the rotor (not PMs) are almost proportional to the rotor speed;

- if the current in slot is fixed in the IPM structure the sum of the losses in the other parts of the rotor (not PMs) are almost proportional to the square root of the rotor speed.

The total losses in SPMA structure (with massive magnetic yoke) are almost double the losses computed for the IPM structure. If the yoke of SPM structure is laminated (SPMC model), losses in yoke tend to be be constant with the rotor speed and the

absolute value of total losses is similar to the one computed for the IPM structure. Fig. 3.24 shows the behavior of total rotor losses at fixed rotor speed and at fixed current in slot in order to have a comparative summary for SPMA and IPM models.
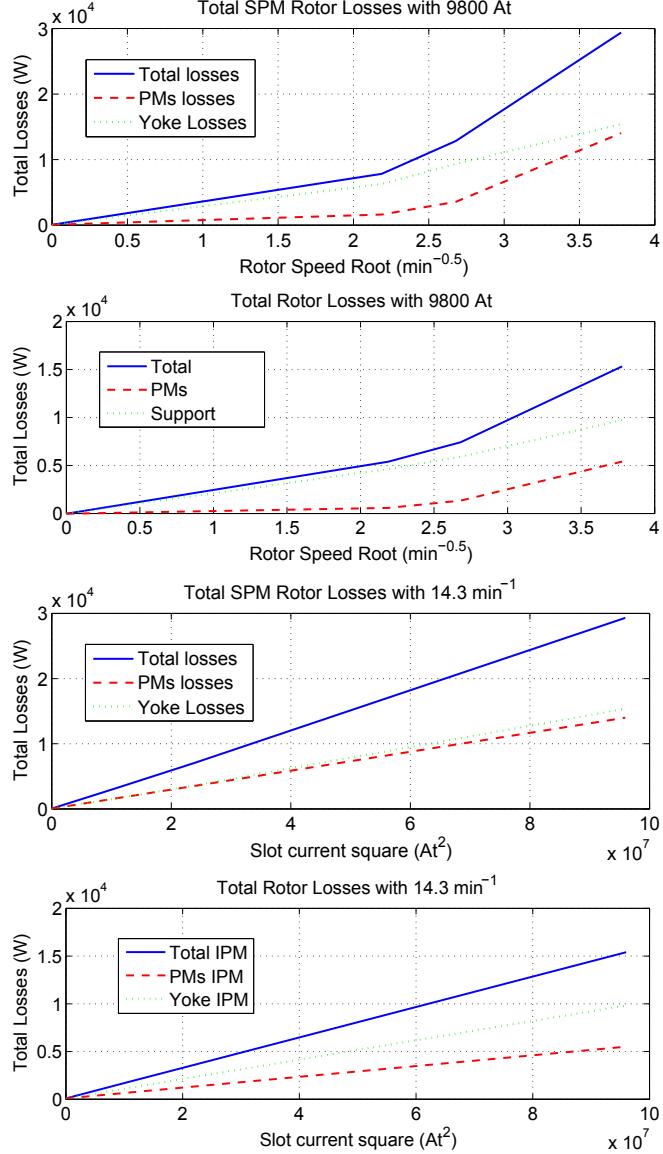
Figure 3.24: Behavior of rotor losses at fixed frequency and fixed total current in slot in SPMA and IPM models

In order to investigate the behavior of the SPM and the IPM solution if both the current in slot and the rotor speed vary,Fig. 3.25 and Fig. 3.26 are obtained considered half the current in slot and half the rotor speed. The behavior of losses remains similar. To deeper investigate the behavior of the SPM and the IPM solution if both the current in slot and the rotor speed vary,Fig. 3.27 and Fig. 3.28 are then obtained considered one third of the current in slot and one third of the rotor speed. The behavior of losses with the current in slot at fixed speed remains similar, slightly variations can be found if the total current in slot is fixed and rotor speed varies.
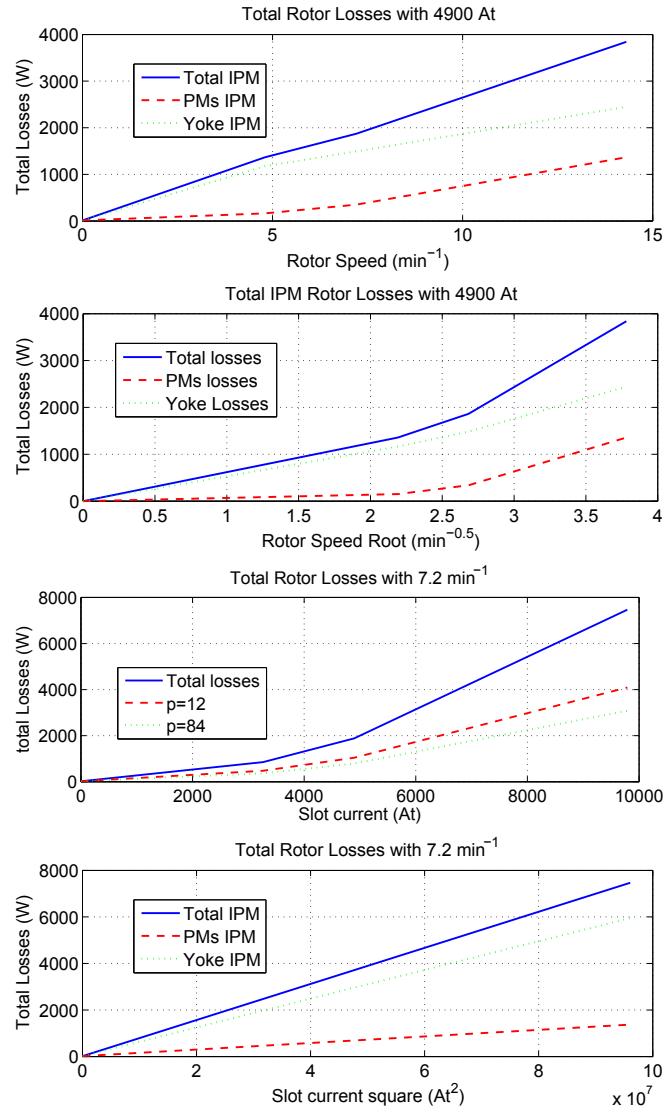
Figure 3.25: Behavior of rotor losses at fixed frequency and fixed total current in slot in IPM model
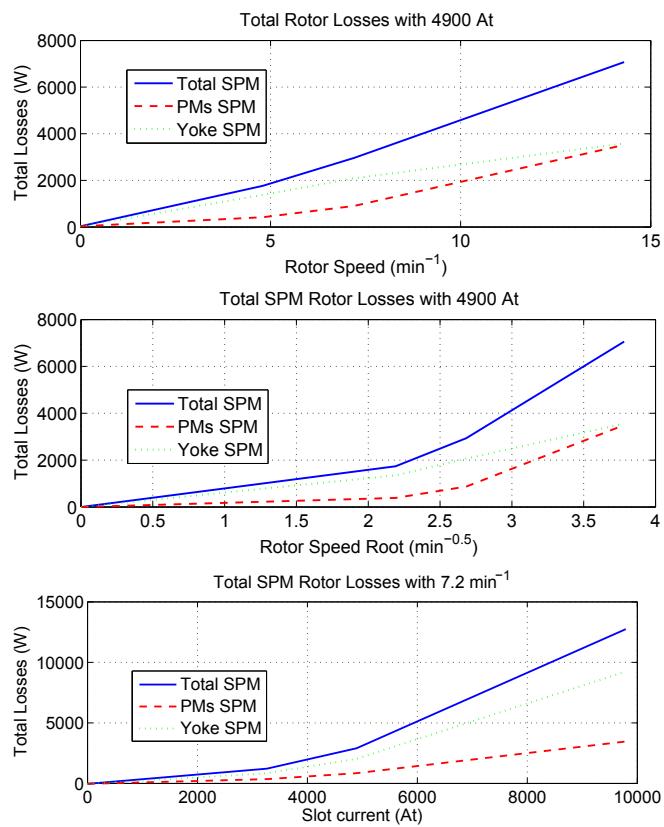
Figure 3.26: Behavior of rotor losses at fixed frequency and fixed total current in slot in SPMA model
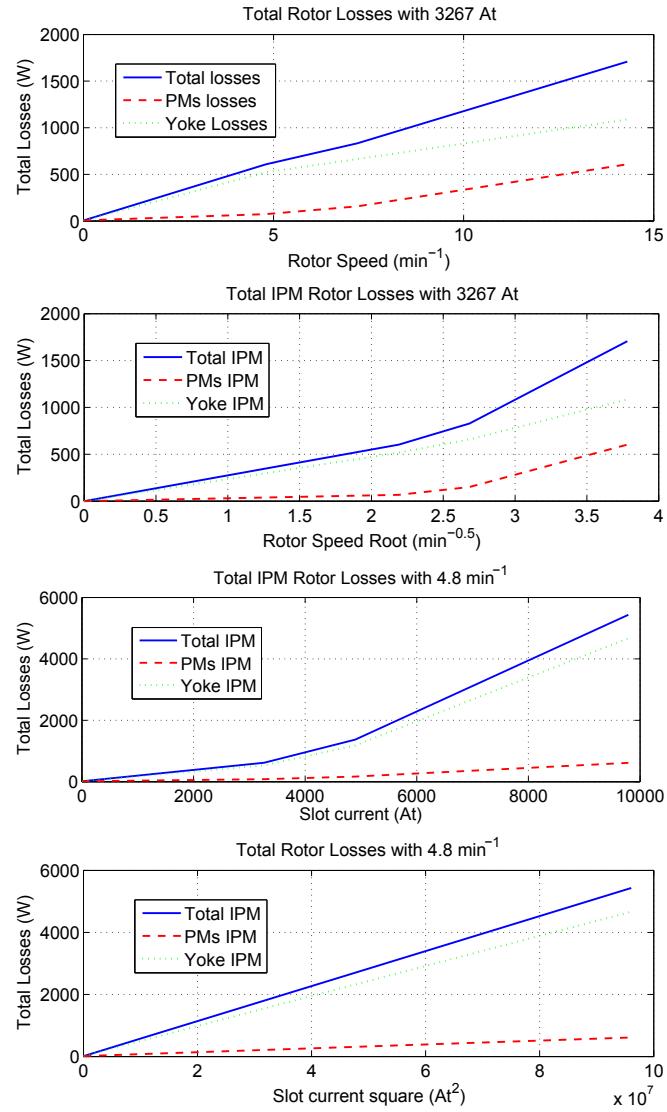
Figure 3.27: Behavior of rotor losses at fixed frequency and fixed total current in slot in IPM model
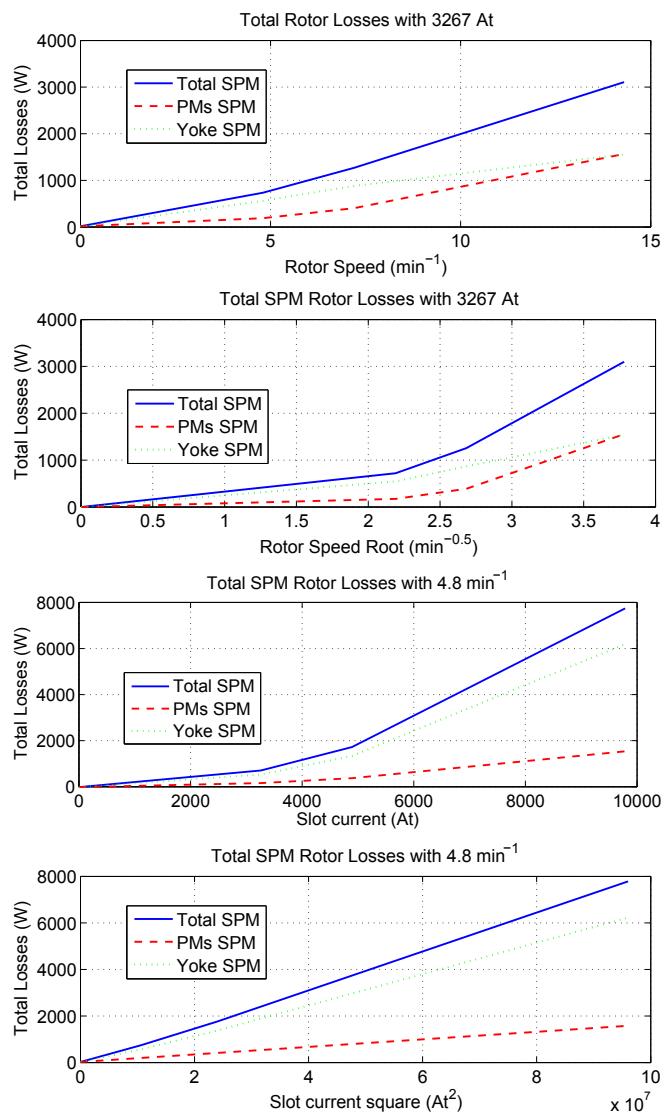
Figure 3.28: Behavior of rotor losses at fixed frequency and fixed total current in slot in SPMA model

3.6. Real cases of rotor losses on large direct drive machines

In this section practical case on existing large PM machines are considered and compared with test bench results. Considered machines are described in Chapter 2: they are both for direct drive applications and have modular structure both in the stator and in the rotor. In literature references for measures on large direct drive machines with modular structure can be found in [32, 33].

3.6.1. Method employed

A large part of B2B testing activity has been dedicated to the measure of the losses in the rotor of the machine. The rotor of the PM machine is basically composed by two parts: permanent magnets and rotor yoke. The structure of the modules employed in the rotor of the machine is the same shown in (Fig. 3.19). Losses in the metal support must be considered also. To measure the temperature of each one a thermal rise run is performed. At least two temperature sensors (pt100) have been placed both on PMs and rotor yoke, in order to guarantee the confidence of the measure. Sensor layout is in Fig. 3.29. Data are register by a logger, which rotates together with the rotor. A typical behavior of the thermal rise run at fixed stator current is shown in Fig. 3.30. The behavior is exponential as per equation (3.17). Basic equation to obtain losses is equation (3.18).
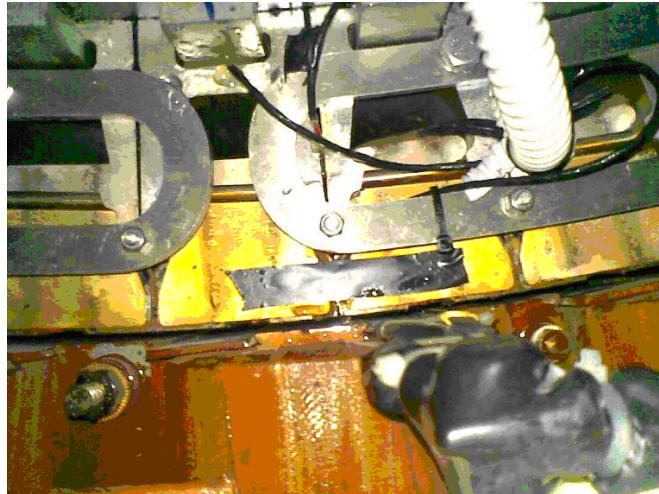
Figure 3.29: Rotor sensor layout

$$T = T_0 * (1 + e^{-\frac{t}{\tau}}) \tag{3.17}$$

$$\int_{\Delta t} Q = m \cdot c_p \cdot \Delta t \tag{3.18}$$

The calorimetric method has been employed according to the standards in [13–15]. This activity is now described and results of the test bench are compared with the so called Current Sheet Method.
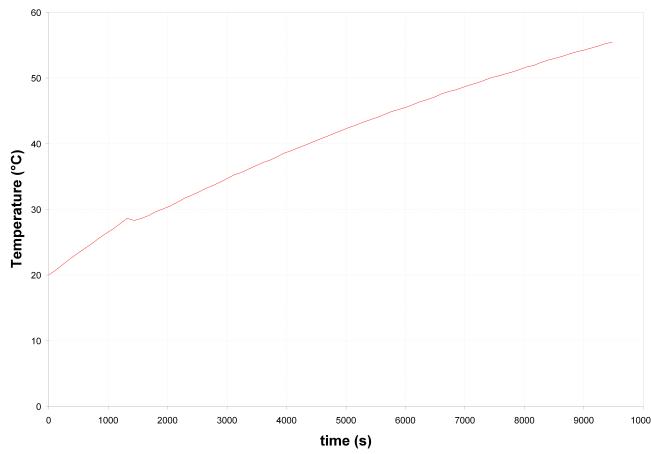
Figure 3.30: Thermal rise run: temperatures measured in the different part of the rotor

3.6.2. Wind IPM generators

To calculate load losses, a finite element (FE) model of one quarter of machine has been used. The model is represented in Fig. 3.31: the stator is substituted by current points, which inject all the harmonics of the electrical load. Several time harmonics simulation are carried out where the injected harmonics enter the rotor materials according to their geometry and to their penetration depth and cause losses in massive materials.For losses in rotor lamination, stator lamination and copper refers to tables in Generator Analytic Model section.
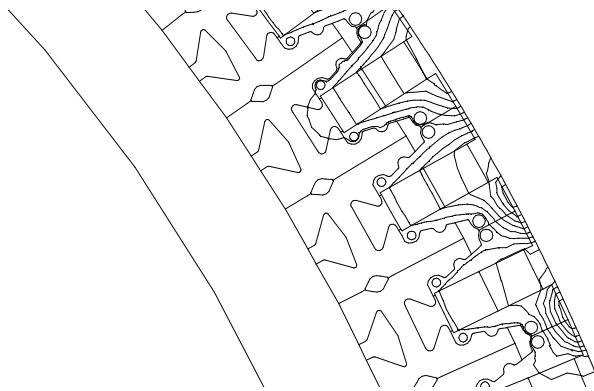
Figure 3.31: FE model used for the computation of the load losses in rotor massive materials, details of current points through the airgap

Assumptions of the model:

- For geometry refers to Generator Analytic Model Section;

- Rated stator current is 968x2 A;

- Generator speed is 18 r/min;

- The total induced current on each PM is assumed to be zero;

- The Support profiles are electrically connected (simulation A);

- The Support profiles are electrically not connected (simulation B);

- The Support profiles are partially electrically connected, with two group of four connect profiles and one group of three connected profiles in a quarter of machine (simulation C);

- Losses are then calculated at no load with disconnected rotor profiles (slotting);

- Iron is assumed to be laminated;

- Total length of the profile is set to $\sim 1000mm$;

- Electric conductivity of PMs is set to $0.66MS/m$;

- Electric conductivity of Aluminium is set to $25MS/m$;

- Electric conductivity of Laminated iron is set to $10.44MS/m$;

- Electric conductivity of rotor yoke iron is set to $1MS/m$;

- Magnetic characteristic of rotor yoke corresponds to 1018 Steel material;

- Frequency of the problem considers the harmonics of the MMF force calculated for a single layer 96 slots 104 poles electrical machine with concentrated windings.

Table 3.39 reassumes the results obtained from the load losses rotor simulation A (Support profiles are electrically connected to each other): Table 3.40 reassumes the

Table 3.39: Computed load rotor losses A (connected Support profiles)

Material	Losses of 104 profiles [%]
PMs	24.11
Support	43.47
Laminatation (analytical calculation)	27.6
Yoke	5.13
TOTAL	100

results obtained from the load losses rotor simulation B (Support profiles are electrically insulated to each other): Table 3.41 reassumes the results obtained from the load losses rotor simulation C (Support profiles are electrically connected in 4-3-4 group in one quarter of machine): Iron losses in the stator iron are computed as about $13kW$ (40–50%) in simulation A,B and C. Connection C is half way between A and B.

Table 3.40: Computed load rotor losses B (insulated Support profiles)

Material	Losses of 104 profiles [%]
PMs	21.4
Support	149
Laminata-tion (analytical calculation)	27.6
Yoke	33.5
TOTAL	231

Table 3.41: Computed load rotor losses C (4-3-4 Support profiles group in one quarter of machine)

Material	Losses of 104 profiles [%]
PMs	24.3
Support	93
Lamination (analytical calculation)	27.6
Yoke	8.3
TOTAL	153

3.6.3. Comparison between computed losses and measured losses by LTW

According to Table 3.42 the load losses calculated are listed.

Support profiles are first considered to be electrically and then half way connected, rotor yoke is magnetic type. The sum of the induced eddy current losses with the half–way connection is quite closer to the measured value.

The correspondence between the FE models developed with the current sheet methods and the test bench experience suggests that these FE models allows to have a satisfying computation of the rotor losses in large direct drive PMs machines. They can be used to predict the behavior of rotor losses at different rotor speed and total current in slot.

The rotor losses due to slotting at no-load are now computed considering electrically insulated support profiles. According to Table 3.43 the comparison between the computed no load losses and the measured ones in PMs and support profiles: the sum

Table 3.42: Comparison between computed and measured losses at load

Material	Losses half–way [%]	Losses connected [%]	Measured by LTW [%]
PMs	24.3	24.11	25.2
Support	93	43.47	36.8
Laminata- tion (analytical calculation)	27.6	27.6	32.8
Yoke	8.3	5.13	43
TOTAL	153	100	138
Yoke+Support	101	48	80
Yoke+Sup+PM	125	73	105

of these losses has been calculated as 10%, while measure establish 8.4%. If Table 3.40 is considered, the sum of losses in PMs and support at load is computed to be 170%: the slotting addendum is then much lower than the MMF one in the total amount of losses.

Another practical example will be shown on the smaller direct drive motor for ropeway traction.

Table 3.43: Comparison between computed and measured losses at no load

Material	Losses not connected [%]	Measured by LTW [%]
PMs	4.5	4.4
Support	5.5	4.0
Supp+PMs	10.0	8.4

3.6.4. Ropeways IPM motors

The procedure described is here applied to a real prototype of large size PM motor for ropeways.The winding is fractional slot type. The machine has been built by Leitner A.G. and was tested by Leitwind A.G. test bench in Telfs (Austria). This motor is now working in a Austrian site. The direct drive concept developed by Leitner Technologies Group is presented in [16]. The losses in rotor PMs and yoke has been computed with finite elements model. They have been used to build a thermal map of the rotor: the temperatures in PMs and yoke have been calculated and compared with the results of the test bench. Fig. 3.32 shows a picture of the motor under test. The main characteristics are presented in Table 3.44: it is worth noticing that the diameter of the IPM motor is similar to the one of the machine C' which will be studied in Chapter 4 and that the machine periodicity t=8 is the same. Fig. 3.33 shows the fractional slot winding of the motor under test. When the machine operates under nominal load

Table 3.44: Characteristics of the motor under test

Characteristic	Value
Diameter (mm)	2160
Length (mm)	736
Slots	96
Poles	80
Rated Speed (r/min)	19.5
Periodicity	8

Figure 3.32: Ropeways motor under test.

the computed losses in rotor due to the subharmonic are almost 13 kW. In Table 3.45 rotor losses have been calculated for each harmonic and they have been expressed in relation to the losses due to the subharmonic. The frequency f_r seen by the rotor is presented for each harmonic also. Once again the losses induced in rotor by harmonics are negligible in respect to the losses induced by the subharmonic. Rotor losses due to the subharmonic have been calculated again, considering that the ropeways motor is operating under overload condition (+40% in respect to the nominal current). They
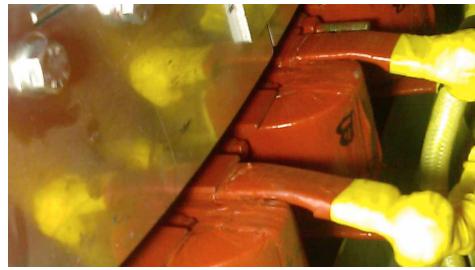
Figure 3.33: Fractional slot winding of the ropeways motor.

Table 3.45: Amount of rotor losses for IPM motor due to each harmonic

p	f_r	Losses [%]
8	15.6	100%
40	0	0%
56	31.2	1%
88	15.6	0%
104	46.8	0%
136	31.2	0%
152	62.4	0.1%

results to be 28.5 kW, more than twice the load condition ones. The rotor losses calculated under load condition and overload condition have then been used to build a simplify thermal finite element model. Table 3.46 presents the over-temperatures calculated with finite element model in rotor PMs and rotor yoke of the ropeways machine. Both the case of the machine under load condition and overload condition are listed. The increasing of temperature obtained under overload operation in respect to load operation is also shown. Table 3.47 presents the over-temperatures measured by the sensors applied on the rotor PMs and rotor yoke of the IPM machine. It is worth noticing that the increasing of the over-temperature from load operation to overload operation, measured by temperature sensors of the test bench, quite agrees with the ones predicted by the thermal finite element model.

Table 3.46: Over-temperatures in the rotor of IPM motor from finite element model

Material	Under load [℃]	Under overload [℃]
PMs	64	109
Rotor Yoke	64	109

Table 3.47: Over-temperatures in the rotor of IPM motor from test bench

Material	Under load [°C]	Under overload [°C]
PMs	67	113
Rotor Yoke	70	115

Chapter 4

A Scaling Law for Rotor Losses

The aim of this chapter is to study the rotor losses phenomenon going through different machine sizes rotational speeds and electrical loadings. The computation of rotor losses is a crucial aspect in Permanent Magnet (PM) machine design. In particular, with the adoption of fractional–slot windings (which causes an increase of the space harmonics content of magneto motive force), the rotor losses assume a dominant role in the machine performance, their prediction is crucial.

4.1. Introduction

PERMANENT Magnets (PMs) are more and more employed in rotating machines to replace the electromagnetic excitation. They allow to build a more compact brushless rotor, also characterized by several poles, which results to be suitable for low–speed direct drive applications.

The growing requirements for higher and higher torque density and the improving technology in PM manufacturing led to the employment of rare earth magnets like NdFeB and SmCo in rotor, instead of Ferrite magnets. In addition, the fractional–slot windings are more and more replacing the integral–slot windings (with full pitch stator windings), so as to reduce stator copper. This type of machine exhibits many advantages such as short end–windings, high slot fill factor, high efficiency and power density together with good flux–weakening and fault-tolerance capabilities [34, 35].

However, the space harmonics of the magneto motive force (MMF) due to such a fractional–slot windings lead to considerable rotor losses. The computation of these losses according to standard procedures (e.g. Steinmetz equation) is not satisfactory. The MMF harmonics move asynchronously with respect to the rotor, inducing currents in any conductive rotor parts, e.g. the metallic iron yoke which supports the magnetic poles and the rare earth PMs themselves. The MMF space harmonic amplitude and frequency depend on the particular combination of number of slots and poles. A detailed description of the MMF harmonic computation can be found in [11].

In the prediction of electrical machines performance, the working temperature are crucial parameters. They are related to the efficiency of the cooling systems and to

the losses in stator and rotor. The stator losses include Joule losses of the copper winding and iron losses in lamination computed via Steinmetz's equation. They can be measured according to standard procedures. The rotor losses are extremely difficult to be measured, despite of their high value in PM fractional slot winding machine. Therefore it is very important to get an accurate prediction.

Various papers cover the topic of the rotor losses computation [36, 37] comparing various fractional–slot machines with respect to the rotor losses [30, 38]. Nevertheless, the impact of the machine size on the rotor losses has not dealt with in the past works. In order to fill this gap, this paper investigates how the rotor losses are influenced by the main dimensions of the PM machine.

At first, the study considers a 125–mm inner diameter PM machine. Then, all geometric lengths are increased through a linear scaling law, for given number of slots and poles. The rotor losses are compared and the relation between rotor losses and machine size is highlighted. Then, two other different machine geometries are compared, rearranging the number of slots and poles according to the stator inner diameters, but keeping the same ratio between slots and poles.

4.2. Analytical Relationship

At first, the relationship between the rotor losses due to induced currents in the rotor and the size of the electrical PM machine is analyzed theoretically.

The machine size is modified keeping the same design, but increasing its geometrical dimensions, so that each length increases proportionally to the quantity l, each surface increases proportionally to l^2, and each volume to l^3. Therefore, for a given stator current density, the current in the stator slots increases as l^2, and thus the electric loading (i.e., the linear current density computed along the stator inner circumference) increases proportionally to l.

Hence, applying the Ampere's law, the flux density B in the air gap results to be proportionally to l, and the magnetic vector potential A, whose curl is B, is proportionally to l^2. Then, the current density induced in the rotor is estimated as:

$$J_r = -\sigma \frac{\partial A}{\partial t} \tag{4.1}$$

where σ is the material conductivity and t is the time. Assuming that the operating frequency remains the same during the scaling process, it results that the induced current density is proportional to l^2.

As a consequence, the losses in the rotor volume due to such induced currents are given by:

$$P_{rl} = \int \frac{J_r^2}{\sigma} \, dVol \tag{4.2}$$

Since the volume increases as l^3 and J_r as l^2, then the rotor losses result to be proportionally to l^7, that is:

$$P_{rl} \propto l^7 \tag{4.3}$$

Although these equations above do not consider skin effects or iron saturation, they highlight how the rotor losses tend to increase with the machine size. If the rotor losses

phenomenon could be neglected in small size PM machine, it has to be mandatorily taken into account in large size PM machines.

4.3. Finite element based analysis of a 12–slot 10–pole PM machine with various sizes

This section aims to verify the analytical relationships described above, by means of finite element analysis.

Starting from a 125–mm inner diameter SPM machine, the geometric lengths are increased simply through the scaling law, keeping constant the number of slots and poles. Fig. 4.1 shows a sketch of the geometry. The first three rows of Table 4.1 summarized the configurations that have been analyzed, that is, machines labeled as A, B and C.
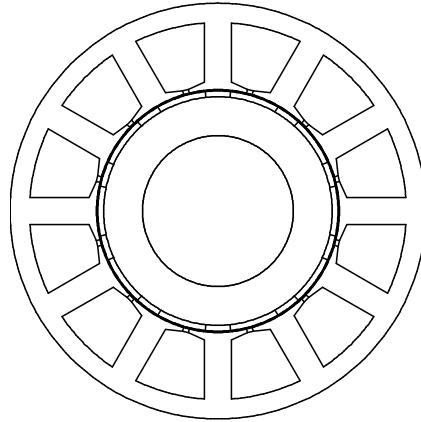
Figure 4.1: Machine A with 12 slots and 10 poles.

Table 4.1: Airgap diameter dimension.

Machine	Diameter D (mm)	Length L (mm)	gap g (mm)	Slots Q	poles $2p$
A	125	100	1	12	10
B	500	400	4	12	10
C	2000	800	8	12	10
A=A'	125	100	1	12	10
B'	500	400	1	48	40
C'	2000	800	2	96	80

4.3.1. Analysis procedure

The MMF space harmonics are computed, considering both their amplitude and speed. Then, the corresponding electric loading harmonics $\hat{K}_{s,\nu}$ are computed according to machine geometry. The stator is removed and replaced by an equivalent current sheet placed along the inner diameter as shown in Fig. 4.2. For each harmonic, the electrical loading $K_{s,\nu}(\theta)$ is applied as:

$$K_{s,\nu}(\theta) = \hat{K}_{s,\nu} \cdot \sin(\nu\theta + \omega_\nu t) \tag{4.4}$$

where ν is the harmonic order, and ω_ν/ν is the speed of such harmonic with respect to the rotor. The space harmonics induce losses in any rotor conductive part, i.e., in PMs and back iron in PM machine. The material properties used in the model (both for linear and saturated back iron yoke) are listed in Table 4.2. From Fig. 4.2, it is worth noticing that back iron has been split in two parts, so as to decrease the size of the mesh elements according to the skin depth of the iron.
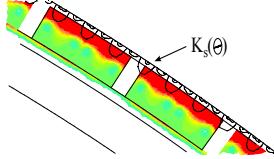
Figure 4.2: The stator is replaced by an equivalent current sheet.

Each MMF harmonic is imposed independently and the corresponding rotor losses are computed. Then, the total rotor losses P_{rl} result as the sum of the rotor losses computed for each harmonic order ν, that is:

$$P_{rl} = \sum_\nu P_{rl,\nu} \tag{4.5}$$

Table 4.2: Material properties used in the model.

Material	PMs NdFeB	iron solid linear	iron lamin. linear	iron lamin. non–linear
σ (MS/m)	0.67	10	0	0
μ_r $(-)$	1.05	50	50	$\mu_r(B)$

According to the 12–slot 10–pole PM machine, with a single–layer winding, Fig. 4.3 shows the amplitudes of the MMF space harmonics, as percentage of the main harmonic. The presence of a subharmonic of order $\nu = 1$ is evident. Fig. 4.4 shows their frequency, in the rotor frequency frame.

As an example of computation, Fig. 4.5 shows the flux lines in the rotor of the 12–slot 10–pole PM machine due to the MMF harmonics, (i.e. of order $\nu = 1$), that is a two–pole space harmonic.
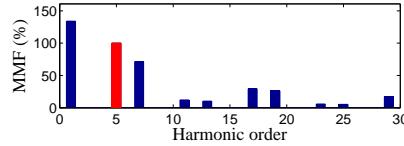
Figure 4.3: Stator current MMF harmonic amplitudes versus harmonic order, according to a 12–slot 10–poles single–layer PM machine.
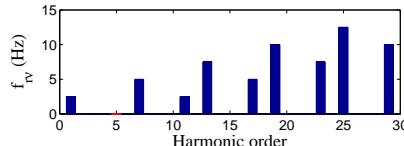
Figure 4.4: Rotor frequency of the stator current MMF harmonics.
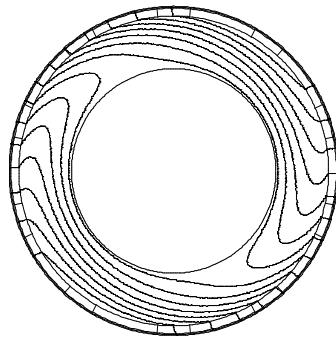
Figure 4.5: Field lines due to the various harmonics.

4.3.2. Results with laminated rotor iron

At first, the rotor back iron is considered to be laminated, so that there are no currents induced in the iron but only in the PMs. In the FE analysis the electrical conductivity of the rotor back iron is set $\sigma = 0$ due to lamination.

The rotor losses are computed according to a rotor speed of 25 r/min. The amplitude and frequency of each MMF space harmonic is computed, refering to the 12–slot 10–pole configuration under study. Then, the corresponding electric loading harmonics are imposed along the stator inner circumference.

Such a computation is carried out for the different sizes of the PM machines, i.e., machine A, B, and C of Table 4.1, computing the relationship between the resulting rotor losses $P_{rl,\nu}$ and the geometric dimension l. The aim is to verify the exponent 7 of l in such a relationship, that is $P_{rl,\nu} \propto l^7$ as in 4.3.

Fig. 4.6 shows the value of the exponent that results, from comparing the rotor losses (losses in the PMs only) of the three PM machines, versus the harmonic order ν. For all the harmonic orders, the rotor losses result to be proportional to the seventh power of the linear geometrical dimension. This is in agreement with the analytical prediction presented above.
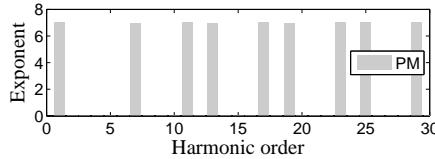
Figure 4.6: Exponent of l in the relationship between rotor losses $P_{rl,\nu}$ and linear dimension l, versus harmonic order ν. Rotor back iron is laminated. Rotor speed is 25 r/min.

4.3.3. Results with solid rotor iron

If the iron is not laminated, eddy currents flow in the rotor yoke as well. The higher impact is due to the MMF sub–harmonics, that is, the harmonics that have a wavelength higher than the pole pitch [30].

From the comparison of the three machines, with different size, Fig. 4.7 shows the value of the exponent of l that is used in the relationship between the rotor losses and the linear dimension l, versus the harmonic order ν. The rotor losses are now in both PMs and iron yoke.

In this case, for low harmonic order, the exponent results lower than the analytical prediction, that is, the increase of losses with the machine size results smaller than the prediction given in 4.3. This is caused by the shielding reaction due to the eddy currents mainly in the back iron. As well known, they create a magnetic field that opposes to the stator field, reducing the amount of rotor losses.

Fig. 4.8 aims to illustrate the reaction due to the rotor currents especially in large size machine. Both simulations refer to the subharmonic of order $\nu = 1$. Fig. 4.8 (a), refers to the small size machine: the flux lines are almost orthogonal to the air gap. On the contrary, Fig. 4.8 (b), refers to the large size machine: the flux lines are distorted by the eddy currents flowing in the rotor, mainly in the iron part.
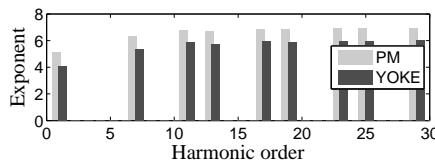
Figure 4.7: Exponent of l in the relationship between rotor losses $P_{rl,\nu}$ and linear dimension l, versus harmonic order ν. Rotor back iron is solid. Rotor speed is 25 r/min.

For higher harmonic orders, it is observed that in rotor yoke the exponent is close to 6 rather than 7, as analytically expected, 4.3. This is due to the skin depth δ of the solid iron, given by:

$$\delta = \sqrt{\frac{1}{\pi f \sigma \mu}} \tag{4.6}$$

Its value is constant for all the PM machines under analysis, the material and the rotor speed remaining to be the same. Therefore, δ does not depend on the machine dimension l, so that the volume where the rotor losses are located results to be proportional to l^2. Hence, such rotor losses result to be proportional to l^6.
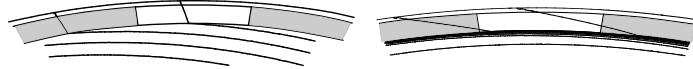
Figure 4.8: Flux lines for small and large machine.

As far as the rotor losses in the PMs are concerned, they all result to be almost proportional to l^7, agreeing with the analytical prediction, but the subharmonic of order $\nu = 1$. The increase of rotor losses due to such subharmonic is almost proportional to l^5.

4.3.4. Impact of the frequency

In order to investigate the effect of frequency on the relationship between rotor losses and machine size, the rotor speed is increased up to 250 r/min. Fig. 4.9 shows the exponent of l, versus the harmonic order ν, according to a solid rotor back iron.

In this case, the shielding effect is more evident for all the harmonic orders. The exponent 7 and 6, for PMs and back iron respectively, are reached for high harmonic order. Once again the skin depth limits the increase of the rotor losses with the machine size.
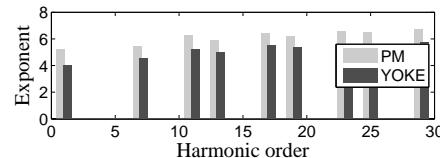
Figure 4.9: Exponent of l in the relationship between rotor losses $P_{rl,\nu}$ and linear dimension l, versus harmonic order ν. Rotor back iron is solid. Rotor speed is 250 r/min.

4.3.5. Saturation in iron yoke

In the analysis above the iron permeability has been fixed, so that all the materials exhibit a linear $B - -H$ curve, and the superimposition of the effects is applied to compute the rotor losses as described by (4.5). However, it was observed that the subharmonic of order $\nu = 1$, which is characterized by the higher wavelength, yields a high flux density in the iron, especially if the iron permeability is fixed to a high value (e.g., $\mu_r = 5000$). Since the computation does not consider the saturation, it is affected by an error, when the constant iron permeability fixed in the simulation is very different from the effective value. On the other hand, if saturation is considered the superimposition of the effects can not be applied, and only a step–to–step analysis

is effective but the impact of each harmonic on the rotor losses can not taken into account.

For the sake of weighting the effect of the saturation, hereafter, only the subharmonic of order $\nu = 1$ is considered. A non–linear magnetic material in back iron is assumed, setting a permeability as a function of the flux density, i.e., $\mu_r(B)$. Hence, the field distribution changes according to the iron saturation.

Fig. 4.10 shows two plots of loss density due to subharmonic for the linear and non–linear iron yoke. The speed is fixed to 25 r/min. The effect of saturation is to reduce the effective permeability of the iron, so that the flux lines enter deeper in the rotor yoke. In other words, the skin depth δ increases.

Fig. 4.11 shows the behavior of the flux density amplitude from the external towards the inner diameter of the yoke. When linear BH–curve is considered (and a high permeability $\mu_r = 5000$ is fixed), a high and improbable flux density is achieved, Fig. 4.11(a). The flux lines are limited in a small portion of the yoke. The effect of the saturation is to decrease the flux density amplitude (Fig. 4.11(b)) and to increase the portion of the yoke carrying the flux lines, as the shaded area in Fig. 4.10(b). As a consequence, it results definitely important to set a proper permeability in the rotor loss computation based on the linear BH characteristic.
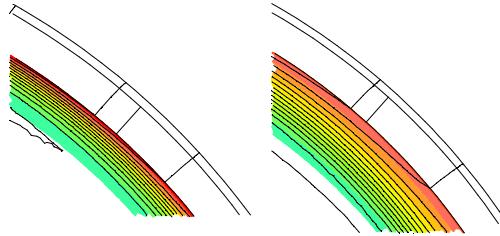
Figure 4.10: Plots of loss density comparing machines with linear iron ($\mu_r = 5000$) and non–linear iron ($\mu_r(B)$).
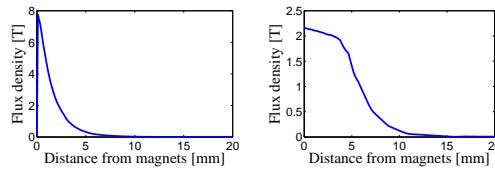
Figure 4.11: Flux density in the iron yoke: comparison between linear and non linea B–H curve.

Table 4.3 reports different results for linear iron (two constant linear permeabilities are considered: $\mu_r = 5000$ and $\mu_r = 150$) and non–linear iron (the permeability is a function of B). The losses are computed according to various amplitude of the electric loading. The highest discrepancy is found when the electric loading is high, yielding to a higher flux density and a higher iron saturation.

Table 4.3: Rotor losses with saturation for the one pole pair subharmonic

Electric Loading (A/m)	Iron relative permeability	PM loss (W)	iron loss (W)
78 000	$\mu_r = 5000$	0.5	186.4
78 000	$\mu_r = 150$	0.2	376.0
78 000	$\mu_r(B)$	0.2	450.6
30 000	$\mu_r = 5000$	0.1	28.3
30 000	$\mu_r = 150$	0.03	57.0
30 000	$\mu_r(B)$	0.1	58.9
3 000	$\mu_r = 5000$	0	0.3
3 000	$\mu_r = 150$	0	0.6
3 000	$\mu_r(B)$	0	0.3

4.4. Finite element analysis of PM machines, increasing the number of slots and poles

Indeed, when the size of the machine increases, the number of slots and poles does not remain the same (as assumed in the previous analysis), but it is rearranged correspondingly. Typically, when the diameter increases, the number of slots increases as well. Then, it is reasonable that a large size machine rotates slower, and thus the number of poles increases with the machine size.

The following analysis refers to the machines A', B' and C' whose main dimensions are reported in Table 4.1. Machine labeled A' is characterized by a unity periodicity, that is $t_p = 1$, [11]. Machine B' is obtained from machine A' multiplying the machine periodicity by four, that is, by the same ratio between the inner diameters (i.e. 500/125). In the same way, the number of slots and poles is increased by four. However, the geometry of the stator teeth and slots is kept the same, and, similarly the air gap and PM thicknesses are kept the same. The pole pitch of the machines A' and B' results to be the same, so that the flux density remains constant. It is expected that the rotor losses increase proportionally to the machine periodicity (i.e. four in the example under study).

Table 4.4 reports the rotor losses in the machines A' and B', considering the same working frequency. The results confirm the expected behavior, with an increase of the rotor losses by almost four times from machine A' to the machine B'.

The PM machine labeled C' has been designed to have the same flux density of the two previous configurations. However, while the ratio between the diameters of the machine B' and C' is four, the number of slots and poles is only twofold, i.e., the machine periodicity is multiplied by two. The dimensions of the stator teeth and slots are doubled, as well as the air gap and PMs thickness.

With these choices, the periodicity of the PM machine C' is increased by $t_p = 8$ times with respect the PM machine A', while the scaling factor is $l = 2$. Therefore, it is expected that the increase of rotor losses is

$t_p \cdot l^7 = 8 \cdot 2^7 = 1024$ times in the PMs, and
$t_p \cdot l^6 = 8 \cdot 2^6 = 512$ times in the iron yoke,
with respect to PM machine labeled A'.

Table 4.4: Comparison of rotor losses in machine A' and B'

Machine	PM losses (W)	Back iron losses (W)
A'	1.2	191.7
B'	5.3	815.6

The rotor losses in these PM machines have been simulated. For the sake of verification, Fig.4.12 shows the exponent of l, versus harmonic order ν and the machine labeled A' is compared with 1/8th of the machine labeled C'. This choice lets to focus the comparison on the geometrical scaling, without considering the effect of the machine periodicity.

Once again the results confirm the prediction: the rotor losses increase proportionally to l^7 and l^6, in the PMs and in the iron yoke, respectively. If the whole structure of machine C' is considered, they increase proportionally to the increase of the machine periodicity as well.
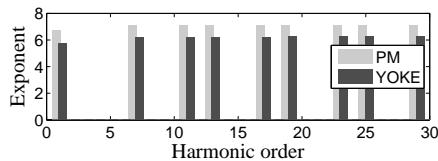
Figure 4.12: Exponent of l in the relationship between rotor losses $P_{rl,\nu}$ and linear dimension l, versus harmonic order ν. One eighth machine C' (96 slots and 80 poles) and A' (12 slots and 10 poles) are used for this computation.

4.4.1. Air gap thickness impact

The air gap thickness has a high impact in the rotor losses determination. The increase of the air gap limits the effect of the MMF harmonics, since the corresponding flux density is reduced. This reduces the eddy currents and the rotor losses consequently.

4.4.2. Losses for given electrical loading

In the comparison above, the surface current density in the stator slots is kept constant. Alternatively the comparison can be carried out fixing a constant linear current density, that is, the stator electrical loading K_s. The slot current density decreases proportionally to l. Therefore, applying the procedure described in section 4.2, the rotor losses result to be proportional to l^5 and l^4, in the PMs and in the iron yoke, respectively. This is confirmed by the behavior of the exponent of l in Fig. 4.13 achieved by finite element based analysis.
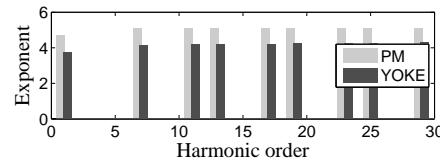
Figure 4.13: Exponent of l in the relationship between rotor losses $P_{rl,\nu}$ and linear dimension l, versus harmonic order ν. Computation carried out by fixing a constant electric loading.

4.5. Impact of rotor losses in machine temperature

This section aims to estimate the increasing of temperature rise due to rotor losses. The machine A' and C' of Table 4.1 are considered in two different thermal conditions: without and with the rotor losses.
Fig. 4.14 shows a portion of machine A' used for the thermal simulation. Regions are identified by the letters in brackets, each one is characterized with a thermal conductivity λ (in W/mK) and a specific losses (in W/m^2K).
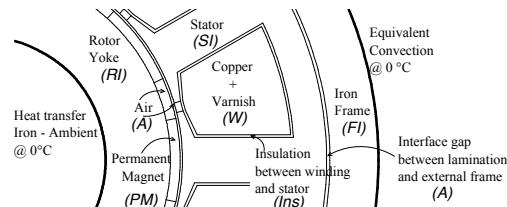
Figure 4.14: Finite element thermal model

The thermal conductivity of the materials are reported in Table 4.5. The specific losses for the regions W, PM and RI are computed fixing the stator electrical loading K_s (see section 4.4.2): with such a hypothesis, the current density decreases with the machine size, and in the machine C' it is half than in the machine A'. It results that the specific losses for region W in machine A' are four times those in machine C'.

It results that the copper specific losses p_{Cu} in machine A' are four times those in machine C'. The rotor losses in regions PM and RI are almost proportional to l^5 and l^4, respectively, that is, the specific losses results to be almost proportional to l^2 and l, respectively. Referring to the machines A' and C', the scaling factor is $l = 2$, therefore

the specific losses of A' in PM and RI are almost four and twice times those of C', respectively.

Heat transfer coefficients α_s and α_r with reference temperature equal to zero has been fixed along the external surface of the stator and rotor. For the stator the combined natural convection and radiation-heat-transfer coefficient lies in the range $\alpha_s = 12$ to $14\ W/m^2K$. For the rotor only a radiation heat transfer is through the shaft assuming a value $\alpha_r = 6\ W/m^2K$ [39].

Table 4.5: Thermal conductivity of the using materials

REGION	MATERIAL	SYMBOL	VALUE (W/mK)
Ins	Stator insulation	λ_{iso}	0.15
W	Copper+Varnish	λ_{Win}	0.75
FI / SI / RI	Iron	λ_{Fe}	45
A	Air	λ_{air}	0.026
PM	Magnet	λ_{mag}	9

Fig. 4.15 shows the temperature map for the machine A' neglecting and considering rotor losses: colors from light blue to dark red show the temperature rise in the machine.
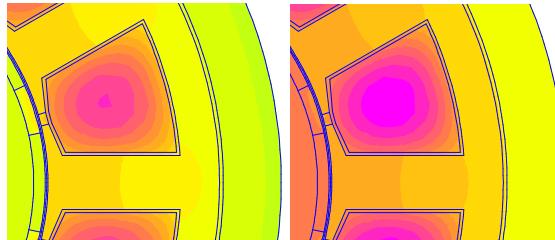
Figure 4.15: Effect of the rotor losses in the machine temperature

Table 4.6: Temperature rises due to the rotor losses

	Machine	Winding	PMs
Without Rotor Losses	A'	136 K	101 K
With Rotor Losses	A'	142 K	123 K
		(+4.4%)	(+21.8%)
Without Rotor Losses	C'	110 K	69 K
With Rotor Losses	C'	138 K	168 K
		(+25.5%)	(+143.5%)

The resulting temperature rises in PMs and Copper are listed in Table 5.25: the rotor losses influence the thermal behavior of the two machines, in particular of machine C'. There is an evident increasing of the temperature both in PMs and in the winding.

It is worth noticing that the rotor losses has not to be neglected during the design process, in order to avoid an underestimation of the operating temperatures. In the actual operating conditions, an overheating might occurs, causing a fault in the machine. An estimation of the rotor overheating caused by the rotor losses is possible by detecting the temperature rise of the winding. A proper threshold has to be included in the monitoring system of the machine in order to avoid that the predicted rotor temperature rise reaches unacceptable values [40].

Furthermore, the rotor losses cause an increase of the temperature in PMs. Both the residual flux density and the magnetic field of the knee of the B-H curve are reduced, as reported in Fig. 5.6. The reduction of the residual flux density causes a decrease
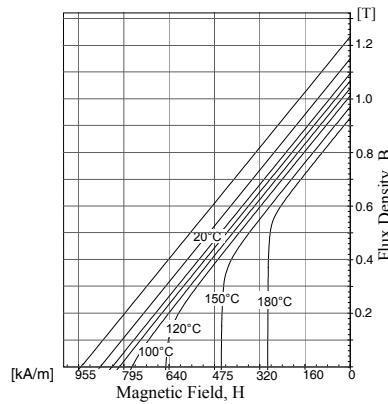
Figure 4.16: Variation of B-H curve for a Neodymium-Iron-Boron PMs with the temperature

of back electromotive force (EMF) and of the motor performance. The reduction of the magnetic field increases the risk of an irreversible demagnetization of the PMs. Therefore, a further strategy to monitor the temperature rise in the rotor is to measure the decrease of the back EMF. This can be carried out adopting any diagnosis technique, e.g. based on a model of the motor, a reconstruction of the zero sequence voltage [41] or the stator current harmonic spectrum [42–44].

4.6. Final considerations

The rotor losses cause the raise of the working temperature. This paper highlights that such losses tend to increase dramatically with the PM machine size. If a simple linear scaling law is applied, so that each geometrical length is increased by a factor l, the increase of the rotor losses results equal to l^7 times.

In order to limit such rotor losses in large size machine, it is mandatory that the machine periodicity increases. Further strategies are to decrease the surface current density, and to increase the air gap thickness when the machine size increases.

Chapter 5

Selection of the number of slots and poles

This chapter describes a methodology to choose a proper stator slots and rotor poles number in large direct drive electrical machines. Main aspects are the winding factor, which is proportional to the torque, and losses in the massive materials of the rotor. To have a synthetic instrument to evaluate losses due to different windings, the Index of Rotor losses is applied in this study. Some basic windings configuration are evaluated and compared with the aim to choose the proper one to design the new LW30A large direct drive generator for LTW101 wind turbine. The final optimization of the magnetic circuit of the machine is then overviewed.

5.1. Basic model for rotor losses

IN Chapter 3 an analytical straight–lined model to calculate losses in massive material has been introduced. It has been proved that the model is suitable to predict the losses of a SPM machine with a continuous magnet ring: Table 5.1 shows the comparison between the FEM model of Fig. 5.1 and analytical computation basing on a 24 slots and 26 poles double–layer (DL) winding. This number of slots (Q) against number of poles (2p) ratio corresponds to 12–13 configuration. The agreement between the finite element simulations and the analytical model is good.

The analytical model has been developed within the Electric Drives Laboratory of the University of Padova, as described in literature [29, 30]. The double–layer winding single–medium configuration is shown in Fig. 5.2, as the result of a FEM (finite element) time-harmonic simulation.

$\frac{\nu}{t}$	Difference Total Losses [%]
1	0
5	7.5
7	5.8
11	7.5
13	-
17	6.8
total	5.6

Table 5.1: Comparison between FEM and analytical model, 12–13 double–layer winding
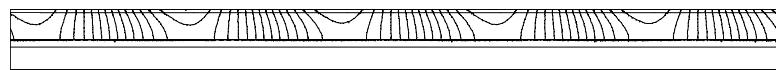
Figure 5.1: FEM model corresponding to 12–13 configuration
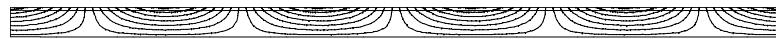
Figure 5.2: straight–lined model with single medium

5.2. The Index of rotor losses

Considering the one–layer straight lined model presented in Fig. 5.2 a synthetic index to study of the phenomenon of rotor losses [29, 45] can be derived. The properties of the materials which will be considered in this study are now fixed. They are presented in Table 5.2. The specific induced losses per surface unit q_ν on the medium expressed

Table 5.2: Material properties used in the model.

Material		PMs	back iron	back iron
		NdFeB	linear massive	linear saturated
σ	(MS/m)	0.67	10	10
μ_r	$(-)$	1.05	5000	50

in equation (5.1). The index ν refers to the harmonic order. These specific losses q_ν of the single–layer model can be used to compare the effect of different windings on the same material, whose geometry and characteristic must be assigned to the model. This comparison is done in Table 5.3: a permanent magnet (PM) block is considered with a thickness of almost 0.03 m. The total specific losses q_l result as the sum of the losses computed for each harmonic order ν, that is in equation (5.2).

$$q = \frac{\xi^4}{\sqrt[4]{(\pi^4 + \xi^4)^3}} \frac{1}{\cos(\varphi/2)} \frac{\hat{K}_{s\nu}^2}{4\sigma\tau_\nu} k_{ym} \tag{5.1}$$

$$q_l = \sum_\nu q_\nu \tag{5.2}$$

Table 5.3: Computation of q_l for different basic windings, double layer

Basic winding	12–10	12–11	12–13
q_l in PMs (W/m^2)	2400	3140	4380

The convenience of considering the index as a dimensionless quantity is shown in [45]: q is divided by $\hat{K}_s^2/(\sigma\tau_p)$, where $\hat{K}_s$ and τ_p refer to the main harmonic, of order $\nu = p$.
The ratio $\hat{K}_{s\nu}/\hat{K}_s = k_{w\nu}/k_w$, where $k_{w\nu}$ is the winding factor of the harmonic of order ν and k_w is the winding factor of the main harmonic. Since $\tau_p/\tau_\nu = \nu/p$, the index of rotor losses can be defined as

$$I_{rl} = \sum_\nu \frac{\xi^4}{\sqrt[4]{(\xi^4 + \pi^4)^3}} \left(\frac{k_{w\nu}}{k_w}\right)^2 \frac{\nu}{p} k_{gap} \tag{5.3}$$

The main advantage the index of rotor losses in equation (5.3) is the simplicity. For a given winding with a number of slots Q and a number of pole pairs p, it is easy to compute the winding factors and the frequency seen by the rotor referring to the various harmonics. The specific wavelength ξ is then defined for each harmonic order

and k_{gap} is defined by the ratio g/D. It is then possible to compute the index presented in equation (5.3). An expression for k_{gap} is provided in [45] as:

$$k_{gap} = k\, e^{-\left(a\frac{g}{D}+b\right)\nu} \tag{5.4}$$

where g is the air–gap and D is the stator diameter. The coefficients k, a, and b are achieved by comparing the losses achieved by means of a straight–lined model with a single medium (see Chapter 3) and the losses achieved by means of a straight–lined model with two media.
The results regarding materials listed in Table 5.2 are here shown.

magnet	$k = 1$	$a = 4.2$	$b = 0.00017$
iron	$k = 1.25$	$a = 15$	$b = 0.040$

They have been achieved by the Authors with g/D in the range 0.002 to 0.01.

5.3. Applying the Index to large PM machines

The aim of this study is to apply the index of rotor losses in equation (5.3) to compare the effect on losses of different windings on large direct drive PM machines. According to the real machines studied in this doctoral work and to the FEM models developed for large machines (see Chapters 2 and 3) the size of the considered diameter D is within the interval:

$$1.5\ m < D < 4\ m \tag{5.5}$$

The same models have been applied to smaller machines ($D \sim 0.1m$), this can also be seen in [30, 45]. Table 5.4 summarizes the main characteristics of the basic geometry chosen to apply the index. The double–layer winding type is considered at the beginning.

Table 5.4: Basic geometry to apply the index of rotor losses in equation (5.3)

Quantity		Value
Stator inner radius	(mm)	~ 2000
Length	(mm)	1000
PM thickness	(mm)	~ 30
Iron yoke thickness	(mm)	~ 40
Airgap thickness	(mm)	~ 5
Frequency ($\nu = p$)	(Hz)	$14 - 23$
Winding type		double–layer

The considered basic windings are:

- 12 slots, 10 poles;

- 12 slots, 11 poles (that means 24 slots, 22 poles);

- 12 slots, 13 poles (that means 24 slots, 26 poles);

The harmonic analysis of the magneto–motive force (MMF), the relative electrical loading ($K_{w,\nu}$) and frequencies ($f_{r,\nu}$) seen from the rotor reference frame of the basic windings under study are shown in Fig. 5.3, Fig. 5.4 and Fig. 5.5. The shape of the MMF is also shown for each winding.

It is worth pointing out that all the basic windings under study must be adapted to the geometry proposed in Table 5.4. This is achieved by choosing a proper periodicity for the machine in the different cases.
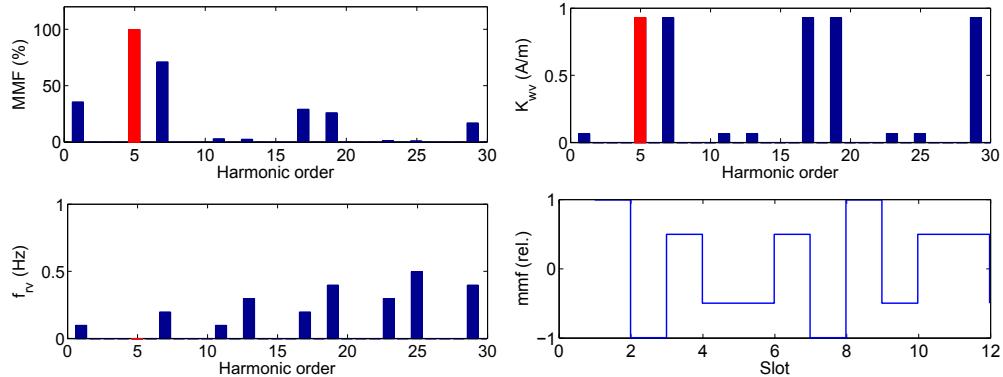
Figure 5.3: Basic DL 12–10 winding harmonics characteristics
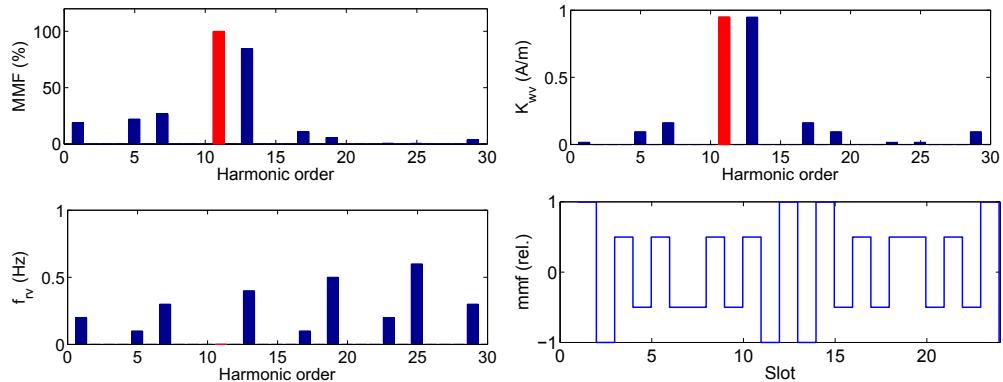
Figure 5.4: Basic DL 12–11 winding harmonics characteristics
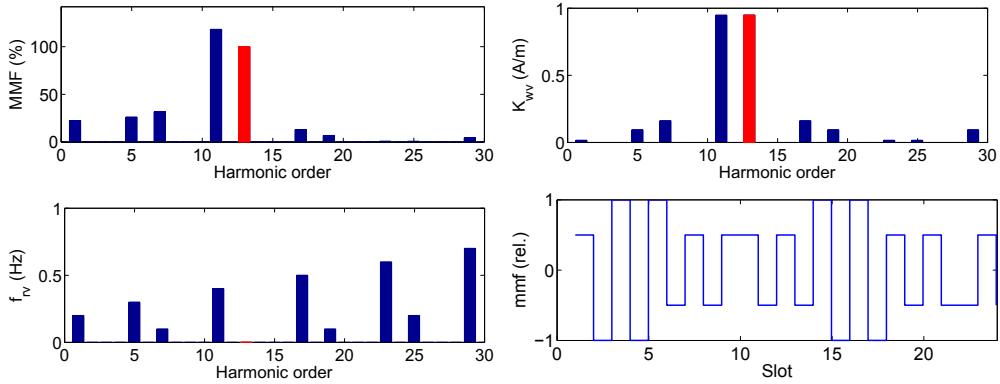
Figure 5.5: Basic DL 12–13 winding harmonics characteristics

The first step is to calculate the index which corresponds to the straight–lined model of Fig. 5.2. The considered material is PM again. This choice is due to the fact that the rotor losses cause an increase of the temperature in PMs if rare-earths material is considered. Both the residual flux density and the magnetic field of the knee of the B-H curve are reduced, as reported in Fig. 5.6 for NdFeB.
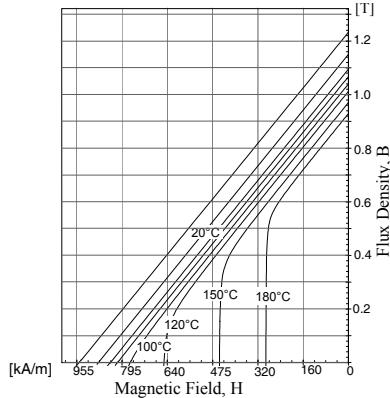
Figure 5.6: Variation of B-H curve for a Neodymium-Iron-Boron PMs with the temperature

The reduction of the residual flux density causes a decrease of back electromotive force (EMF) and of the motor performance. The reduction of the magnetic field increases the risk of an irreversible demagnetization of the PMs. Rare earths PMs can be considered "precious material" in large direct drive PM machines as well, due to their cost as can be read in literature [46,47]. It is then crucial to limit losses in PMs. Table 5.3 is extended in Table 5.5, including the computation of the index.

The trend of the computed q_l and index agrees for each basic windings considered. This is more evident if both the index and q_l are written considering the values of the 12–10 winding as the 100% base. This is done in Table 5.6.

Table 5.5: Computation of q_l and index, different basic windings, double layer

Basic winding	12–10	12–11	12–13
q_l in PMs (W/m^2)	2400	3140	4380
Index in PMs	0.086	0.1	0.13

Table 5.6: Computation of q_l and index, per–cent, double layer

Basic winding	12–10	12–11	12–13
q_l in PMs (%)	100	130	183
Index in PMs (%)	100	116	151

The Index seems then to be a good instrument to evaluate the impact of rotor losses on a PMs medium. The effect of the airgap is included. It is then necessary to evaluate its employment considering more realistic machine configuration.

5.3.1. Transition to Halbach structure

The second step towards a realistic machine configuration is to place the PM medium on a back-iron yoke. That way the rotor structure of an Halbach machine with a continuous magnet ring is defined. To calculate the specific induced losses q_l as per equations (5.1–5.2) a straight–lined three–media model is required (Fig. 5.7). This model has been considered with two different values of the relative magnetic permeability μ_r of the back iron. It can be calculated both analytically or via FEM analysis. Losses are finally referred to the chosen geometry proposed in Table 5.4.

CONFIG. A
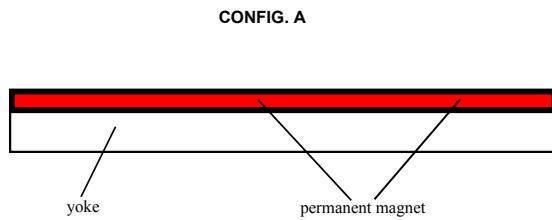
Figure 5.7: Three–media straight model for Halbach structure

A circuital segmentation of eddy current in the PM ring is introduced, as it is divided into insulated blocks. Fig. 5.8 shows the modified model, which requires a time-harmonic FEM simulation. The computed values of rotor losses and index are listed in Table 5.7.

CONFIG. C
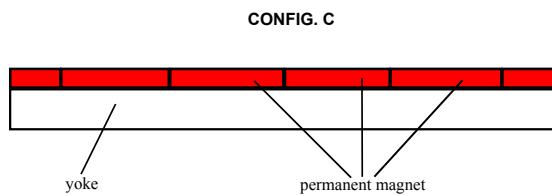
Figure 5.8: Model for Halbach structure, insulated PMs

Table 5.7: Computation of Rotor Losses, different basic winding,double–layer winding

BASIC WINDING PART	12–10			12–11			12–13		
	Yoke (kW)	PMs (kW)	Total (kW)	Yoke (kW)	PMs (kW)	Total (kW)	Yoke (kW)	PMs (kW)	Total (kW)
Halbach FEM $\mu_r = 5000$	3.4	36	39.4	3	43	46	5.9	73	79
Halbach An. $\mu_r = 5000$	1.9	34	35.9	2	41.6	43.6	3.7	71	75
Halbach An. $\mu_r = 50$	8.2	24.6	32.8	12.8	35.7	48.5	24	58	81
Halbach FEM Ins.$\mu = 5000$	9.5	24.5	34.1	6.4	29.5	35.8	9.7	35.7	45.4
RL Index (dimensionless)	-	0.086	-	-	0.10	-	-	0.13	-

The analysis of the three–media straight–lined models leads to the following considerations:

- there is a good agreement in the yoke losses and total losses of the analytical and FEM models;

- the losses computed in PMs with the analytical model are lower than losses predicted with FEM time-harmonic, otherwise their trend in respect to the basic–winding agrees with both the models;

- if the saturation of the iron yoke increases (i.e. the relative magnetic permeability is lower) the magnet losses reduce, while the yoke losses increase. The total losses generally increase, but they reduce in the basic 12–10 structure;

- if the magnet ring is electrically segmented the magnet losses reduce, while the yoke losses increase. The total losses decrease in all the basic windings considered.

It is worth noticing that the trend of the index of rotor losses in PMs in respect to the basic windings still agrees with the one predicted by the straight–lined models. This can be noticed in Fig. 5.9, where the behavior of the losses in PMs is shown considering the values of the 12–10 winding as the 100% reference.
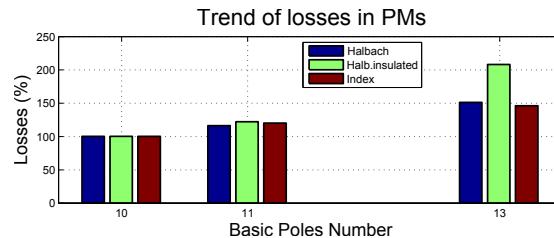
Figure 5.9: Trend of losses in PMs of Halbach structure and index

Table 5.8: Different Rotor Structure

Structure			Conductivity (MS)			Permeability		
PART			Yoke	PMs	Slot	Yoke	PMs	Slot
Halbach FEM $\mu_r = 5000$	A		10	0.66	-	5000	1.05	-
Halbach An. $\mu_r = 5000$	A		10	0.66	-	5000	1.05	-
Halbach An. $\mu_r = 50$	A		10	0.66	-	50	1.05	-
Magnet Only	B		-	0.66	-	-	1.05	-
RL Index (dimensionless)	B		-	0.66	-	-	1.05	-
Halbach FEM Ins.$\mu = 5000$	C		10	0.66	0	5000	1.05	1
SPM $\mu = 5000$	D		10	0.66	0	5000	1.05	1
SPM $\mu = 5000$ ferrite	D		10	0	0	5000	1.05	1
SPM $\mu = 50$	D		10	0.66	0	50	1.05	1
SPM/IPM $\mu = 5000$	E		10	0.66	0	5000	1.05	1
SPM/IPM $\mu = 5000$ laminated yoke	E		0	0.66	0	5000	1.05	1
IPM $\mu = 5000$ laminated yoke/slot	E		0	0.66	0	5000	1.05	1
IPM $\mu = 5000$ aluminum yoke/lam.slot	E		25	0.66	0	5000	1.05	1
IPM $\mu = 5000$ aluminum yoke/lam.nl.slot	E		25	0.66	0	$\mu(B)$	1.05	1
IPM $\mu = 5000$ al.yoke/lam.nl.slot/ferrite	E		25	0	0	$\mu(B)$	1.05	1

5.3.2. Transition to SPM and IPM structure

The third step is to divide the continuous magnet ring of the Halbach structure into discrete PM blocks. In this section simple rectified models are employed first to operate the transition to surface permanent magnet (SPM) structures of the rotor.

As the fourth step of this study, the structure of the rotor is then switched to interior permanent magnet (IPM) with tangential magnetization of PMs: the PM discrete blocks are the same used in the SPM model, but they are rotated and buried into the magnetizing part. All the rotor structures which have been considered are summarized in Fig. 5.10.

The following points shows the strategy to jump from SPM to IPM structure:

- PMs have been rotated: the structure is still SPM, but PMs are vertically placed on the rotor yoke;

- the rotor yoke is then laminated, i.e. its electrical conductivity is set to 0;

- the same lamination in now employed in the slots of the rotor, instead of filling them with air;

- the material of the rotor yoke is now set to vacuum;

- the yoke of the rotor is then set to aluminum;

- ferrite PMs (zero conductivity) are then used in order to evaluate the impact on the other parts of the rotor of the machine.

The characteristics of all the related materials employed are shown in Table 5.8. The machine operates with 9.8 kA total current in slot and 14.3 r/min speed, DL winding is still considered. The results of the FEM simulations with the current sheet method and double layer winding are collected in Table 5.9 Some considerations can be done if DL winding is considered:

CONFIG. A

yoke   permanent magnet

CONFIG. B

permanent magnet

CONFIG. C

yoke   permanent magnet

CONFIG. D   slot

yoke   permanent magnet

CONFIG. E

slot   permanent magnet

yoke
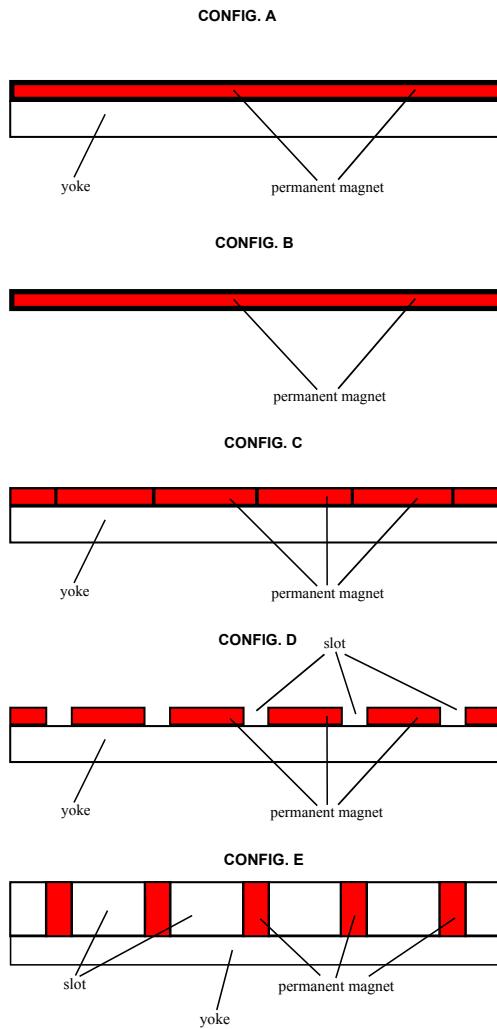
Figure 5.10: Rotor structure A,B,C,D,E

- the good agreement of the analytical and FEM model is proved in structure A;

- the tendency of losses in PMs agrees with the Rotor Losses Index (RL INDEX) behavior in all the structures A, B, C, D, E;

- in the transitions between structure A and D losses in yoke increases while losses in PMs decreases, both with the magnetic permeability of the yoke set to 5000 and 50 (the shielding effect of the continuous magnet ring is getting weaker);

- in the transitions between structure A and D total losses in yoke increases in all the considered basic windings;

- in structure A losses in PMs are decoupled from the yoke ones if there is vacuum in rotor slots. This can be noticed in the IPM configuration with vacuum–slots: the losses in PMs don't vary neither with massive yoke nor with laminated yoke;

- in structure E losses in PMs are decoupled from the yoke ones if rotor slots are

Table 5.9: Results of the computation of Rotor Losses for different basic winding and rotor structure, 1 m stack length, double layer

BASIC WINDING PART	12–10 Yoke (kW)	PMs (kW)	Total (kW)	12–11 Yoke (kW)	PMs (kW)	Total (kW)	12–13 Yoke (kW)	PMs (kW)	Total (kW)
Halbach FEM $\mu_r = 5000$	3.4	36	39.4	3	43	46	5.9	73	79
Halbach An. $\mu_r = 5000$	1.9	34	35.9	2	41.6	43.6	3.7	71	75
Halbach An. $\mu_r = 50$	8.2	24.6	32.8	12.8	35.7	48.5	24	58	81
Magnet Only	-	30	30	-	38	38	-	53	53
RL Index	-	0.086	-	-	0.10%	-	-	0.13%	-
Continuous insulated $\mu = 5000$	9.5	24.5	34.1	6.4	29.5	35.8	9.7	35.7	45.4
SPM $\mu = 5000$	9.5	16	25.5	6.4	18.4	24.8	9.8	21	31
SPM $\mu = 5000$ ferrite	9.6	-	9.6	6.5	-	6.5	9.9	-	9.9
SPM $\mu = 50$	11	14	25	14	16.5	30.5	26	18.4	44.4
SPM/IPM $\mu = 5000$	2.5	4.1	6.6	2	4.9	6.9	2.1	6.1	8.2
SPM/IPM $\mu = 5000$ laminated yoke	-	4.1	4.1	-	4.9	4.9	-	6.1	6.1
IPM $\mu = 5000$ laminated yoke/slot	-	2.5	2.5	-	2.7	2.7	-	2.6	2.6
IPM $\mu = 5000$ air yoke/lam.slot	-	15.5	15.5	-	28	28	-	54.4	54.4
IPM $\mu = 5000$ al. yoke/lam.slot	8.2	15.5	23.6	18	30	48	33.4	58.7	92.2
IPM $\mu = 5000$ al. yoke/lam.nl.slot	8.2	15.5	23.6	18	30	48	33.5	58.8	92.3
IPM $\mu = 5000$ al.yk/lam.nl.slot/ferr.	8.2	-	8.2	18	-	18	33.5	-	33.5

made with laminated magnetic steel and rotor yoke is not magnetic: they don't vary neither with "air" nor with "aluminum" yoke;

- if rare-earths PMs are replaced with zero-conductive PMs (ferrite), the effect on the losses of the other part of the rotor are negligible, i.e. the effect is the same of removing the losses in PMs from the total amount. This can be noticed both with IPM and SPM structure.

5.3.3. Employing The Single–Layer Winding

In the previous paragraph it has been shown that the rotor losses index is a good and fast instrument to predict the losses in PMs of different rotor structures. The MMF harmonics obtained starting from different basic–windings have been used. The double layer–winding has been considered.

In this paragraph the single–layer (SL) is considered. The harmonic analysis of the magneto–motive force (MMF) and the relative electrical loading ($K_{w,\nu}$) of the basic windings under study are shown in Fig. 5.11, Fig. 5.12 and Fig. 5.13. It is worth pointing out that all the basic windings under study is still adapted to the geometry proposed in Table 5.4, by choosing a proper periodicity for the machine in the different cases. Despite its reduced MMF harmonic content (Chapter 3) the DL winding is often affected by critical technical reliability, especially in large electrical machines.

It is then interesting to repeat the study using a more common SL winding configuration of the armature part. Results of the FEM simulations with the current sheet method using SL winding are collected in Table 5.10.

Some considerations can be done if SL winding is considered:

- the good agreement of the analytical and FEM model is proved again;

- the tendency of losses in PMs agrees with the Rotor Losses Index (RL INDEX) behavior in structure A, B, C, D;
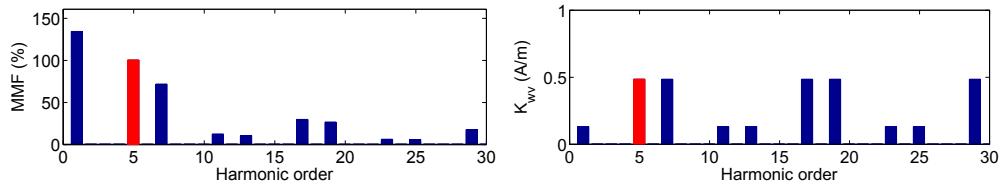
Figure 5.11: Basic SL 12–10 winding harmonics characteristics
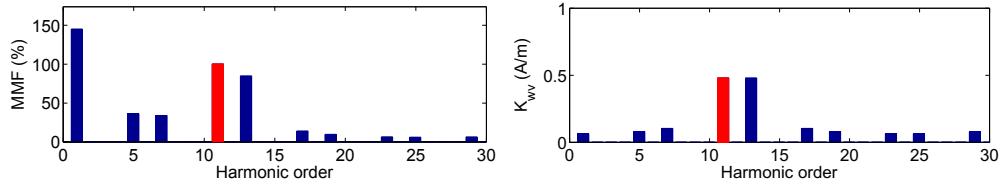
Figure 5.12: Basic SL 12–11 winding harmonics characteristics
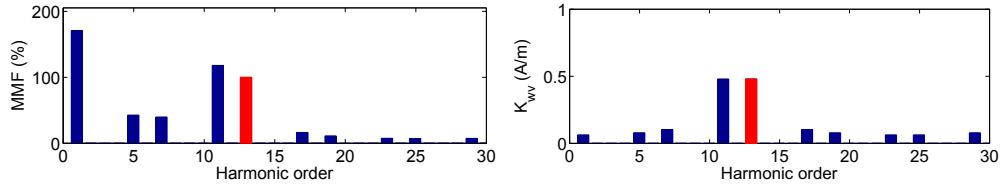
Figure 5.13: Basic SL 12–13 winding harmonics characteristics

Table 5.10: Results of the computation of Rotor Losses for different basic winding and rotor structure, 1 m stack length, single layer

BASIC WINDING PART	**12–10** Yoke (kW)	PMs (kW)	Total (kW)	**12–11** Yoke (kW)	PMs (kW)	Total (kW)	**12–13** Yoke (kW)	PMs (kW)	Total (kW)
Continuous $\mu = 5000$	23	177	200	7.5	90	98	10	126	136
Continuous Analytical $\mu = 5000$	18	178	196	7.5	90	98	10	126	136
Continuous Analytical $\mu = 50$	43	60	103	26	49	75	38	75	113
Magnet Only Analytical	-	51	-	-	45	-	-	62	-
RL Index	-	0.16	-	-	0.12	-	-	0.16& -	
Continuous insulated $\mu = 5000$	108	49	158	135	38	173	143	43	186
SPM $\mu = 5000$	108	28	137	132	23	160	145	25	170
SPM $\mu = 5000$ ferrite	108	-	108	132	-	132	145	-	145
SPM $\mu = 50$	72	16	92	38	18	56	53	20	73
SPM/IPM $\mu = 5000$	27	5.4	32.7	61	5.7	67	61	6.7	67
SPM/IPM $\mu = 5000$ laminated yoke	-	5.4	5.4	-	5.9	5.9	-	6.9	6.9
IPM $\mu = 5000$ laminated yoke/slot	-	4.2	4.2	-	3.9	3.9	-	3.5	3.5
IPM $\mu = 5000$ air yoke/lam.slot	-	23	23	-	32	32	-	60	60
IPM $\mu = 5000$ al. yoke/lam.slot	20	24	44	23	34	57	39	65	104
IPM $\mu = 5000$ al. yoke/lam.nl.slot	20	24	44	23	34	57	39	65	104
IPM $\mu = 5000$ al.yk/lam.nl.slot/ferr.	20	-	20	23	-	23	39	-	39

- the tendency of losses in PMs does not agree with the Rotor Losses Index (RL INDEX) behavior in structure E;

- in the transitions between structure A and D losses in yoke increases while losses in PMs decreases (the shielding effect of the continuous magnet ring is getting weaker);

- in the transitions between structure A and D total losses in yoke decreases in the basic 12–10 winding;

- in the transitions between structure A and D total losses in yoke increases in the basic 12–11 and 12–13 windings;

- in structure A losses in PMs are decoupled from the yoke ones if there is vacuum in rotor slots. This can be noticed in the IPM configuration with vacuum–slots: the losses in PMs don't vary neither with massive yoke nor with laminated yoke;

- in structure E losses in PMs are decoupled from the yoke ones if rotor slots are made with laminated magnetic steel and rotor yoke is not magnetic: they don't vary neither with "air" nor with "aluminum" yoke;

- if rare-earths PMs are replaced with zero-conductive PMs (ferrite), the effect on the losses of the other part of the rotor are negligible, i.e. the effect is the same of removing the losses in PMs from the total amount. This can be noticed both with IPM and SPM structure.

It is worth noticing that the main difference in respect to the DL winding case is that the trends of losses in PMs obtained with FEM in the IPM structure do not agree with the prediction of the RL Index. The RL Index behavior agrees with FEM if the 12–10 basic winding is removed from the study. It is then necessary to evaluate the behavior of the index using a larger number of different windings. Some other examples will be added while choosing the number of slots and poles for the new LW30A direct drive generator.

5.4. Torque of the machine:the winding factor

In Chapter 2 the analytical model to study some large direct drive PM machines has been proposed. It has been shown that it can be applied to the study of existing Leitwind and Leitner PM machines, due to the results of FEM models and test bench activity.

The electromagnetic power can be calculated as per equation (5.6), in order to obtain the electromagnetic torque T_{el}.

$$P_{el} = 3E_{0,load}I_{line}N_{line} \tag{5.6}$$

$$T_{el}\frac{2\pi}{60}n = 3E_{0,load}I_{line}N_{line} = P_{el} \tag{5.7}$$

$$T_{el} = \frac{P_el}{\frac{2\pi}{60}n} \tag{5.8}$$

Equation (5.8) can be written again considering the airgap flux density at load $B_{g,0,load}$, the electrical loading of the machine $\hat{K}_s$, the diameter D and active length L_{stk}. Equation (5.9) is then modified according to the definition of electrical loading $\hat{K}_s = k_w\frac{\hat{I}_{slot}}{p_s}$ as per equation (5.10), where k_w is the winding factor, $\hat{I}_{slot}$ the total current in slot and p_s the stator pitch.

$$T_{el} = \hat{K}_s B_{g0,load,av}D^2 L_{stk} \tag{5.9}$$

$$T_{el} = k_w\frac{\hat{I}_{slot}}{p_s}B_{g0,load}D^2 L_{stk} \tag{5.10}$$

If the definition of k_w is considered, the following can be written for a 96 slots, 104 poles, SL winding machine, while more general definition can be found in [11]:

$$k_p = \cos(\frac{\alpha_{stroke}}{2}) \tag{5.11}$$

$$k_d = \frac{\sqrt{2}}{2}\sqrt{1 + \cos(2\alpha_{stroke})} \tag{5.12}$$

$$k_w = k_p k_d \tag{5.13}$$

α_{stroke} is the angular shifting related to the strokes of the star of slot and it is related to the harmonic order ν. When $\nu = p$ it is then possible to establish a proportionality between the winding factor and the electromagnetic torque, considering that the geometry and the airgap flux density of the machine are fixed:

$$T_{el} \sim k_w = k_p k_d \tag{5.14}$$

The winding factor k_w results then to be the second index to be used in selecting the proper number of slots and poles ratio for a new design, resulting to be the torque index.

Impact of the Carter Factor

In equation (5.10) the influence of the number of slots Q and of the number of poles 2p is considered in the winding factor k_w only, which is related to the winding itself and acts on the value of the electrical loading $\hat{K}_s$.

The analytical computation in Chapter 2 shows that the average fundamental value of the airgap flux density $B_{g0,load,av}$ depends on the geometry of the polar shoe (α_{ps} is the angular width) and on the shape of the slots of the stator. The equivalent value of the airgap g" increases and so the flux density gets smaller: the Carter factor of the stator take this aspect into account. Equations (5.15) (5.16) (5.17) (5.18) summarizes the influence of Kc, while the saturation $ksat$ depends on the saturation of the magnetic circuit: the meaning of symbols is the same as per Chapter 2.

$$B_{g0,l,av} = B_{g0,l}\sin(\alpha_{ps}^e/2) \tag{5.15}$$

$$Kc = \frac{1}{1 - \frac{w_s}{p_s} + [\frac{4}{\pi}\frac{g}{p_s}\ln((1 + \frac{pi}{4})\frac{w_s}{g})]} \tag{5.16}$$

$$B_{g0,l} = \frac{B_{rem}}{\frac{\tau_p - t_{pm}}{2h_p m} + \frac{2g \cdot Kc \cdot ksat\mu_{rec}}{t_{pm}}} \tag{5.17}$$

$$g'' = g \cdot Kc \cdot ksat \tag{5.18}$$

Equation (5.15) can be replaced by equation (5.16) considering the Carter factor of the rotor Kcr together with the Carter factor of the stator: this is written in equation (5.19).

$$B_{g0,l,av} = \frac{B_{rem}}{\frac{\tau_p - t_{pm}}{2h_p m} + \frac{2g \cdot Kc \cdot Kcr \cdot ksat\mu_{rec}}{t_{pm}}} \tag{5.19}$$

The electromagnetic torque of the machine is reduced both by Kc and Kcr because it is proportional both to kw and $B_{g0,l,av} = f(KcKcr)$.

$$T_{el} \sim k_w \cdot B_{g0,l,av}(KcKcr) \tag{5.20}$$

5.5. Pre-sizing of the LW30A generator

In this section the development of LTW 3MW MONO generators starts, the RL Index and the winding factor kw as a torque index will be used. The models employed in the previous sections are fit to the new generator size according to the following specifications, given by LTW:

- The outer diameter of the active part is $\sim 4000mm$;

- Flux concentration in rotor;

- Concentrated tooth windings with single or double layer;

- Segmentation of the stator is required;

- The rated torque of the machine is $\sim 2MNm$;

- The speed range of the machine is $12 - 18r/min$;

- The machine must be as short as possible, according to the torque specified;

- The machine is for low voltage application;

- The power factor $cos\phi$ must not be lower than 0.8;

- Magnet employed is NdFeB;

- The coercive field Hc is greater than $850000A/m$;

- The remanence Brem is greater than $1.17T$ at $20C$ magnet temperature.

5.5.1. Selection of the winding: slot and poles number

In order to choose the slots and poles number $Q/2p$ some criteria has been adopted, as suggested in $[11, 48]$:

- The number of slot Q is higher than 50 and lower than 200;

- The number of poles 2p is higher than 40 and lower than 150;

- The periodicity of the machine t is between 1 and 15, this is related to desired number of parallel paths;

- The number of phases m is 3;

- The number of strokes of the star of slot $Q/(t)$ is even;

- The number of strokes per phase of the star of slot $Q/(m*t)$ is even and so the winding is feasible;

- Q is even and the coil throw yq is odd and so both the DL and SL windings are feasible;

- $Q/(2*t)$ is even, and so the harmonic orders of the DL and SL windings are the same;

- The groups with the same number of coils $Q/(m* \mid Q-2p \mid)$ is integer, in order to allow modularity;

- The groups of coils $\mid Q-2p \mid$ is integer, in order to allow the segmentation of the stator;

- Reduction of the MMF harmonics in the airgap.

In table 5.11 the windings which satisfy the proposed criteria are listed with $60 < Q < 180$. The meaning of the following symbols is explained:

- kdds is the distribution factor corresponding to the DL winding;

- kpds is the pitch factor corresponding to the DL winding;

- kwds is the total winding factor corresponding to the DL winding;

- kdss is the distribution factor corresponding to the SL winding;

- kpss is the pitch factor corresponding to the SL winding;

- kwss is the total winding factor corresponding to the SL winding.

In order to erase useless configuration, t has been considered as 2, 3, 5, 7 or multiple (lower than 14), while Q is between 72 and 168, new configurations are presented in table 5.5.1. This requirement is due to the maximum number of parallel paths desired by the power electronic interface.

Table 5.11: first winding selection in LW30A development.

Q	2p	t	Q/(mt)	Q/t	Q/(2t)	yq	kdds	kpds	kwds	kdss	kpss	kwss
60	50	5	4	12	6	1	0,9659	0,9659	0,933	1	0,9659	0,9659
60	58	1	20	60	30	1	0,9554	0,9986	0,9541	0,9567	0,9986	0,9554
72	60	6	4	12	6	1	0,9659	0,9659	0,933	1	0,9659	0,9659
60	62	1	20	60	30	1	0,9554	0,9986	0,9541	0,9567	0,9986	0,9554
72	66	3	8	24	12	1	0,9577	0,9914	0,9495	0,9659	0,9914	0,9577
72	68	2	12	36	18	1	0,9561	0,9962	0,9525	0,9598	0,9962	0,9561
60	70	5	4	12	6	1	0,9659	0,9659	0,933	1	0,9659	0,9659
72	70	1	24	72	36	1	0,9552	0,999	0,9543	0,9561	0,999	0,9552
84	70	7	4	12	6	1	0,9659	0,9659	0,933	1	0,9659	0,9659
72	74	1	24	72	36	1	0,9552	0,999	0,9543	0,9561	0,999	0,9552
72	76	2	12	36	18	1	0,9561	0,9962	0,9525	0,9598	0,9962	0,9561
72	78	3	8	24	12	1	0,9577	0,9914	0,9495	0,9659	0,9914	0,9577
96	80	8	4	12	6	1	0,9659	0,9659	0,933	1	0,9659	0,9659
84	82	1	28	84	42	1	0,9552	0,9993	0,9545	0,9558	0,9993	0,9552
72	84	6	4	12	6	1	0,9659	0,9659	0,933	1	0,9659	0,9659
84	86	1	28	84	42	1	0,9552	0,9993	0,9545	0,9558	0,9993	0,9552
96	88	4	8	24	12	1	0,9577	0,9914	0,9495	0,9659	0,9914	0,9577
108	90	9	4	12	6	1	0,9659	0,9659	0,933	1	0,9659	0,9659
96	92	2	16	48	24	1	0,9556	0,9979	0,9536	0,9577	0,9979	0,9556
96	94	1	32	96	48	1	0,9551	0,9995	0,9546	0,9556	0,9995	0,9551
84	98	7	4	12	6	1	0,9659	0,9659	0,933	1	0,9659	0,9659
96	98	1	32	96	48	1	0,9551	0,9995	0,9546	0,9556	0,9995	0,9551
96	100	2	16	48	24	1	0,9556	0,9979	0,9536	0,9577	0,9979	0,9556
120	100	10	4	12	6	1	0,9659	0,9659	0,933	1	0,9659	0,9659
108	102	3	12	36	18	1	0,9561	0,9962	0,9525	0,9598	0,9962	0,9561
96	104	4	8	24	12	1	0,9577	0,9914	0,9495	0,9659	0,9914	0,9577
108	106	1	36	108	54	1	0,9551	0,9996	0,9547	0,9555	0,9996	0,9551
108	110	1	36	108	54	1	0,9551	0,9996	0,9547	0,9555	0,9996	0,9551
120	110	5	8	24	12	1	0,9577	0,9914	0,9495	0,9659	0,9914	0,9577
132	110	11	4	12	6	1	0,9659	0,9659	0,933	1	0,9659	0,9659
96	112	8	4	12	6	1	0,9659	0,9659	0,933	1	0,9659	0,9659
108	114	3	12	36	18	1	0,9561	0,9962	0,9525	0,9598	0,9962	0,9561
120	116	2	20	60	30	1	0,9554	0,9986	0,9541	0,9567	0,9986	0,9554
120	118	1	40	120	60	1	0,955	0,9997	0,9547	0,9554	0,9997	0,955
144	120	12	4	12	6	1	0,9659	0,9659	0,933	1	0,9659	0,9659
120	122	1	40	120	60	1	0,955	0,9997	0,9547	0,9554	0,9997	0,955
120	124	2	20	60	30	1	0,9554	0,9986	0,9541	0,9567	0,9986	0,9554
108	126	9	4	12	6	1	0,9659	0,9659	0,933	1	0,9659	0,9659
120	130	5	8	24	12	1	0,9577	0,9914	0,9495	0,9659	0,9914	0,9577
132	130	1	44	132	66	1	0,955	0,9997	0,9547	0,9553	0,9997	0,955
156	130	13	4	12	6	1	0,9659	0,9659	0,933	1	0,9659	0,9659
144	132	6	8	24	12	1	0,9577	0,9914	0,9495	0,9659	0,9914	0,9577
132	134	1	44	132	66	1	0,955	0,9997	0,9547	0,9553	0,9997	0,955
144	136	4	12	36	18	1	0,9561	0,9962	0,9525	0,9598	0,9962	0,9561
144	138	3	16	48	24	1	0,9556	0,9979	0,9536	0,9577	0,9979	0,9556
120	140	10	4	12	6	1	0,9659	0,9659	0,933	1	0,9659	0,9659
144	140	2	24	72	36	1	0,9552	0,999	0,9543	0,9561	0,999	0,9552
168	140	14	4	12	6	1	0,9659	0,9659	0,933	1	0,9659	0,9659
144	142	1	48	144	72	1	0,955	0,9998	0,9548	0,9552	0,9998	0,955
144	146	1	48	144	72	1	0,955	0,9998	0,9548	0,9552	0,9998	0,955
144	148	2	24	72	36	1	0,9552	0,999	0,9543	0,9561	0,999	0,9552
144	150	3	16	48	24	1	0,9556	0,9979	0,9536	0,9577	0,9979	0,9556
180	150	15	4	12	6	1	0,9659	0,9659	0,933	1	0,9659	0,9659

5.5.2. First Finite Element Comparison

A first FEM comparison has been done starting from the 12–10 basic windings and the 12–11 basic windings. The periodicity of the winding is then chosen again according to the geometry proposed in Table 5.4. The flux concentration rotor structure has been chosen, i.e. the IPM structure E as per Table 5.8. FEM models have been realized using the same stator geometry (i.e. the number of slot Q is fixed) and changing the size of the rotor poles in order to keep the mass of PMs fixed:

- the torque have been evaluated trough magnetostatic DC FEM models (Fig. 5.14);

Table 5.12: second winding selection in LW30A development.

Q	2p	t	Q/(mt)	Q/t	Q/(2t)	yq	kdds	kpds	kwds	kdss	kpss	kwss
72	60	6	4	12	6	1	0,9659	0,9659	0,933	1	0,9659	0,9659
72	68	2	12	36	18	1	0,9561	0,9962	0,9525	0,9598	0,9962	0,9561
72	76	2	12	36	18	1	0,9561	0,9962	0,9525	0,9598	0,9962	0,9561
96	80	8	4	12	6	1	0,9659	0,9659	0,933	1	0,9659	0,9659
72	84	6	4	12	6	1	0,9659	0,9659	0,933	1	0,9659	0,9659
96	88	4	8	24	12	1	0,9577	0,9914	0,9495	0,9659	0,9914	0,9577
96	92	2	16	48	24	1	0,9556	0,9979	0,9536	0,9577	0,9979	0,9556
96	100	2	16	48	24	1	0,9556	0,9979	0,9536	0,9577	0,9979	0,9556
120	100	10	4	12	6	1	0,9659	0,9659	0,933	1	0,9659	0,9659
96	104	4	8	24	12	1	0,9577	0,9914	0,9495	0,9659	0,9914	0,9577
96	112	8	4	12	6	1	0,9659	0,9659	0,933	1	0,9659	0,9659
120	116	2	20	60	30	1	0,9554	0,9986	0,9541	0,9567	0,9986	0,9554
144	120	12	4	12	6	1	0,9659	0,9659	0,933	1	0,9659	0,9659
120	124	2	20	60	30	1	0,9554	0,9986	0,9541	0,9567	0,9986	0,9554
144	132	6	8	24	12	1	0,9577	0,9914	0,9495	0,9659	0,9914	0,9577
144	136	4	12	36	18	1	0,9561	0,9962	0,9525	0,9598	0,9962	0,9561
120	140	10	4	12	6	1	0,9659	0,9659	0,933	1	0,9659	0,9659
144	140	2	24	72	36	1	0,9552	0,999	0,9543	0,9561	0,999	0,9552
168	140	14	4	12	6	1	0,9659	0,9659	0,933	1	0,9659	0,9659
144	148	2	24	72	36	1	0,9552	0,999	0,9543	0,9561	0,999	0,9552

- the losses in rotor have been evaluated trough the current sheet AC method(Fig. 5.18):

- the joule losses in the winding have been evaluated through the AC time harmonic model of the stator slot (Fig. 5.16);

- the inputs to this first FEM comparison are listed in Table 5.13.
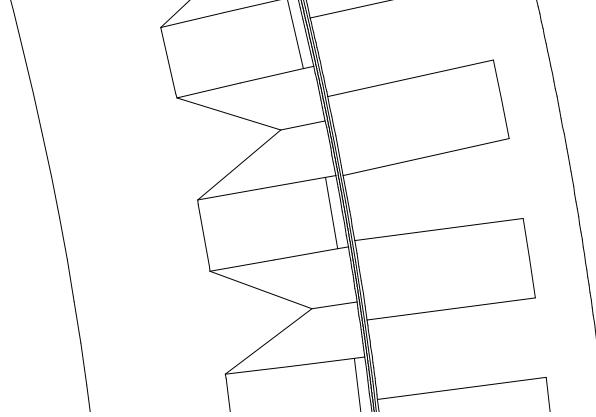
Figure 5.14: Magnetostatic FEM model

;
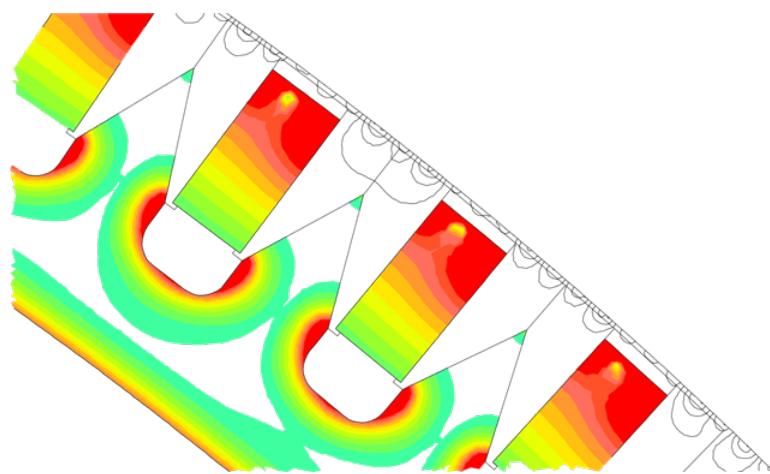
Figure 5.15: Rotor losses with AC current sheet
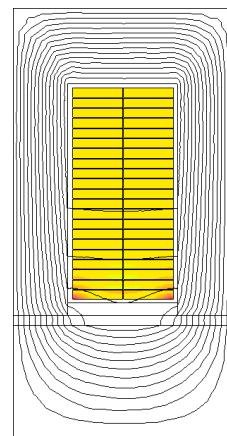
Figure 5.16: Joule losses in slot

Table 5.13: Input of the pre-sizing.

	Value
layer in winding	SL or DL
total current in slot (A)	9800
speed (r/min)	14.3
number of phases m	3
slot filling factor SL	0.77
slot filling factor DL	0.74

Results of the comparison

In Table 5.14 the preliminary results for 3MW Mono generator are listed: it is possible to evaluate the behavior of the RL index in relation to the FEM computed rotor losses, and the behavior of the electromagnetic torque in relation to the winding factor.

Table 5.14: Results of the comparison between the basic 12–10 and 12–11 configurations with single and double layer.

		12–10 SL	12–11 SL	12–10 DL	12–11 DL
Q/(mt)	shows coils distribution	4	8	4	8
Q/t	shows coils distribution	12	24	12	24
Q/(2t)	shows coils distribution	6	12	6	12
yq	slot pitch	1	1	1	1
kd	distribution factor	1	0,9659	0,9659	0,9577
kp	pitch factor	0,9659	0,9914	0,9659	0,9914
kw	winding factor kd*kp	0,9659	0,9577	0,933	0,9495
D [mm]	outer diameter	4100	4100	4100	4100
L [mm]	active lenght	1350	1350	1350	1350
Rotor Losses Index magnet		0,16	0,12	0,086	0,10
Id [A]	d-axis current	-486,24	-389,705	-486,24	-389,705
Iq [A]	q-axis current	-2757,602	-2772,892	-2757,602	-2772,892
cos ϕ		0,86	0,83	0,89	0,85
Ld [mH]	d-axis inductance	1,8	1,8	1,3	1,5
Lq [mH]	q-axis inductance	2,4	2,3	1,9	2
Tel [kNm]	load electromagnetic torque	-2481	-2470	-2371	-2432
Δ Tel [%]	torque ripple	7,457	1,933	4,783	2,181
Ploss rot [kW]	losses in rotor	37,7	41,6	25,0	35,9
Ploss mag [%]	losses in magnets	100	124	71	109
Ploss stat [kW]	losses in stator	155,2	159,5	159,0	162,3
Pout [kW]	efficiency	3558	3537	3390	3478
eta%		96,2	96,1	95,9	95,9
T el/active mass [%]		100	99	96	98

The tendency of losses in PMs does not agree with the Rotor Losses Index (RL INDEX) if SL winding is used, but it agrees with RL INDEX if DL winding is used.

The 12–10 based DL winding has the lowest losses in rotor and in PMs in accordance with the RL INDEX; The tendency of the electromagnetic torque agrees with the behavior of the winding factor kw: the lowest electromagnetic torque is developed by the 12–10 based DL winding, due to the ”poor” winding factor.

The 12–10 based SL winding results to be the best compromise between torque and losses in PMs.
Once again the trend of losses in PMs obtained with FEM in the IPM structure agrees with the prediction of the RL Index only if DL winding is considered. The INDEX appears to be a good instrument to have a fast estimation of the losses in PMs due to the harmonic content of a winding characterized by Q slots and p pole pairs. It has been shown that works properly with Halbach structure and SPM structure. If IPM structure is considered with SL winding it is necessary to consider the computed FEM losses in this study. A second series of FEM simulations is then performed to extend the range of evaluation of RL INDEX.

5.5.3. Second Finite Element Comparison

A second FEM comparison has been done. The periodicity of the winding is then chosen again according to the geometry proposed in Table 5.4. The flux concentration rotor structure has been chosen, i.e. the IPM structure E as per Table 5.8. FEM models have been realized using the same stator geometry (i.e. the number of slot Q is fixed) and changing the size of the rotor poles in order to keep the mass of PMs fixed. Other two basic windings have been added, as well as the 12–10 and 12-11 ones: the 12–13 and the 12–14 (6–7). According to the comparison in the previous section:

- the torque have been evaluated trough magnetostatic DC FEM models (Fig. 5.14);

- the losses in rotor have been evaluated trough the current sheet AC method(Fig. 5.18):

- the joule losses in the winding have been evaluated through the AC time harmonic model of the stator slot (Fig. 5.16);

- the inputs to this first FEM comparison are the same of Table 5.13.

Table 5.15: Results of the comparison between the basic 12–10, 12–11, 12–13, 12–14 with SL winding.

starting winding	12–10 SL	12–11 SL	12–13 SL	12–14 SL
RL INDEX SL	0,16	0,12	0,16	0,21
rotor magnets losses [%]	100	116	260	360
total rotor losses [kW]	24,86	26,06	46,98	63.17
losses genenerator [kW]	156,14	153,40	189,29	201,59
speed [r/min]	14,30	14,30	14,30	14,30
Torque el. [kNm]	2115	2167	2280	2320
kw	0,966	0,958	0,966	0,958
Kcr	1,26	1,25	1,22	1,21
E0 [V]	577,00	593,00	629,00	648,00
E0l [V]	522,00	541,00	572,00	582,00
Ld [mH]	1,53	1,57	1,81	1,92
Lq [mH]	2,01	1,88	1,94	2,13
V l [V]	612,10	642,00	711,00	774,00
cosphi	0,90	0,88	0,83	0,77
Pel [kW]	3166	3243	3413	3472
Torque on magnet mass [%]	100	102	108	110

In Table 5.15 the preliminary results are listed. The study is limited to SL winding. In order to establish which are the more interesting windings to be chosen for the developing of the new LW30A generator, the FEM simulated electromagnetic torque on magnet mass is considered. The stator and the mass of PMs is fixed. The machines based on 12–13 and 12–14 have the highest torque on PM mass, up to 10% more than 12–10 solution, but the winding factor does not show that difference in FEM computed torque, because it is similar for each solution. This is due to the influence of the real

geometry of the different machines, where only the stator is fixed. A verification on the same machine with different winding connection will be provided below.

This evaluation is done with the same machine and different connection of the stator winding as per figure Fig. 5.17, the structure corresponds to the Ropeways SFA motor described in Chapter 2, Connection A, and Connection B. Table 5.16 reports the
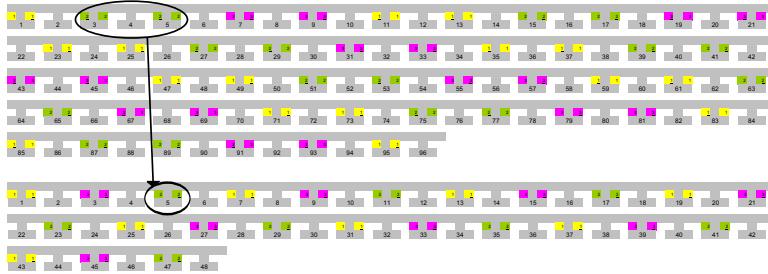
Figure 5.17: Two different connection in the same machine

electromagnetic torque and the winding factors of the fundamental: the proportion agrees with the prediction of the winding factor. The losses in PM agrees with the

Table 5.16: Electromagnetic torque (FEM) for 96 slots 80 poles motor with and without modularity

Material	Torque [kN]	kw
Connection B	220	0.84
Connection A	253	0.97
delta	+15%	+15%

trend predicted by the RL index in all the reference SL windings with the exception of the 12–10 one, this has been observed in the previous analysis also. The total amount of rotor losses in PMs corresponding to the 12–14 basic winding is almost four times the one computed for 12–10 winding. The power factor reduces if the number of poles increases. To complete the analysis on rotor losses the effect of the DL winding is introduced again and the electrical connection of the elements of the rotor structure is analyzed.

5.5.4. Analysis of the connection of the rotor

In the following Table 5.17 other preliminary results for LW30A generator are listed, fixing Q. The basic winding 12–16 (6–8) has been added. Fig. 5.18 presents the structure of the one module of the rotor. Different connections of the rotor module and different materials of the rotor yoke have been considered in the following analysis. The metal support of each magnetic element of the rotor is first considered to be electrically be electrically connected to the other like the bars of the cage of an induction motor. The yoke is removed at the beginning, then two different materials are employed: iron and aluminium. The characteristic are the same presented in Table 5.8. The metal supports of each magnetic element are then considered to be electrically insulated to each other.

Both SL and DL layer winding are employed.

Rotor losses tend to be very huge for each configuration if the rotor modules are
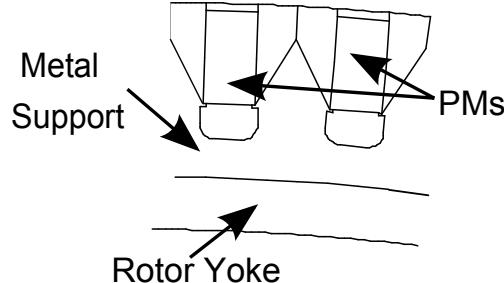
Figure 5.18: Module of the basic IPM

Table 5.17: Results of the comparison for different rotor connections.

| Basic Winding | 12–10 | 12–11 | 12–13 | 12–14 | 12–16 |
Rotor connections	(kW)	(kW)	(kW)	(kW)	(kW)
No yoke connected SL	25.2	29.0	47.4	63.8	104.7
No yoke connected DL	12.3	22.6	40.7	49.2	72.6
Al yoke connected SL	25.2	29.0	47.2	63.8	104.7
Al yoke connected DL	12.3	22.6	40.6	49.2	72.6
Al yoke not connected SL	38.5	33.4	52.8	79.3	140.3
Al yoke not connected DL	14.5	23.7	41.0	51.3	84.2
Iron yoke connected SL	25.1	28.2	47.3	64.2	103.8
Iron yoke connected DL	12.4	22.6	40.5	49.8	72.2
Iron yoke not connected SL	98.7	98.8	145.6	177.0	197.1
Iron yoke not connected DL	20.5	27.0	45.4	59.5	89.8
	(%)	(%)	(%)	(%)	(%)
Losses in PMs SL	100	138	261	360	586
Losses in PMs DL	63	119	235	295	455
			(dimensionless)		
RL Index PMs SL	0.16	0.13	0.16	0.21	0.28
RL Index PMs DL	0.086	0.10	0.13	0.16	0.24

not connected to each other. If the modules are connected there is not a significative influence of losses in the rotor yoke (it can be removed from the total amount). If the modules are disconnected the losses in the rotor tend to be extremely huge if a magnetic iron yoke is employed, especially for configurations which start from the basic windings 12–13, 12–14 and 12–16.

The losses in PMs are not affected by the connection of the rotor and they have been written in Table 5.15. This is in accordance with the behavior highlighted in section 5.2: losses in PMs are not influenced by losses in the other parts of the rotor in the model employed in the analysis.

The impact of the DL winding is very remarkable if not electrically connected modules are employed on a magnetic yoke, especially in the 12–10 winding. The main effect of the DL solution is reducing the amplitude of the subharmonics of the airgap MMF, whose impact is more evident on the metal support and the rotor yoke. The "long" wavelength let them go deeply inside the rotor structure, especially if a magnetic yoke reduces the equivalent reluctance of the interested magnetic circuit.

Once if IPM structure is considered with SL winding the INDEX of rotor losses in PMs misses the prediction: this is the only case in this study. The trend of the INDEX in any other case agree with the prediction of the FEM computation. It is then important to notice that the tendency of the INDEX considering the shifting from DL winding to SL layer winding is correct for all the windings considered.

The winding obtained from the 12–10 basic solution is the one with the lowest amount of parasitic losses for every rotor connection under study. It is also the one with the lowest amount of losses in PMs. It has been shown that fixing the stator and the mass of PMs the torque of the machine increases and so does the losses in rotor. On the contrary the power factor reduces. The basic 12–14 presents a value of the power factor which is lower than 0.8 and so it is out of specification. The machine obtained starting from the basic 12–13 winding is the better compromise for developed torque and power factor, even if losses in PMs are quite high in respect to the 12–10 solution.

5.6. Procedure for thermal analysis

In this section, the initial procedure for the thermal analysis of LW30A generator is reported. The purpose is to evaluate the impact of losses on the temperature of PMs and the electromagnetic torque of the machine. The model in Fig. 5.19 has been used.
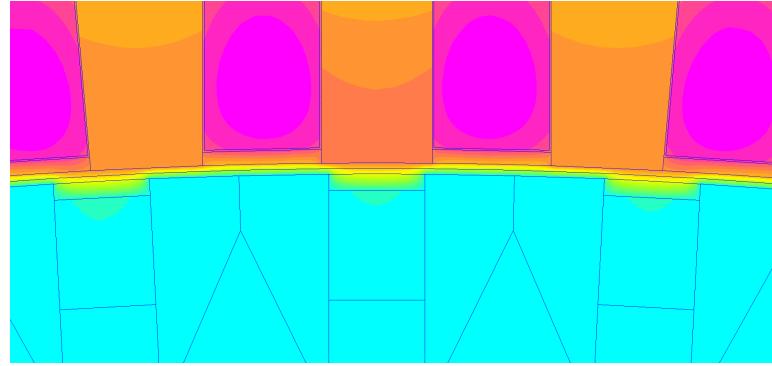
Figure 5.19: Model used for thermal simulation

While the symbols for thermal conductivities of the materials are reported in Table 5.18. Some of this values are the data input for the computation of the following

Table 5.18: Thermal conductivity of the using materials

MATERIAL	SYMBOL
Stator insulation	λ_{iso}
Varnish	λ_{Ver}
Copper	λ_{Cu}
Iron	λ_{Fe}
Aluminum	λ_{Al}
Air	λ_{air}
Magnet	λ_{mag}
Wedge	λ_{wed}

equivalent thermal conductivity. Reference can be found in [49].

Average thermal conductivity of a winding The winding is modeled like a block with a conductivity in x and y direction obtained by these formulas:

$$\lambda_{Cu-Ver,x} = \lambda_{iso} \left(\frac{b'h}{h'\delta_i} + \frac{\delta_i}{h'} \right)$$

$$\lambda_{Cu-Ver,y} = \lambda_{iso} \left(\frac{h'b}{b'\delta_i} + \frac{\delta_i}{b'} \right)$$

where b and h are the thickness and width of a single conductor without insulation, while b' and h' are the dimensions of the insulated conductor as shown in Fig. 5.20.
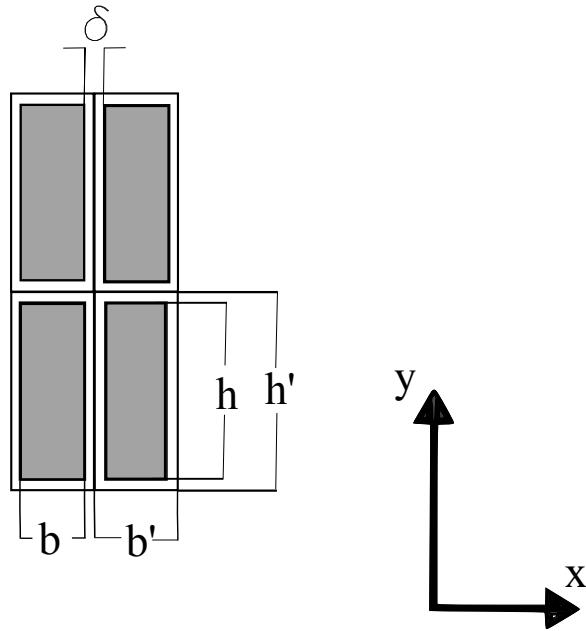
Figure 5.20: Winding made of rectangular conductors

The method validity has been verified by computing the over temperature of two slot models, with the same geometrical dimensions and same copper losses (Fig. 5.21). The simulated difference in temperature is lower than $0.5K$.
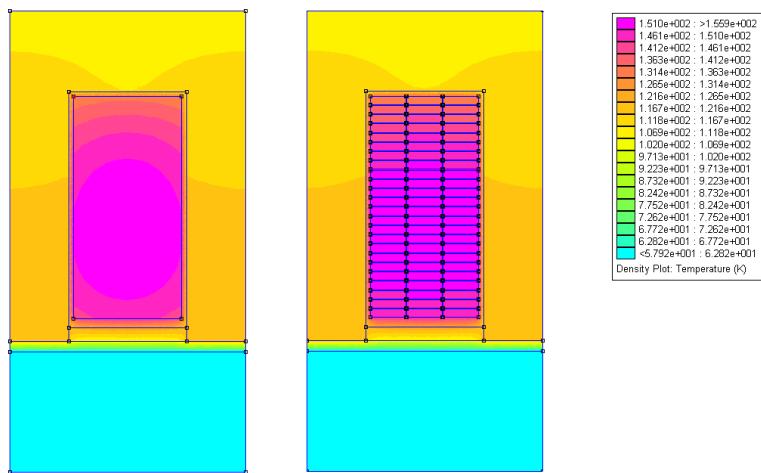
Figure 5.21: Temperature distribution in the two slot model

Air-gap in order to evaluate the convective heating transfer inside the air-gap, an

equivalent thermal conductivity is computed:

$$\lambda_{gap} = 0.0019\eta^{-2.9084}Re^{0.4614\ln(3.3361\eta)}$$

with $\eta = \frac{D_i - 2g}{D_i}$, where D_i is the stator inner diameter and g is the air-gap thickness, while $Re = \frac{vg}{\upsilon}$ is the Reynolds number where v is the relative speed between air and rotor and υ is the cinematic viscosity of the air $(1.51 \cdot 10^{-5}\ m^2/s$ @ 20 °C, ref. [50]).

5.6.1. Convection Coefficient

To calculate the convection coefficient, a natural convection into the rotor is assumed. A forced convection over the frame is supposed instead, due to the presence of the wind which moves the blades of the turbine.

Natural convection From Schuisky's book [50] for a vertical surface with H=0.5 m height and with $T_{amb} = 20C$ and $T_{surface} = 35C$, the natural convection coefficient is $\alpha_k \approx 8\ W/m^2K$ and it varies with the height as $\sqrt[4]{0.5/H}$. By imposing H=1.35 m the convection coefficient becomes $\alpha_k \approx 6\ W/m^2K$.

Forced convection From Schuisky's book the convection coefficient for air flowing along a plate is

$$\alpha = 6l^{-0.22}v^{0.78}$$

where l is the length of the plate and v the air speed; for $v = 4.5m/s$ and $l = 1.35m$ the coefficient value is $\alpha_k \approx 20\ W/m^2K$.

In Table 5.19 the convection coefficients used in the simulations are shown.
The thermal model will be used to compare the magnet temperature of two solutions

Table 5.19: Behavior of the calculated convection coefficients

	SYMBOL	VALUE [W/mK]
Outer diameter	α_{est}	60
Inner diameter	α_{int}	18

proposed for the final layout of the LW30A generator:

- the machine obtained starting from the basic 12–13 winding which is the better compromise for developed torque and power factor;

- the machine obtained from the 12–10 basic solution which is the one with the lowest amount of parasitic losses for every rotor connection. It is also the one with the lowest amount of losses in PMs.

5.7. Third FEM Comparison: configurations based on 12–10 and 12–13

The two analyzed machines have the same stator. The modules of the rotor are electrically connected to each other. The SL configuration is evaluated thanks to its easier technical feasibility. The two rotors have the same radial dimension, while the magnet for the 12–13 machine is thinner than the 12–10 poles machine due to the reduction of pole pitch. The reduction of the magnet thickness is carried out with the aim to maintain the same magnetic material for the two configurations. In the computation of the two model, the same $14.3 r/min$ mechanical speed is kept.

No-load computation

A no-load computation is performed at the beginning. The d-axis flux due to PMs is calculated, the cogging torque T_{cog} in Table 5.20 is the peak value.

The peak value of the cogging torque results to be much higher (five times) in the

Table 5.20: No load computation

	12–13	12–10
Λ_{mg} [Vs]	7.68	9.11
T_{cog} [kNm]	2.15	10.95

machine obtained with the basic 12–10 winding. This is due to the fact that the lower number of poles causes the total magnetic energy of the machine to have a remarkable variation with the position of the rotor. If the 12–10 based structure will be chosen for the final layout of the LW30A machine a strong optimization on the shape of stator teeth is required.

Load computation

To simulate the two machine at load they are fed with the same current (modulus and phase). The rotational speed $n = 14.3 r/min$ is also fixed. The load magnetic flux $\Lambda_{mg,l}$ is the d-axis flux when only a q-axis current is applied. It is worth noticing that these values are lower than in section 5.205.7. As expected the electromagnetic torque T_{em} of the machine based on 12–13 winding is +8% better than the other one, while the power factor $cos\phi$ is the lowest. It is worth noticing that the torque ripple of the 12–10 configuration is the worst: the optimization of the machine in order to reduce it is necessary. The 12–10 based machine has the highest saliency ratio: that means an higher reluctance component in electromagnetic torque.

Table 5.21: Results in load computation

	12–13	**12–10**
$\Lambda_{mg,l}$ [Vs]	7.05	8.17
T_{em} [MNm]	2.28	2.11
ΔT_{em} [%]	1.32	3.32
$cos\phi$	0.83	0.90
L_d [mH]	1.91	1.31
L_q [mH]	1.98	1.99
saliency L_q/L_d	1.04	1.52

Efficiency estimation

The computation of losses of the two machines gives the results in Table 5.22. Despite the higher electromagnetic torque developed, the 12–13 based machine winding present a lower efficiency. To recover this gap it is possible to double the electrical segmentation of PMs in order to reduce rotor losses. Results are presented in Table 5.23, the gap in efficiency of the 12–13 winding is now filled. It is worth noticing that the cost of PMs increases with that solution and that losses in 12–10 winding are still the lowest.

Another possibility is to recover the gap in torque of the 12–10 solution instead of filling

Table 5.22: Evaluation of electromagnetic power and losses

	12–13	**12–10**
P_{el} [kW]	3414	3160
P_{Cu} [kW]	90	86
P_{Fe} [kW]	27	21
P_r [kW]	47	25
η [%]	95.2	95.8

Table 5.23: Evaluation of electromagnetic power and losses, double PMs segmentation in 12–13

	12–13b	**12–10**
P_{el} [kW]	3414	3160
P_{Cu} [kW]	90	86
P_{Fe} [kW]	27	21
P_r [kW]	28	25
η [%]	95.8	95.8

the gap in efficiency of the 12–13 based machine. This has been done in Table 5.24, the electromagnetic power is now the same for both the solution. It is worth noticing

that once again the efficiency of the two solution is the same and that rotor losses in
12–10 winding are still the lowest.

Table 5.24: Evaluation of electromagnetic power and losses, increased current in 12–10

	12–13	12–10b
P_{el} [kW]	3414	3414
P_{Cu} [kW]	90	111
P_{Fe} [kW]	27	22
P_r [kW]	47	32
η [%]	95.2	95.2

Thermal analysis

The thermal model implemented is used for computing the relative rotor temperatures
of 12–13 structure in respect to the 12–10 one. The case of doubling the electrical
segmentation of PMs in 12–13b and the case of increasing the current in 12–10b are
also considered. As previously highlighted the temperature of PMs represents a critical
point to be evaluated. The temperatures for the winding and permanent magnet are
shown in Table 5.25: the relative temperature of copper in 12–10b solution is high, but
it must be related to a F class insulation at least ($\sim 150C$).

Table 5.25: Average relative temperature in PM and winding

	12–10	12–13	12–13b	12–10b
T_{wind} [K]	0	10	10	30
T_{PM} [K]	0	24	11	14

5.8. Optimization of the LW30A Generator

Guidelines to optimize of the chosen SL winding based on 12–10 structure are overview
in this section. This work is the results of an intense activity involving LTW Research
and Development department and the University of Padova.
Generally a particular care has been given to the following aspects:

- modularity of the stator (segmented in modules);

- modularity of the rotor (each rotor pole can be easy replaced);

- optimization of the shape of PMs to maximize the flux linkage (and so the torque);

- equalization of the width of the stator teeth and reduction of the cogging torque;

- reduction of the impact of holes and wedges on the magnetic circuit;

- MTPA trajectory;

- analysis of the connection of the rotor elements in order to reduce losses and choosing proper materials;

- demagnetization of PMs;

- transient study of the short circuit;

- prediction of the temperature at rated point with thermal models.

The general characteristics of Leitwind LW30 direct drive generator are listed in Table 5.26. More can be found in [4].

Both magnetostatic and transient FEM have been used to complete the study of the

Table 5.26: General Characteristics of New LW30A Generator

Generator Characteristics	Symbol	Value	Unit
Number of Slots (basic machine)	Q	12	
Number of Poles (basic machine)	$2p$	10	
Number of Phases	m	3	
Stator Outer Diameter	D_{est}	≈ 4000	mm
Rated Power	P_{gen}	3150	kW

generator. Fig. 5.8 represents the transient FEM model employed. It results to be $L_d \neq L_q$ if $\alpha_{ie} \neq 90$ $el.deg.$: an anisotropy between the direct axis and the quadrature axis is present, together with a reluctance torque component on the MTPA trajectory.
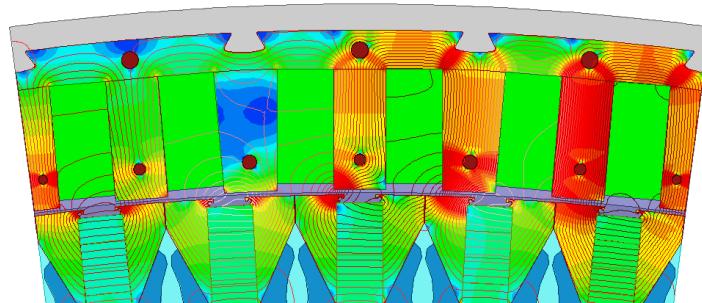
Figure 5.22: LW30A load field map

Shaping of the PMs

The principle of shaping the PM is shown in Fig. 5.23: the mass of the magnetic material is fixed. Fig. 5.24 shows the load torque versus the shape factor k_{ff}, which is the ratio between the width and the heigth of the PM.
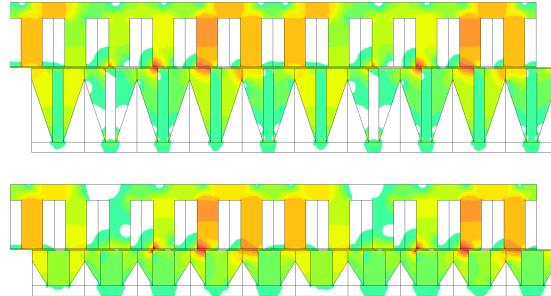
Figure 5.23: Shaping the PM
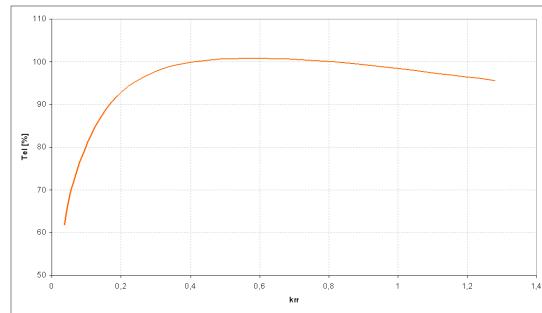
Figure 5.24: Behavior of torque with the shaping factor

Equalization of the tooth width

The equalization of the tooth width is shown in Fig. 5.25: the SL winding is realized with rectangular slot and alternate trapezoidal teeth. The width of the trapezoidal tooth is set in order to obtain a uniform distribution of the flux density.
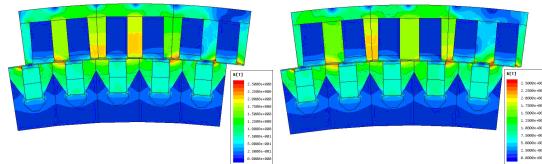
Figure 5.25: Uniforming the flux density in trapezoidal tooth

Cogging torque reduction

As a consequence of the equalization of the with of stator teeth the waveforms of the cogging torque improves. Another improvement on the cogging torque has been reached by reducing the impact of the holes on the magnetic circuit by studying their layout and size. The total effect on cogging is shown in Fig. 5.26.
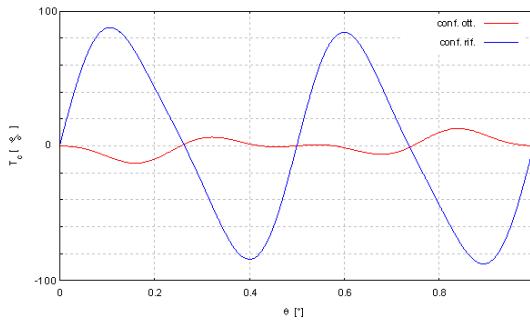
Figure 5.26: Improvement in the cogging torque waveform

Force on a rotor pole and Lorentz force on a stator coil

The study of electromagnetic forces on stator and rotor has been used for structural computation. The behavior of Lorentz force on a stator coil is shown in Fig. 5.27. It is worth noticing that in the radial direction the force generally acts in order to push the coil inside the slot. The radial and tangential force acting on one rotor poles are computed: Fig. 5.28 shows the reconstruction of the radial force.
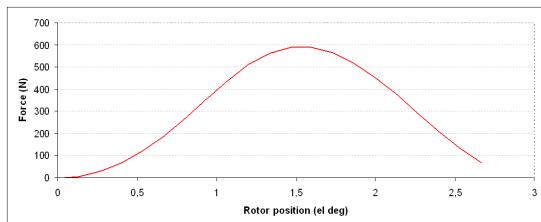
Figure 5.27: Radial Lorentz force on a coil
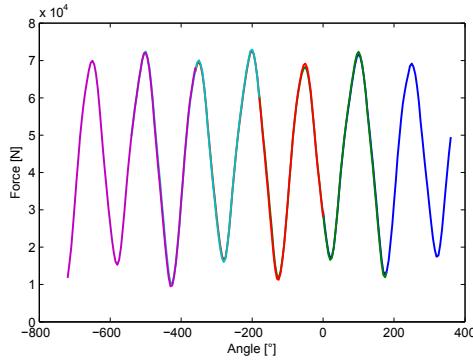
Figure 5.28: Electromagnetic radial forces on a rotor poles: reconstruction

Rotor losses comparison with transient FEM

The analysis of rotor connection has been done both with transient and AC time-harmonic FEM. The characteristic of the materials are the same presented in Table 5.8. Table 5.27 nad Table 5.28 presents the per-cent losses in each part of the rotor with the two computational method. It is worth noticing that the proportions between the two methods agree.

Table 5.27: AC losses as sum of each harmonic contribution

	$P_{Yoke}[\%]$	$P_{Al}[\%]$	$P_{PM}[\%]$	$P_{Al} + P_{Yoke}[\%]$
Al yoke connected SL	0.1	53	100	41
Al yoke isolated SL	100	100	100	100
Iron yoke connected SL	6	20	100	19
Iron yoke isolated SL	100	100	100	100

Table 5.28: Losses computed with transient FEM

	$P_{Yoke}[\%]$	$P_{Al}[\%]$	$P_{PM}[\%]$	$P_{Al} + P_{Yoke}[\%]$
Al yoke				
Connected modules	0	55	100	43
Insulated modules	100	100	100	100
Iron yoke				
Connected modules	-	-	-	18.4
Insulated modules	-	-	-	100

5.9. Building of the generator

The windings of the stator have been built and tested in the production plant of Gummidipoondi, near Chennai in India Fig. 5.29. Fig. 5.30 shows the machine during the assembling of the stator segment in Telfs (Austria).

Figure 5.29: Stator winding testing team

Figure 5.30: Assembling the stator

Test Bench Activity and Datashield

The L30A direct drive motor will be tested at B2B test bench in Telfs in the first months of 2013. The previous experience on LW15C generator and SFA motor in Chapter 2 will be the background to go on with the complete testing of the new machine.
The provisory LW30A generator Data Shield is presented in Fig. 5.9.

				LEITWIND®	
		PERMANENT MAGNETS SYNCHRONOS			
		3+3 PHASE AC GENERATOR			
		Design and patents property of Leitner			

Type:	LW30A		Serial N°		
T. BOX	kW	V	In	Hz	Conn.
1R 1S 1T	844	555	1058	14.4	Y
2R 2S 2T	844	555	1058	14.4	Y
1U 1V 1W	844	555	1058	14.4	Y
2U 2V 2W	844	555	1058	14.4	Y

cos φ:	0,83	η %:	94.3%
Inductance (q-axis): 2.34 mH		Resistance (ph/ph): 13.76 mΩ	
Inductance (d-axis): 2.00 mH			
Nominal speed:	14.4 rpm	Max speed:	19.3 rpm
DUTY S1	IP 55	Insulation class:	

Ambient operating temperature range: -20 / +40 °C

Mass:	79000 kg	YEAR/MONTH

Advanced Tecnology Worldwide

LEITNER TECHNOLOGIES

I-39049 Vipiteno - Sterzing

Figure 5.31: Data shield of LW30A generator for LTW101 wind turbine

5.10. Conclusion on slots and poles number

In 12–13 generator the torque and cogging torque improves respect to 12–10 generator. On the other hand, the power factor decreases and the rotor losses are are greater than the ones computed for 12–10 solution. As shown in the analysis of the electrical connection of the rotor elements, a perfect connection is crucial not to have a huge amount of losses. In order to maintain the losses of 12–13 structure close to 12–10 losses it is worth connecting perfectly the pole profiles and increasing the magnet segmentation.
To avoid extra cost due to segmentation of PMs as well as the risk of a not perfect rotor connection a solution based on 12–10 winding and increased stator current is then interesting. According to the analyzed thermal model the temperature of PMs in this configuration is only a bit higher in respect to the 12–13b one with extra segmentation, while it is much lower than the one computed for standard 12–13 structure.

Chapter 6

The Switching-Flux Permanent Magnet Machine

Switching Flux Permanent Magnet machines compared with Interior Permanent Magnet machines are presented to be interesting solutions in terms of torque per volume density, compactness, active material layout and cooling capability. The flux linkage results to be bi-directional and voltage is almost sinusoidal. These machines are then interesting for AC drives and field weakening operation.
Employing low cost magnet material must be carefully evaluated despite of the lack of torque capability adopting rare earths permanent magnet can be recovered with cost saving.
The aim of this chapter is to clarify the behavior of Switching Flux PM Machine in respect to Fractional Slot Machines, considering different rotor topologies. Small Motors are chosen to carry on the analysis.

6.1. Introduction

PERMANENT magnet (PM) machines are largely used in industrial drives, electrical vehicle applications and generation systems based on renewable energy such as wind and wave energy systems. The recent instability of rare earth PMs prices forced the electrical machines designers to focus on low cost solutions [51, 52].

The switching flux PM machines (SFPM) are presented to be interesting alternatives to the more used surface permanent magnet (SPM) and interior permanent magnet (IPM) machines [53, 54]. They give the possibility to pack the magnet material directly on the armature part, resulting a robust structure. It is also possible to cool the active material easier, because it is on the stator. An analysis of the performance with a different number of slots and rotor poles is shown in [55]. The performance of all- and alternate-poles windings are studied in [56].

The structure of the moving part of SFPM machine is simple and robust due to the possibility to built the rotor with iron only, as in switched reluctance machines. Examples for wave energy generator and tubular machine are given in [57, 58]. A

151

vehicle propulsion system which use the same priciple is presented in [59]. Another interesting field of application is the aerospace one, thanks to the high compactness of the flux switching solution [60]. The SFPM machine can reach performance similar to that of the fractional slot permanent magnet machine: a comparative study between a SFPM machine and an IPM machine can be found in [61], considering distribute winding IPM machine for automotive field. Machines for electrical vehicles are then presented and studied in [62, 63]. Another comparison between SFPM machine and SPM machine regarding aerospace application is available in [64], while an high speed application is presented in [65].

The flux linkage of SFPM machine is bi-directional and voltage is almost sinusoidal: the machine is then interesting for AC drives and field weakening (FW) operation. Examples are available in [35, 66].

This paper compares the capabilities of several PM machines with different topologies:

- The SFPM machine;

- The SPM machine, radially magnetized PMs;

- The IPM machine, radially magnetized PMs;

- The IPM machine with flux concentration, tangentially magnetized PMs (IPM2);

- The IPM machine with V shape PMs (VIPM).

All these machines have fixed outer diameter and fractional slot winding, the stack length of the compared structure is adjusted in order to have the same torque. The aim of the study is to compare the torque density, referred to magnet material mass and to the whole volume.

Rare earth PMs are employed at the beginning. Low cost ferrite PMs are then employed to investigate their cost respect to the machine performance. The possibility to integrate a huge magnet quantity in the armature of the SFPM machine and the flux concentration principle can lead to a cost effective solution which must be carefully evaluated without considering the performance of the machine only. In addition, further capabilities will be compared, including the robustness against PMs demagnetization.

6.2. Description of the considered machines

The PM machines under comparison have been chosen with the same stator outer diameter of a SPM and IPM machines assumed as reference case. Such machines have been analyzed in literature where classical single layer and double layer three-phase windings have been considered in comparison to the fault-tolerant six-phase winding. Experimental results have confirmed that finite elements analysis is suitable for estimating the motor performance and that those machines are well-known by the authors [67–70]. Therefore, the agreements between experimental results and predictions reinforce the confidence in the results of the following analysis. The number of slots is Q=12 and the number of poles is $2p$=10. The winding is a 2-layer fractional slot winding. Fig. 6.1 shows the SPM machine and the IPM machine [71].
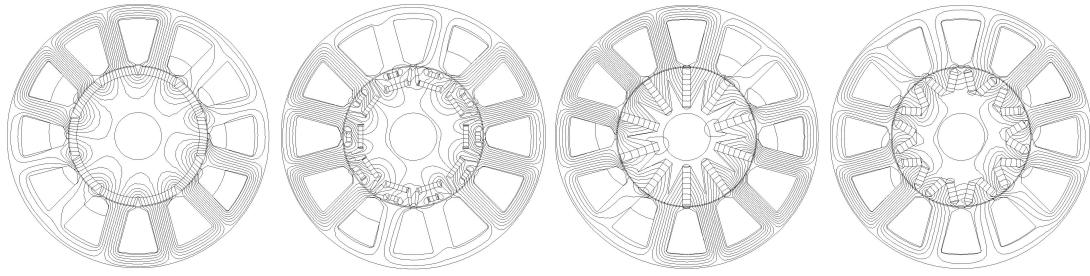
Figure 6.1: Field lines of SPM, IPM, IPM2 and VIPM2 configurations under load

In this first comparison the active volume of all the machines considered is almost the same, because both the outer diameter and the stack length are maintained constant. The stator is fixed in this study. Two other rotor types are designed, using the same PM material mass employed in SPM machine: the IPM2 machine and the VIPM machine. Fig. 6.1 shows these two machines as well. Table 7.2 summarizes the main characteristics of the fixed stator together with the permanent magnet mass in the rotor. The stack length is 90 mm for all the machines;

Table 6.1: geometry of PM motors

Quantity		Value
Stator outer diameter	(mm)	134
Stator inner diameter	(mm)	71.5
Stack length	(mm)	90
Split ratio	–	0.54
Stator tooth width	(mm)	10.5
Stator tooth height	(mm)	23.25
Slot fill factor	–	0.4
Airgap thickness	(mm)	0.4
Rotor permanent magnet mass IPM	(kg)	0.27
Rotor permanent magnet mass IPM2, SPM, VIPM	(kg)	0.55

Fig. 6.2 shows the SFPM machine and Table 7.3 summarizes its main characteristics. Stator outer and inner diameter, stack length and airgap thickness are the same of the other motors of Fig. 6.1.

In addition the following assumptions are made:

- Iron lamination is employed in both stator and rotor;

- Rare earth PMs have 0.97 T remanence and 1.06 relative permeability;

- Rare earth PMs density is 7600 kg/m^3;

- The nominal slot current is 1665 A (peak). That corresponds to about 9 A/mm^2 (rms) in the conductors;
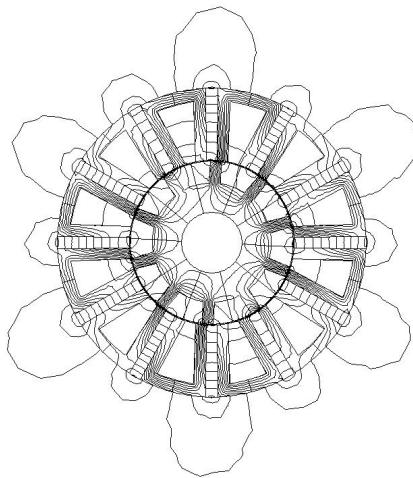
Figure 6.2: SFPM machine and flux lines under load

Table 6.2: geometry of the SFPM machine

Quantity		Value
Stator outer diameter	(mm)	134
Stator inner diameter	(mm)	71.5
Airgap thickness	(mm)	0.4
Rotor tooth width	(mm)	4.62
Rotor tooth height	(mm)	9.6
Stator tooth width	(mm)	4.67
Stator tooth height	(mm)	26
Stator slot opening	(mm)	4.68
Magnet width	(mm)	4.68
Magnet height	(mm)	31.28
Stack length	(mm)	90
Magnet mass	(kg)	1.29

- The equivalent number of series turn per phase is 118.

6.3. Results of the comparison

6.3.1. Nominal torque comparison

The PM machines presented above have been analyzed using 2D finite elements. Each operating point is obtained by performing a simulation over the whole electrical period. The first step of the study is to compare the rated torque of the different machines, which work as motors and controlled according to the Maximum Torque Per Ampere (MTPA) strategy: the angle of the stator current vector α_{ie} is changed, till the maxi-

mum torque is reached. Fig. 6.3(a) shows the torque versus rotor position of the SPM machine when only q-axis current is supplied (i.e. with α_{ie}=90 deg). The average torque is 30.4 Nm, the torque ripple is 1.6%. Fig. 6.3(b) shows the torque behavior of the SFPM machine: the current angle to get the maximum torque is α_{ie}=105 deg. The average torque is 30.8 Nm and the torque ripple is 5.6%, higher than in SPM machine. Fig. 6.4 presents the IPM2 machine and VIPM machine torque behavior. The current angles to get the maximum torque are α_{ie}=110 deg and α_{ie}=120 deg respectively. The average torques are 39.4 Nm and 30.6 Nm respectively, while the torque ripple are 2.5% and 4%.
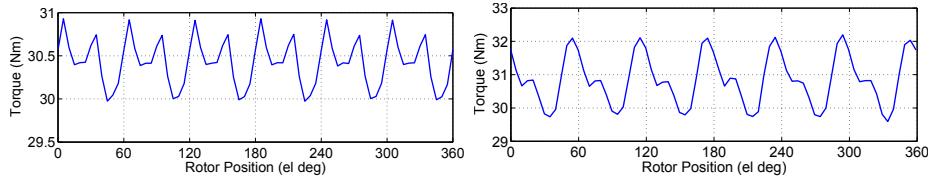
Figure 6.3: Torque behavior versus rotor position
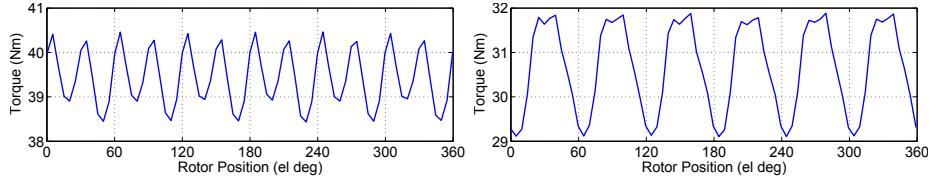
Figure 6.4: Torque behavior versus rotor position

Table 6.3: Results of the comparison for torque (Rare Earth PMs)

Quantity		SFPM	IPM	IPM2	SPM	VIPM
Torque	(Nm)	30.8	15.7	39.4	30.4	30.6
Torque ripple	(%)	5.6	6.4	2.5	1.6	4.0
MTPA α_{ie}	(deg)	105	130	110	90	120
PM mass	(kg)	1.29	0.27	0.55	0.55	0.55
PM Volume	(%)	100	21	43	43	43
Torque/PM mass	($\frac{Nm}{kg}$)	24	58	72	55.3	55.6
Torque/PM mass	(%)	100	241	300	230	232

The results of the torque comparison are summarized in Table 6.3. by the SPM and VIPM machines. The IPM2 machine develops the highest torque, thanks to the flux concentration. The IPM machine has the lowest torque, which is almost half the torque of the SPM machine, mainly due to the reduced PM mass. This motor has been designed to satisfy some given fault tolerant capabilities [67]. SFPM machine exhibits the lowest torque to PM mass ratio, resulting less than half than the SPM machine. The torque ripple of the SFPM machine is almost three times the ripple of the SPM machine and twice the ripple of the IPM2 machine. The IPM and VIPM machines have a similar torque ripple compared to SFPM machine. In order to develop almost the same torque (i.e. 30.8 Nm) the stack length of each machine could be rearranged.

SPM, SFPM and VIPM machines do not need any adjustment. The stack length of the IPM machine must be almost double.

The demagnetization behavior of the analyzed motors must be carefully evaluated. The flux density plot of the IPM, IPM2, SPM and VPIM motors are shown in Fig. 6.5. In addition, some lines are highlighted along which the normal component of the magnetic flux density is monitored. These lines lay on the portion of the PMs which presents the lowest flux density.
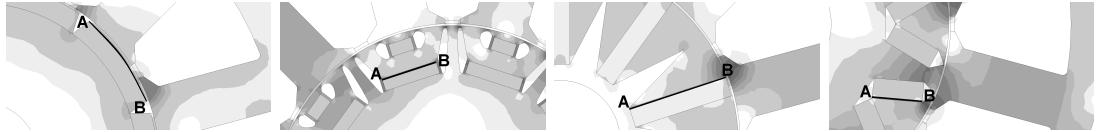
Figure 6.5: Flux density map and selection of the monitoring lines on SPM, IPM, IPM2 and VIPM2 Permanent Magnets

Using rare earths PMs high intrinsic coercive force can be assumed (e.g. referring to average quality NdFeB PM it is about 1300 kA/m at 20°C temperature). However, it reduces to about 450 kA/m at operating temperature 130°C. The following condition represents a safety limit of the flux density normal to the line in PMs, that can be expressed as:

$$B_n > 0.4 \ T \tag{6.1}$$

Fig. 6.6 shows the behavior of the normal component of the flux density on the lines in Fig. 6.5 for IPM, IPM2 SPM and VIPM machines.
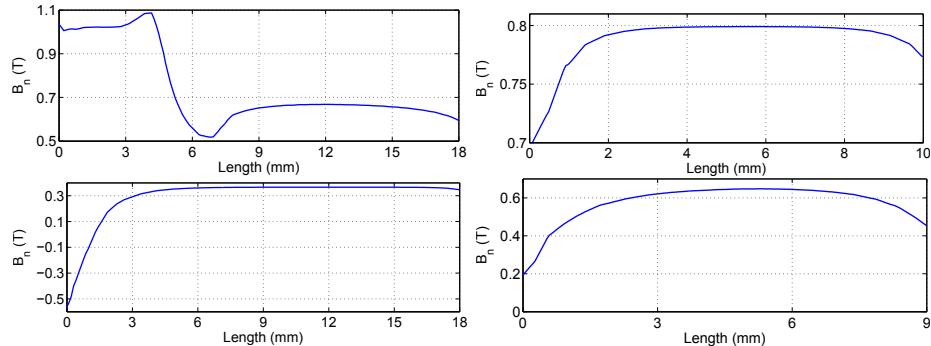
Figure 6.6: Flux density on the monitoring lines of SPM, IPM, IPM2 and VIPM2 Permanent Magnets

The SPM machine presents a good demagnetization resistance and the flux density is always greater than 0.5 T. The IPM machine presents the best demagnetization resistance, being the flux density in PMs always greater than 0.7 T. The IPM2 machine presents the worst demagnetization resistance: the lowest normal flux density drops down to -0.55 T in some portion of the magnet. This means that a part of the PM results to be demagnetized. The VIPM machine is slightly critical: the lowest value of the flux density is 0.2 T in some portion of the magnet.

Fig. 6.7 shows the behavior of the flux density in the PMs of the SFPM machine. The normal component to the line results always lower than 0.4 T along the whole monitoring line and drops down to -0.5 T.
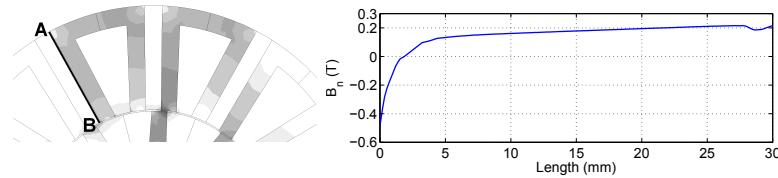
Figure 6.7: Selection of the monitoring line on SFPM Permanent Magnets

If rare earth PMs motors are considered, the machines which employ the flux concentration (e.g. IPM2, SFPM machines) have the worst demagnetization behavior. The magnets of the considered IPM2 machine and SFPM machine are completely demagnetized even under nominal load if average quality NdFeB is employed. To completely avoid that phenomenon a higher grade NdFeB magnet or SmCo, which exhibits the knee of the B-H curve in the third quadrant (i.e. a very high coercive force) must be used. The IPM machine and SPM machine are safe and can work without any demagnetization risk. The IPM machine is the configuration with the best demagnetization resistance. The magnets of the VIPM machine result to be partially demagnetized.

6.3.2. Employing of ferrite PMs

A further comparison is carried out to evaluate the ferrite magnets instead of rare earth ones. The previous analysis is repeated by replacing magnet materials but keeping the same geometries (Table 7.2-7.3). Each machine is labeled as follows:

- SFPMfe is SFPM machine with ferrite PMs;

- SPMfe is SPM machine with ferrite PMs;

- IPMfe is IPM machine with ferrite PMs;

- IPM2fe is IPM2 machine with ferrite PMs;

- VIPMfe is VIPM machine with ferrite PMs;

Table 6.4 reports results for torque comparison. The SFPM machine with rare earth magnets of Table 6.3 has been considered as reference machine.

Ferrite PMs have 0.4 T remanence and 1.06 relative permeability and mass density equal to 5000 kg/m^3. They have low intrinsic coercive force which is about 250-300 kA/m even at 20°C, according to [72], and the risk of demagnetization is high. It is worth noticing that the ferrite PMs have a stable demagnetization behavior in temperature, so the temperature of PMs is fixed at 20°C. The following condition represents a safety limit of the flux density in PMs:

Table 6.4: Results of the comparison for torque, ref. SFPM machine (Ferrite PMs)

Quantity		SFPMfe	IPMfe	IPM2fe	SPMfe	VIPMfe
Torque	(Nm)	20.9	10.3	20.7	13.0	17.6
Torque ripple	(%)	2.5	9.7	6.5	7.7	11
MTPA α_{ie}	(deg)	80	130	120	90	130
PM Volume	(%)	100	210	43	43	43
Torque/PM mass	$(\frac{\text{Nm}}{\text{kg}})$	24.9	38.0	37.0	23.6	32.0
Torque/PM mass	(%)	104	158	154	98	134

$$B_n > 0.1 \ T \tag{6.2}$$

Of course the nominal torque of each machine with ferrite PMs falls down, in comparison with the original rare earth machines. The torque of the SPMfe machine collapses respect to the SPM machine, with a -57% drop. This is expected since all the torque of SPM machine depends on the PM flux. The torque of the IPMfe machine is lower respect to the IPM machine, but with a -35% drop, thanks to the reluctance torque component. The IPM2fe machine compared to the IPM2 machine exhibits a -50% lack of torque. The VIPMfe machine compared to the VIPM machine has a similar behavior with a -40% drop in torque. The lack of torque of the SFPMfe machine respect to the SFPM machine is -32%: this machine behaves then like IPM machine, but it has not a significant reluctance torque component. This quite low lack of performance in SFPM structure is due to the big magnet mass integrated in stator teeth and the flux concentration.

It is worth noticing that the torque ripple of each machines increases after replacing rare earths PMs with ferrite PMs. The only exception is the torque ripple of SFPMfe machine: it drops from 5.6% down to 2.5%.

Further study of IPM machine with different magnet materials is also reported in [73].

In order to evaluate the demagnetization risk Fig. 6.8 shows the behavior of the normal component of the flux density along the monitoring lines for IPMfe, IPM2fe SPMfe and VIPMfe machines.

The SPMfe machine is slightly critical: the lowest value of the flux density is 0.05 T in some portion of the magnet. The IPMfe machine presents the best demagnetization resistance, being the flux density in PMs always greater than 0.19 T. The IPM2fe machine presents the worst demagnetization resistance: the lowest value of the flux density drops down to -0.6 T in some portion of the magnet. The VIPMfe machine is very critical: the lowest value of the flux density is -0.15 T in large portions of the magnet. Fig. 6.9 shows the behavior of the flux density on the PMs of the SFPMfe machine. The value of the normal component is lower than 0.1 T along the whole line and drops down to -0.5 T.
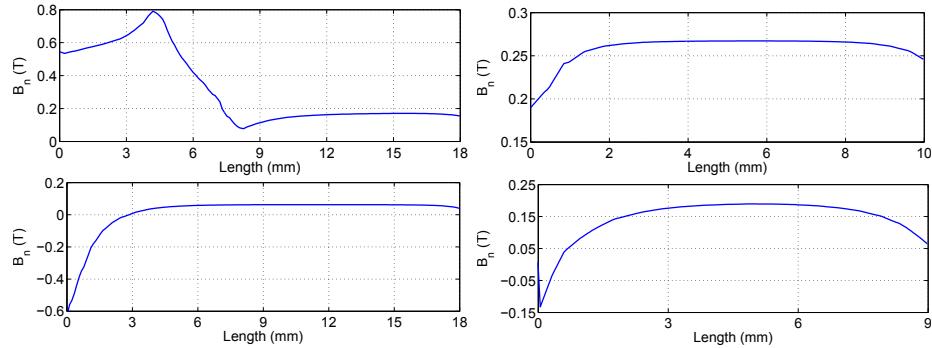
Figure 6.8: Flux density on the monitoring lines of SPMfe, IPMfe, IPM2fe and VIPM2fe Permanent Magnets

The employing of ferrite PMs must be carefully evaluated. The machines which employ flux concentration (e.g. IPM2fe, SFPMfe machines) have the worst demagnetization behavior. They cannot work with average quality ferrite keeping the same geometry of the related rare earth machine. A redesign of the magnetic circuit is required to avoid this risk. The magnets of the VIPMfe and SPMfe machines result to be partially demagnetized. Once again the IPMfe machine is the configuration with the better demagnetization resistance and works properly even with ferrite PMs.
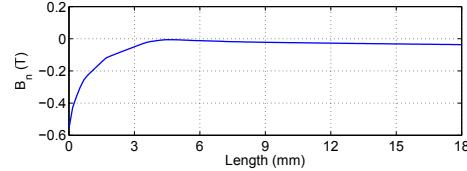
Figure 6.9: Flux density on the monitoring lines of SFPMfe

The impact of demagnetization is summarized in Table 6.5, considering the standard magnet characteristics presented in Section 6.3.1 and 7.3.2. The adjusted stack length for each machine is presented as well.

Table 6.5: Results of the comparison for cost at fixed rated torque

Quantity		SFPM	SFPMfe	IPM	IPMfe	IPM2	IPM2fe	SPM	SPMfe	VIPM	VIPMfe
Torque	(Nm)	30.8	30.8	30.8	30.8	30.8	30.8	30.4	30.8	30.6	30.8
Stack length	(mm)	90	133	177	270	70	134	90	214	90	158
Slot volume	(dm^3)	0.29	0.43	0.71	1.08	0.28	0.54	0.36	0.85	0.36	0.63
Copper volume	(dm^3)	0.12	0.17	0.28	0.43	0.11	0.21	0.14	0.34	0.14	0.25
Stator iron volume	(dm^3)	0.62	0.91	1.07	1.63	0.43	0.81	0.54	1.29	0.54	0.95
Rotor iron volume	(dm^3)	0.18	0.27	0.48	0.74	0.14	0.26	0.24	0.56	0.23	0.40
Magnet volume	(dm^3)	0.17	0.25	0.07	0.11	0.06	0.11	0.07	0.17	0.07	0.13
Active volume	(dm^3)	1.08	1.60	1.91	2.91	0.73	1.40	1.00	2.36	0.99	1.73
Copper mass	(kg)	1.04	1.54	2.52	3.84	1.00	1.91	1.28	3.04	1.28	2.24
Stator iron mass	(kg)	4.80	7.08	8.37	12.74	3.32	6.33	4.25	10.08	4.25	7.44
Rotor iron mass	(kg)	1.42	2.09	3.77	5.73	1.07	2.05	1.85	4.39	1.77	3.10
Magnet mass	(kg)	1.29	1.25	0.53	0.53	0.43	0.54	0.54	0.84	0.55	0.63
Active mass	(kg)	8.54	11.96	15.19	22.85	5.83	10.82	7.91	18.34	7.84	13.41
Copper cost	(USD)	11.7	17.2	28.3	43.0	11.2	21.4	14.3	34.0	14.3	25.1
Stator iron cost	(USD)	10.6	15.6	18.4	28.0	7.3	13.9	9.3	22.2	9.3	16.4
Rotor iron cost	(USD)	3.1	4.6	8.3	12.6	2.4	4.5	4.1	9.7	3.9	6.8
Magnet cost	(USD)	77.2	12.5	31.9	5.3	25.7	5.4	32.4	8.4	32.8	6.3
Active cost	(USD)	102.6	49.9	86.9	89.0	46.6	45.2	60.1	74.3	60.4	54.6
Torque/active volume	(Nm/dm^3)	28.5	19.3	16.2	10.6	42.1	22.1	30.5	13.0	31.0	17.8
Torque/active mass	(Nm/kg)	3.6	2.6	2.0	1.3	5.3	2.9	3.8	1.7	3.9	2.3
Torque/active cost	(Nm/USD)	0.30	0.62	0.36	0.35	0.66	0.68	0.51	0.42	0.51	0.56
Active cost/torque	(USD/Nm)	3.3	1.6	2.8	2.9	1.5	1.5	2.0	2.4	2.0	1.8
Lowest B_n on PMs	(T)	-0.5	-0.5	0.7	0.19	-0.55	-0.6	0.5	0.05	0.2	-0.15
Whole magnet resists demagnetization?	risk	no	yes	yes	risk	no	yes	no	risk	no	

6.3.3. Cost Comparison

The study deals with cost estimation of the active material to evaluate the compared machines in term of USD/kg, both for rare earth and ferrite PMs, considering the standard magnet characteristics presented in Section 6.3.1 and 7.3.2. Following quotations are considered, starting from literature [46, 47]:

- Cost of NdFeB PMs average grade: 60 USD/kg;

- Cost of ferrite PMs: 10 USD/kg;

- Cost of copper: 11.2 USD/kg;

- Cost of iron lamination: 2.2 USD/kg;

The active length of each machine is adjusted so as they develop about the same rated torque (i.e. 30.8 Nm). The length (and so the active volume) of the machines is increased with the aim to investigate their economical convenience. The results of the cost comparison are shown in Table 6.5. It results:

- There is no economical convenience if ferrite PMs are employed in SPM structure, without acting on machine geometry, because the cost per torque increases from 2 USD/Nm up to 2.4 USD/Nm. The SPMfe structure with ferrite PM is affected by partial demagnetization;

- Referring to the IPM and IPM2 structures, the economical impact is almost the same if rare earths or ferrite PMs are employed. Otherwise IPM2 machine requires higher grade rare earth magnets (not quoted) and cannot work with ferrite magnets if the geometry is not modified;

- It could seem there is a big convenience in employing ferrite with SFPM structure, because the cost per torque drops from 3.3 USD/Nm down to 1.6 USD/Nm. Otherwise such a structure cannot work with standard ferrite magnets due to demagnetization limits;

- VIPMfe machine is a bit cost effective with a cost per torque drop from 2.0 USD/Nm down to 1.8 USD/Nm. Moreover, also this structure is affected by partial demagnetization.

6.3.4. Field weakening capability

The last part of this analysis ends with the evaluation of the FW capability of the considered topologies. The comparison is referred to the following data:

- the base torque 30.8 Nm;

- the base speed is fixed to 1000 r/min;

- the inverter current limit is 14 A;

- the inverter voltage limit allows each machine to run at 1000 r/min.

The drive speed increases and current angle moves from the MTPA point in order to maintain the inverter phase voltage. The mechanical limit for speed is fixed to 6700 r/min. The reference value for constant power region is 6.7 kW at least, which corresponds to the VIPM machine behavior. The shape of torque and power characteristics of SFPM, IPM, IPM2, SPM and VIPM machines are shown in Fig. 6.10. Fig. 6.10 (a) presents the behavior of torque vs speed, while Fig. 6.10 (b) presents the behavior of power vs speed.
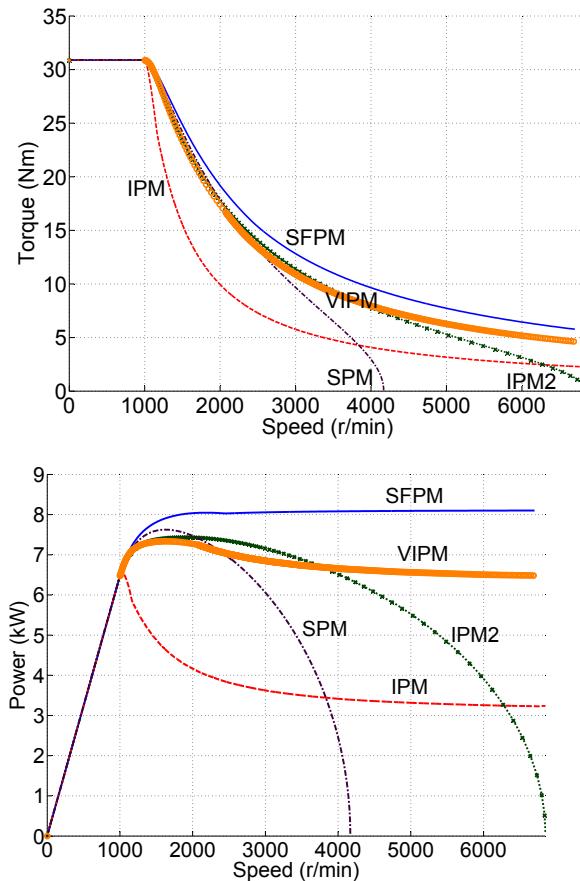

Figure 6.10: Mechanical output of NdFeB considering FW control

Fig. 6.11 presents the trajectory of the current vector on the $Id - Iq$ plane. It is worth noticing that SFPM and VIPM machines can guarantee a wide constant power region,while SPM and IPM2 machines collapse. The SFPM machine can provide an higher maximum power respect to the VIPM machine. The SFPM machine seems then a good candidate for AC drives. The IPM machine has a wide constant power region as well, but it exhibits a lower power (almost 4 kW). A summary of the FW control is presented in Table 6.6.
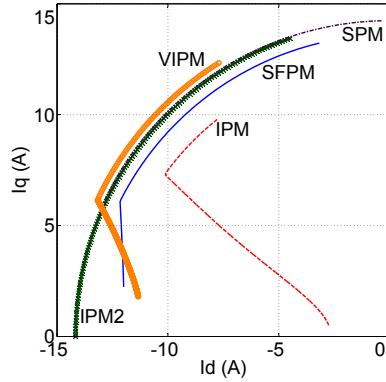
Figure 6.11: Trajectory of the current vectors

Table 6.6: Results of the comparison for FW

Quantity	SFPM	IPM	IPM2	SPM	VIPM
Constant power region width (p.u.)	6.7	—	3.7	2.6	6.7
Max power value (kW)	8.1	6.6	7.4	7.63	7.33
Flux linkage phase (mVs)	213	397	422	344	365
Flux linkage with 0 d-axis flux (mVs)	116	431	—	—	172
Torque with 0 d axis flux (Nm)	20.6	13.6	—	—	16.1

It is worth noticing that in SPM and IPM2 machines the magnet flux in d-axis does not become completely equal to zero. On the other hand, the magnet flux become zero in SFPM, IPM and VIPM machines: that means they can be driven in a large constant power region beyond the rated speed.

6.4. Final considerations

In this chapter different topologies of PM machines have been compared. Torque production, active material cost and demagnetization behavior and field weakening capability have been considered. Both rare earths and low cost PMs (ferrite) have been investigated.

The IPM2 machine with flux concentration results to have the best torque on active material mass. On the other hand, it is very sensitive to demagnetization of PMs.

The SFPM machine with rare earths PMs exhibits almost the same capabilities than SPM and VIPM machines in term of torque per active mass: however it results to be expensive, due to the high amount of magnet employed. The demagnetization behavior is critic and the employment of high-grade NdFeB or SmCo is required. The field

weakening capability of SFPM machine results to be slightly better than the other IPM machines under analysis.

VIPM machine is only partially demagnetized at nominal load, while the IPM machine has the best demagnetization resistance. Employing of ferrite PMs has to be carefully evaluated: the magnets of the VIPMfe and SPMfe machines result to be partially demagnetized. On the contrary, the IPMfe machine can work without any demagnetization risk even with ferrite.

SFPMfe machine seems to be an interesting solution: the active material cost is almost the lowest in respect to the other machines under study. However. it has been found that machines which employ the flux concentration principle (e.g. IPM2fe, SFPMfe machines) have the worst demagnetization behavior. They cannot work with average quality ferrite PMs due to demagnetization problems. A complete re-design of the geometry is required.

Chapter 7

Linear Drive Modules For Wave Energy Conversion

Permanent Magnets Linear Generators can be designed adopting different topologies. They are used according to the constrains required by the application. In this chapter different linear generator topologies for Wave Energy Conversion are compared. Different geometries are chosen in the armature and the magnetizing parts, including the switching flux permanent magnet machine.
The switching flux structure results to be cost effective if ferrite permanent magnets are employed, but the impact of demagnetization must be carefully evaluated.
A solution with double sided translator is finally considered.

7.1. Introduction

WAVE energy conversion has grown more and more in the renewable energy research scenario during the last ten years. The strong development of wind power and the requirement for off shore application is encouraging the new interesting in the ocean wave energy extraction field [74, 75]. From the generator point of view a very interesting typology is the direct drive linear one with permanent magnets: no brushes and erasing of the gearboxes to the essential requirements in order to reduce maintenance, which is very expensive in the sea environment. The family of the permanent magnet (PM) linear generators comprises three main assembly topologies: the cylindrical (or tubular) one, the U-channel shape and the flat type one. The latter includes the ironless , the slotless and the slotted iron configurations. A complete introduction is provided in [76], while analytical and numerical techniques to study and design linear PM generator are given in [77–79]. The example of a tubular structure is developed in [58].

The different topologies are developed according to the constrains imposed by the particular technical application, considering the required airgap flux density, the forces acting on the mechanical structure of the translator and the target circuital features. In particular the requirements for linear generators for direct drive wave energy conversion are high thrust and low speed [80]. The Archimede Wave Swing (AWS) and the

Table 7.1: Rough numbers characterizing a linear generator for a wave energy converter

Symbol	Description	Unit	Value
τ_{pk}	Thrust (peak)	MNm	1
v_p	Max Speed	m/s	2.2
P_{ave}	Average power	MW	1
g	Airgap thickness	mm	5
Ov	overlength	$\%$	+60

Inertial Sea Wave Energy Converter (ISWEC) are examples of PM linear direct drive generator for wave energy conversion [81–84].

In the State of Oregon (US), direct drive tubular solution for ocean power utilization is under development [85]. Another example of linear generator applied to wave energy (not with PMs) have been developed by J.Vining [86]. Several configurations have been presented in [87]. The employing of linear switching flux permanent magnet (SFPM) generator coupled with a buoy is proposed in [57]. The simplicity of the structure of the mover (iron only like in reluctance machines) could lead to a better dynamic behavior. The switching flux configuration has been also proposed for the "pendulum" machine within the SEAQUEST project [88]:the pre–design of an arch–shaped direct drive wave generator is developed basing on a structure with 12 stator slots and 14 rotor teeth [89, 90].

In Table 7.1 Rough numbers characterizing a direct drive PM linear generator for wave energy extraction are presented, starting from [80]. The overlength Ov is the length of the mover (or armature) which exceeds the armature (or the mover) length.

Some topologies are analyzed with a two dimensional finite element (FE) approach considering the presence of an armature part, including a three–phase winding, an airgap, and a magnetizing part with permanent magnets, which can be surface mounted or buried in the iron. For the sake of generality, the length of the module is considered to be 1 m for all configurations. Similarly, the width of the model is fixed equal to 0.4 m, the height of the linear motor is 0.25 m and the airgap thickness is 5 mm for all configurations. A sketch is reported in Fig. 7.1, referring to the basic structure with surface mounted PMs (SPM).
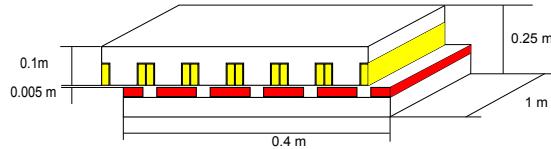

Figure 7.1: Reference geometry of a linear generator module

Two topologies are then added to the study:

• The SFPM machine;

- The IPM machine with flux concentration, tangentially magnetized PMs (IPM).

The IPM and SPM have fixed armature part and fractional slot winding, the aim of the study is to compare the thrust density, referred to magnet material mass and to the whole active mass.

Rare earth PMs are employed at the beginning. Low cost ferrite PMs are then employed to investigate their cost respect to the machine performance. The possibility to integrate a huge magnet quantity in the armature of the SFPM machine and the flux concentration principle can lead to a cost effective solution which must be carefully evaluated without considering the performance of the machine only. The robustness against PMs demagnetization is a crucial point to investigate. In order to increase the thrust density the possibility of employing a double-sided structure is analyzed. The impact of the studied modules is finally evaluated on a wave energy conversion system, whose parameters come from literature [91,91].

7.2. Description of the linear modules under study

The PM machines under comparison have been chosen with the same armature part, the number of slots of the basic module is $Q=12$ and the number of poles is $2p=10$. The winding is a single layer (SL) fractional slot winding. Fig. 7.2 shows the SPM machine and the IPM generator modules.
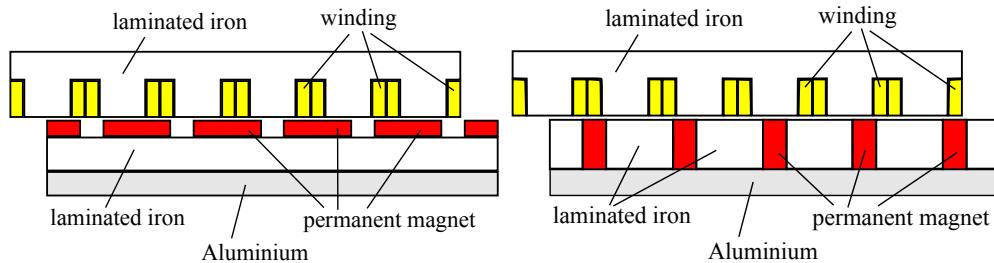
Figure 7.2: Linear generators: SPM module and IPM module.

In this first comparison the active volume of all the machines considered is almost the same, because both the outer armature part and the mass of PMs are kept constant. Table 7.2 summarizes the main characteristics of the fixed stator together with the permanent magnet mass in the rotor. The stack length is 200 mm for all the modules;

The working principle of the SFPM module differs from traditional fractional slot winding module in the sign of the flux linkage: if the SPM (or IPM) topology is considered the sign of the flux linkage Ψ remains the same while the PM is moving under an armature coil. In the SFPM topology the sign of the flux "switches" and changes its sign while a tooth of the translator is moving under an armature coil. Fig. 7.3 shows the SFPM machine and Table 7.3 summarizes its main characteristics. Stator thickness, stack length and airgap thickness are the same of the other modules of Fig. 7.2. The number of stator slots is still $Q=12$ and the number of the translator teeth is equal to the number of poles is $2p=10$ of SPM and IPM modules. PMs are

Table 7.2: geometry of SPM and IPM modules

Quantity		Value
Stator thickness	(mm)	90
Stack length	(mm)	200
Stator tooth width	(mm)	35
Stator tooth height	(mm)	80
Slot fill factor	–	0.8
Airgap thickness	(mm)	5
Permanent magnet mass	(kg)	~ 50

placed in the armature part together with the winding. It is clear that the FSPM machine working frequency is double the one of SPM and IPM machines.
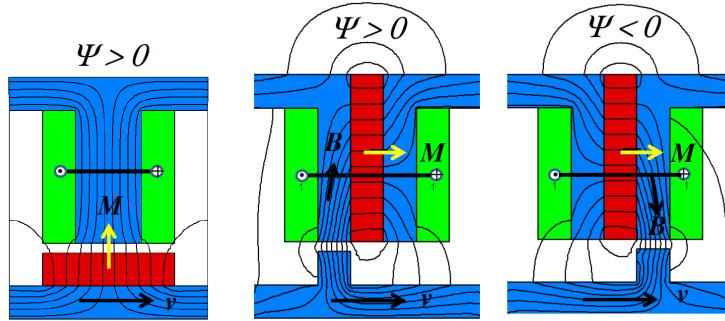
Figure 7.3: SFPM machine working principle: difference in respect to SPM (courtesy of K.Reichert)

Table 7.3: geometry of the SFPM module

Quantity		Value
Stator thickness	(mm)	90
Airgap thickness	(mm)	5
Rotor tooth width	(mm)	26
Rotor tooth height	(mm)	40
Stator tooth width	(mm)	20
Stator tooth height	(mm)	90
Stator slot opening	(mm)	26
Magnet width	(mm)	22
Magnet height	(mm)	90
Stack length	(mm)	200
Magnet mass	(kg)	~ 50

In addition the following assumptions are made:

- Iron lamination is employed in both stator and rotor;

- Rare earth PMs have 1.1 T remanence and 1.05 relative permeability;

- Rare earth PMs density is 7600 kg/m^3;

- The total current in slot is $\sim$ 10000 A (peak);

- end effects and side effects are neglected;

7.3. Results of the comparison

7.3.1. Load comparison

The PM modules presented above have been analyzed using 2D finite elements. Each operating point is obtained by performing a simulation over the whole electrical period. The first step of the study is to compare the rated thrust of the different modules, which work as generators and controlled according to the Maximum Thrust Per Ampere (MTPA) strategy: the angle of the stator current vector α_{ie} is changed, till the maximum thrust is reached. The power factor is include in the comparison. The average thrust of the SPM reference module is 12 kN, the thrust ripple is 2.5%. In SFPM module the average thrust is 9 kN and the thrust ripple is 4.0%, while referring to IPM topology average thrust is 15 kN and the thrust ripple is 2.0%. The results of the

Table 7.4: Results of the comparison for thrust (Rare Earth PMs)

	SPM	IPM	SFPM
Basic module slots-poles/teeth	12-10	12-10	12-10
Thrust (N) with Lstk=0.2 m	12100	15300	9000
Thrust ripple %	2.50	2.00	4.00
Power factor	0.82	0.9	0.63
Airgap thrust density %	100	126	75

thrust comparison are summarized in Table 7.4. The thrust developed by the SFPM module is poor (-25%) in respect to the well known SPM topology with the same PM magnet mass. This topology present the poorest power factor in respect to the SPM and IPM ones. The IPM module develops the highest thrust, almost +30% in respect to the SPM reference , thanks to the flux concentration. The trust ripple of the SFPM module is almost double the one of the other configurations.
The demagnetization behavior of the analyzed modules must be carefully evaluated. In this part of the study the software FEMAG [92] has been used with the courtesy of Leitwind AG and Prof.Konrad Reichert (Emeritus, ETH Zurich) [93]. The propagation of the demagnetizing field in SFPM module is shown in Fig. 7.4, varying the maximum allowed intrinsic field of the PM. It starts from an ideal magnet, with no demagnetization effect, the field is decreased down to 500 kA/m. On the flux density point of view this condition can be expressed as:

$$B_m > 0.4 \ T \tag{7.1}$$
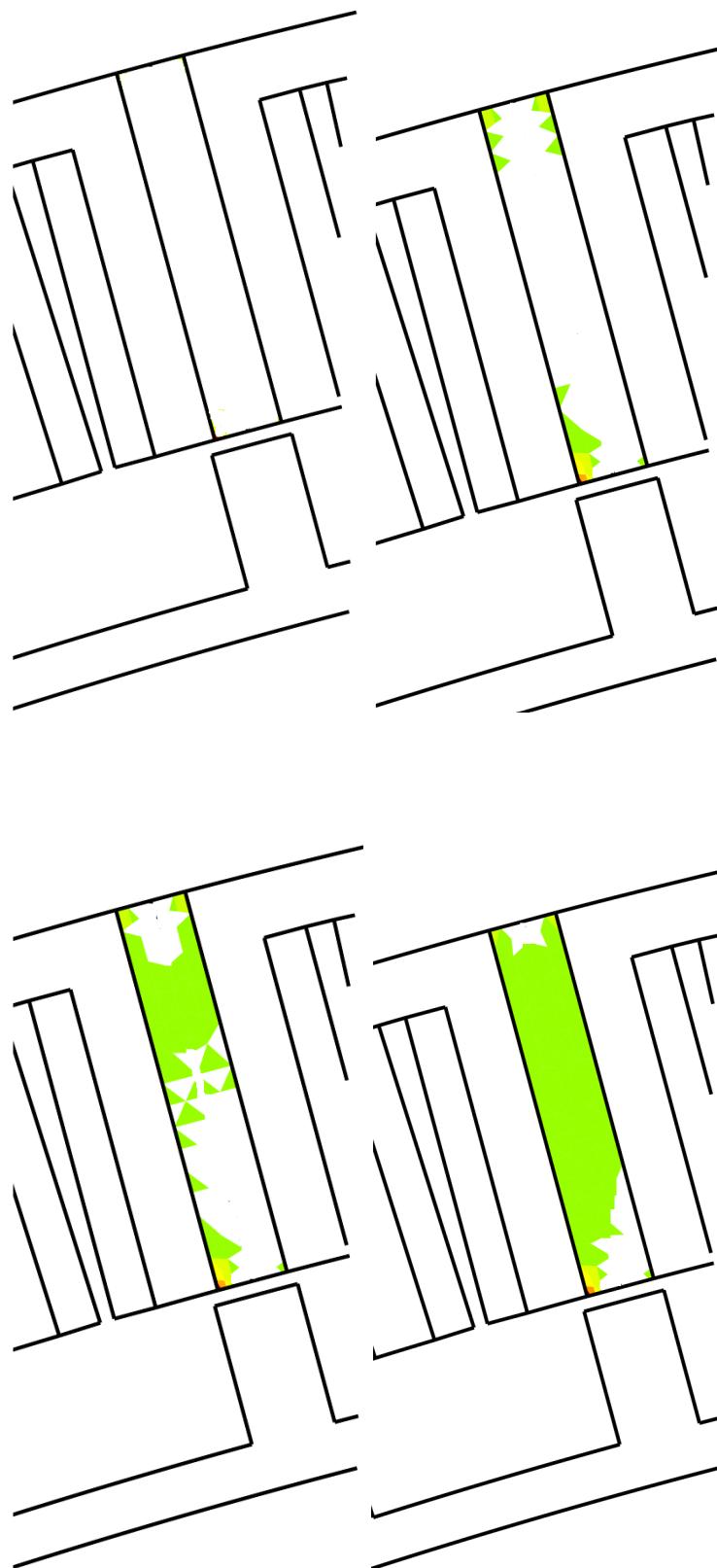
Figure 7.4: Propagation of the demagnetization in SFPM PM: the intrinsic field gradually goes down to 500 kA/m

Using rare earths PMs high intrinsic coercive force can be assumed (e.g. referring to average quality NdFeB PM it is about 1300 kA/m at 20°C temperature). However, it reduces with temperature: let consider that it goes down to about 450 kA/m if temperature rises up to 130°C. The demagnetization analysis has been done on all the modules also, two different limits are considered:

- demag1: the demagnetizing field is set to 680 kA/m, i.e. $B_m > 0.3\ T$;

- demag2: the demagnetizing field is set to 500 kA/m, i.e. $B_m > 0.4\ T$ as per (7.1).

For each topology the portion of demagnetized is calculated. The SPM module presents a good demagnetization resistance and the demagnetized area in 0.2% only with the most severe condition. The IPM module presents a good demagnetization resistance in demag1 case (0.3% demagnetized area), but the demagnetized area increases up to 3.4% in demag2 case (ten times in respect to demag1). The SFPM module results to be very sensitive to demagnetization in PMs: when the limit is set to 680 kA/m the demagnetized portion is 2.6%, the highest if compared to IPM and SPM in the same condition. The situation collapses if the field is set lower than 500 kA/m: almost the whole magnet is demagnetized. The results of the demagnetization analysis are summarized in Table 7.5.

Table 7.5: Results of the demagnetization analysis (Rare Earth PMs)

	SPM	IPM	SFPM
Basic module slots-poles/teeth	12-10	12-10	12-10
Demag. area PM demag1 %	0	0.3	2.6
Demag. area PM demag2 %	0.2	3.4	98

If rare earth PMs modules are considered, the machines which employ the flux concentration (e.g. IPM, SFPM modules) have the worst demagnetization behavior. The magnets of the considered SFPM module can be completely demagnetized even under nominal load if average quality NdFeB is employed. To completely avoid that phenomenon a higher grade NdFeB magnet or SmCo, which exhibits the knee of the B-H curve in the third quadrant (i.e. a very high coercive force) must be used.

7.3.2. Employing of ferrite PMs

A further comparison is carried out to evaluate the ferrite magnets instead of rare earth ones. Despite its low energy in respect to rare earth, ferrite has a lower impact on environment and human health. The extraction process of ferrite is similar to the iron one, while rare earths must be separated from radio elements [94], and can help to solve the problem of sustainability of life due to "own–built" human environment within Earth [95]. The previous analysis is repeated by replacing magnet materials but keeping the same geometries (Table 7.2-7.3). Each machine is labeled as follows:

- SFPMfe is SFPM machine with ferrite PMs;

- SPMfe is SPM machine with ferrite PMs;

- IPMfe is IPM machine with ferrite PMs;

Table 7.3.2 reports results for thrust comparison. The SPM machine with rare earth magnets of Table 7.4 has been considered as reference machine for thrust density in airgap. Ferrite PMs have 0.4 T remanence and 1.06 relative permeability and mass

Table 7.6: Results of the comparison for thrust (Ferrite PMs)

	SPMfe	IPMfe	SFPMfe
Basic module slots-poles/teeth	12-10	12-10	12-10
Thrust (N) with Lstk=0.2 m	4400	6500	4000
Thrust ripple %	1.50	7.00	4.20
Power factor	0.44	0.48	0.29
Airgap thrust density %	37	54	33

density equal to 5000 kg/m^3. As expected the nominal thrust of each module with ferrite PMs falls down, in comparison with the original rare earth machines. The torque of the SPMfe module collapses respect to the SPM module, with a -63% drop. Like in the case of Rare Earths this topology presents the poorest power factor in respect to the SPMfe and IPMfe ones: the impact of the cost of power electronics must be evaluated. The IPMfe module compared to the IPM module exhibits a -57% lack of thrust, slightly better than in SPM topology. The lack of torque of the SFPMfe module respect to the SFPM module is -56%: this machine behaves then like IPM machine. It is worth noticing that the torque ripple of the IPM linear modules increases after replacing rare earths PMs with ferrite PMs, while in SPM module this ripple reduces and tends to remain constant in SFPM module. Further study of IPM machine with different magnet materials is also reported in [73]. In particular the demagnetization of a tubular PM machine is considered in [96].

They have low intrinsic coercive force which is about 250-300 kA/m even at 20°C, according to [72], and the risk of demagnetization is high. It is worth noticing that the ferrite PMs have a stable demagnetization behavior in temperature, so the temperature of PMs is fixed at 20°C. The demagnetization analysis has been done on all the modules also, two different limits are considered:

- demag1: the demagnetizing field is set to 280 kA/m, i.e. $B_m > 0.05\ T$;

- demag2: the demagnetizing field is set to 255 kA/m, i.e. $B_m > 0.1\ T$.

For each topology the portion of demagnetized is calculated. The SPMfe module presents the best demagnetization resistance and the demagnetized area in 2.6% with the most severe condition. The IPMfe module presents an acceptable demagnetization resistance in demag1 case (2% demagnetized area), but the demagnetized area increases up to 4.6% in demag2 case (more than twice in respect to demag1). The SFPMfe module results to be the most sensitive one to demagnetization in PMs: when the limit is set to 280 kA/m the demagnetized portion is 14%, the highest if compared to IPMfe and SPMfe in the same condition. The situation collapses if the field is set lower than 255 kA/m: almost one third of the magnet is demagnetized. The results of the demagnetization analysis are summarized in Table 7.3.2.

Table 7.7: Results of the demagnetization analysis (Ferrite PMs)

	SPMfe	IPMfe	SFPMfe
Basic module slots-poles/teeth	12-10	12-10	12-10
Demag. area PM demag1 %	1	2	14
Demag. area PM demag2 %	2.6	4.6	30

Generally the demagnetization behavior gets worse when rare earths are replaced with ferrite. Like for rare earth, if ferrite PMs modules are considered, the machines which employ the flux concentration (e.g. IPMfe, SFPMfe modules) have the worst demagnetization behavior. The magnets of the considered SFPMfe module can heavily demagnetized even under nominal load if standard Ferrite is employed. To avoid that phenomenon ferrite with lanthanum or strontium should be employed, otherwise a strong redesign of the machine is required.

7.4. Recovering the gap between SFPM and SPM

7.4.1. The 12–14 flux switching module

In the previous comparison it has been shown that the SFPM topology has a lower airgap thrust density in respect to the SPM topology both with rare earth and ferrite. In order to recover this gap the SFPM module is modified: the armature part remains the same and the number of teeth of the translator is increased up to 14: this new module is called SFPMb (rare earth) and SFPMbfe (ferrite).

If rare earth PMs are considered, there thrust density is still -17% lower, but if ferrite is employed the difference in performance is filled and the same thrust is developed.

Table 7.4.1 reports results for comparison, including the demagnetization behavior.

Table 7.8: Adding SFPMb and SFPMbfe to the study

	SPM	SPMfe	SFPMb	SFPMbfe
Basic module slots-poles/teeth	12-10	12-10	12-14	12-14
Thrust (N) with Lstk=0.2 m	12100	4400	10000	4600
Thrust ripple %	2.50	1.50	5.00	5.40
Power factor	0.82	0.44	0.55	0.25
Airgap thrust density %	100	37	83	38
Demag. area PM demag1 %	0	1	1.7	0.8
Demag. area PM demag2 %	0.2	2.6	98	17

Despite the gap in thrust density has been recovered at least for SFPMbfe module, the power factor is very poor in respect to the SPMfe module: 0.25 instead of 0.44.

Both SFPMb and SFPMbfe module results to be very sensitive to demagnetization in PMs: the demagnetized portion of PM increases very remarkably (almost the whole magnet) when the field limit drops from 680 kA/m (demag1) down to 500 kA/m (demag2) for rare earth. If ferrite is employed the demagnetization behavior is better but the lost PM area is 20 times higher when the field limit drops from 280 kA/m (demag1) down to 255 kA/m (demag2).

7.4.2. The double–side flux switching module with ferrite

In this paragraph a double-side configuration of the switching flux PM module is proposed starting from literature [97]. The reference dimensions are still in (Table 7.2-7.3). The geometry of the armature part is modified by removing the iron yoke which connects the stator teeth. The PM quantity, the iron teeth quantity and the copper mass are kept constant. Ferrite PMs are employed.

Another translator is added on the opposite side in respect to the horizontal axe of the machine, including a second airgap. This new translator is shifted in respect to the existing one in order that its teeth are aligned with the slots of the other. The configuration with 10 teeth is considered.

Fig. 7.5 shows the switching flux PM generator module: it will be called DSFPMfe.
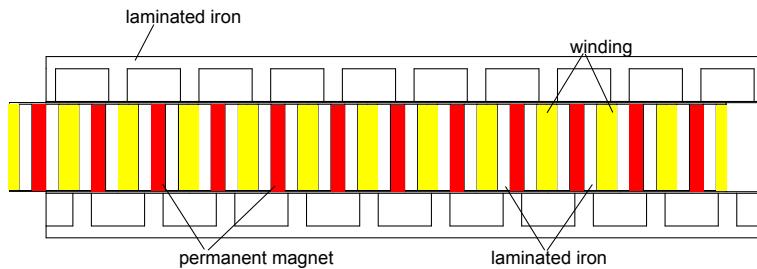
Figure 7.5: Double–sided flux switching module, DSFPMfe.

The mechanical complexity of the system increases but some aspects must be noticed:

- the structure of the translator is simple, like in reluctance machine and does not contain "precious material" (like PMs or copper);

- there is not a big impact on the active material cost then, if the translator is doubled;

- the normal forces acting on the bearing are now balanced.

The balancing of the electromagnetic forces acting on the bearing for such a structure is confirmed in [97]. Peak value of the normal force acting on the bearing is within 200 kN if single–sided SFPMfe is considered and this value results to be almost 100 times smaller referring to the double-sided module. It is then possible to reduce the airgap without increasing the structural sizing of the bearing: the DSFPM module is computed considering the airgap thickness equal to $5mm$ (the same of all the other modules in this study) at the beginning. Then the airgap thickness is halved in order to increase the thrust capability.

If a $5mm$ airgap is considered the thrust density of the DSFPMfe structure is 37% and the power factor almost doubles (0.58 instead of 0.29) in respect to the SFPMfe topology. This is positive from the point of view of the power electronics.

Table 7.4.2 reports results for comparison, including the demagnetization behavior.

Table 7.9: Comparison of SPM with double–sided switching flux DSFPMfe, g=5 mm

	SPM	SPMfe	SFPMfe	SFPMbfe	DSFPMb
Basic module slots-poles/teeth	12-10	12-10	12-10	12-14	12-10
Thrust (N) with Lstk=0.2 m	12100	4400	4000	4600	4400
Power factor	0.82	0.44	0.29	0.25	0.58
Airgap thrust density %	100	37	33	38	36
Demag. area PM demag1 %	0	1	14	1	4
Demag. area PM demag2 %	0.2	2.6	30	17	8

The sensitivity to demagnetization of DSFPMfe module is good because the demagnetized portion of PMs does not increase dramatically when the field limit drops from 280 kA/m (demag1) down to 255 kA/m (demag2). It is worth noticing that when the field limit is set to 255 kA/m the demagnetized area is the lowest in comparison to single–sided flux switching solutions with ferrite PMs.

The airgap of the double-sided module is now halved and the thrust capability grows up to 56%: it reaches the one of the IPMfe single–sided module. The power factor increase up to 0.8 which is the same range of SPM and IPM modules with rare earth PMs.

Table 7.4.2 reports results for comparison, including the demagnetization behavior.

The sensitivity to demagnetization of DSFPMfe module is confirmed to be good because the demagnetized portion of PMs does not increase dramatically when the field limit drops from 280 kA/m (demag1) down to 255 kA/m (demag2), even with

Table 7.10: Comparison of SPM and IPM with double–sided switching flux (DSFPMfe with halved g)

	SPM	SPMfe	IPMfe	SFPMfe	DSFPMb
Basic module slots-poles/teeth	12-10	12-10	12-10	12-10	12-10
Thrust (N) with Lstk=0.2 m	12100	4400	6500	4000	6800
Power factor	0.82	0.44	0.48	0.29	0.8
Airgap thrust density %	100	37	54	33	56
Demag. area PM demag1 %	0	1	2	14	8
Demag. area PM demag2 %	0.2	2.6	4.6	30	12

halved airgap. Again, when the field limit is set to 255 kA/m the demagnetized area is the lowest in comparison to single–sided flux switching solutions with ferrite PMs.

In Fig. 7.6, the demagnetization of single–sided SFPMfe structure is compare with the corresponding DSFPMfe module. The the field is set down to 280 kA/m. Pictures are made with software FEMM [12].
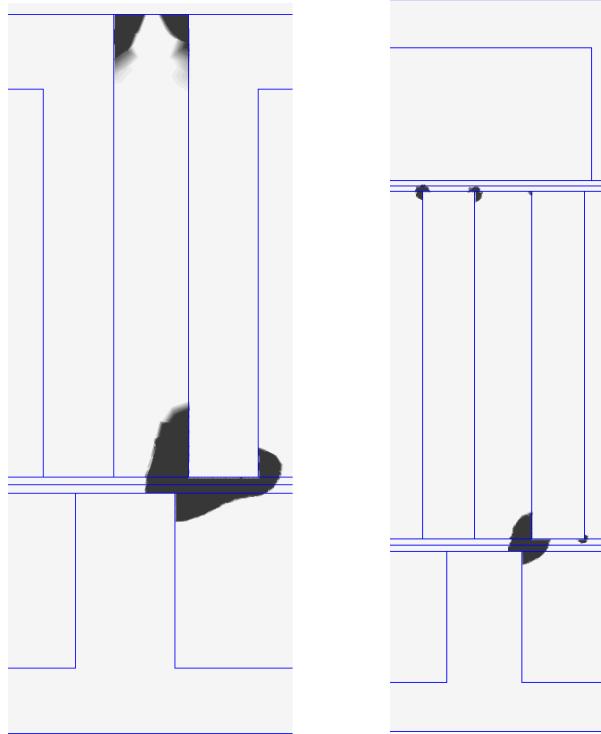

Figure 7.6: Demagnetization in SFPMfe and DSFPMfe PM: field limit set to 280 kA/m

7.5. Employment of the modules on a wave energy system

In this section the sizing of an electrical machines for a wave energy conversion system in literature [91] is used as the reference to evaluate the employing of the linear modules analyzed in this study. In this article different control strategies are employed to extract power from the waves and the size of the electrical generator is studied. More about proper control techniques to be employed in a wave power take off (PTO) can be found in [98–100].

7.5.1. Buoy structure and hydrodynamic model

Fig. 7.7 presents the comparison between buoyancy concepts: the one with linear modules and the other one with rotary machine. Special thanks are given to the authors of [91] for this paragraph. In order to properly represent the interaction between the sea
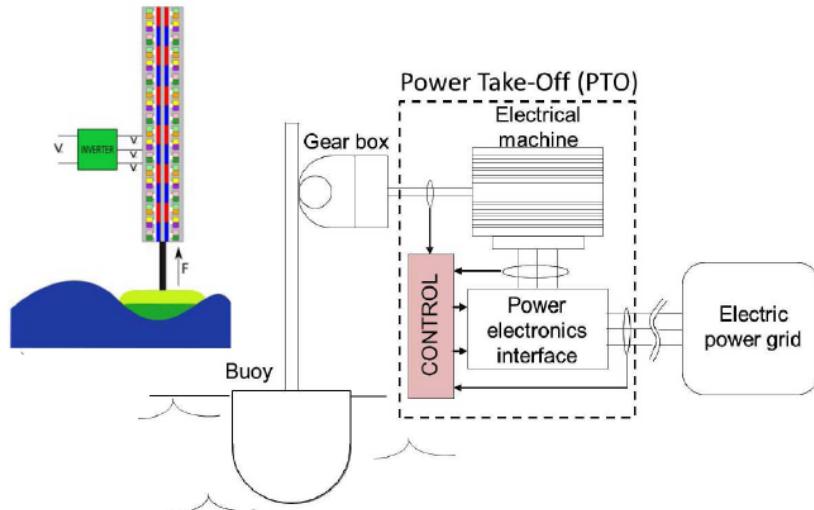
Figure 7.7: Buoyancy concepts: rotary versus linear

waves and the point absorber, which is a single degree of freedom device, the Cummins equation can be used [101]:

$$
\begin{aligned}
F_E(t) + F_L(t) = {} & (M + a_\infty)\ddot{s}(t) \\
& + \int_\infty^t K_{rad}(t - \tau)\ \dot{s}(\tau)\ d\tau + K\ s(t)
\end{aligned}
\tag{7.2}
$$

where s is the position of the buoy and $\dot{s}$ is its speed. F_E is the excitation force applied by the waves to the point absorber and F_L is the force applied by the PTO. The radiation force that represents the effect of radiated waves produced by the buoy oscillation needs also to be taken into account. In (7.2) it is expressed by the convolution integral, K_{rad} being the radiation impulse response function. Moreover, M is the mass of the device including the contribution due to the PTO inertia, K is the hydrostatic stiffness and a_∞ represents the value of added mass at infinite frequency [102]. It is

Table 7.11: Main data of the electrical machine

External diameter	D_e	500	mm
Airgap diameter	D	400	mm
Airgap	g	1	mm
Torque		1000	Nm

useful to analyse the behavior of the system under regular waves, i.e. sinusoidal waves, of period $T_{sin} = 2\pi/\omega$. In this case (7.2) can be rewritten as:

$$
\bar{F}_E(t) + \bar{F}_L(t) = -\omega^2 (M + A(\omega))\bar{S} \\
+ j\omega B(\omega)\bar{S} + K\bar{S}
\tag{7.3}
$$

where "$^-$" denotes complex operators, A represents the added mass at the considered frequency, accounting for the mass of water involved in the buoy movement; B is the mechanical damping. The point absorber can be modeled as a mass-spring-damper system and a corresponding electric equivalent can be derived, which is shown in Fig.7.8.
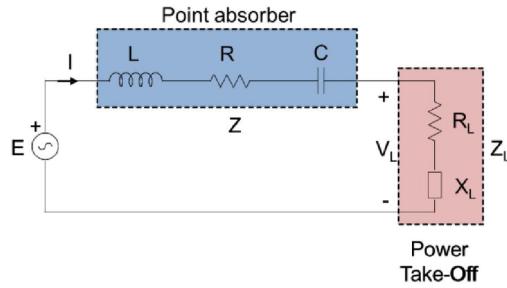

Figure 7.8: Electric equivalent of a point absorber wave energy converter

The excitation force F_E corresponds to the supply voltage, E in the electric analogue, while the buoy velocity corresponds to the current, I. The mass of the point absorber and PTO is represented by the inductance L, while the hydrostatic stiffness corresponds to the inverse of the capacitance C. The total buoy damping is represented by the resistance R. It is worth noticing that the representation of the system through its electric analogue is limited to a sinusoidal input, since both the total buoy mass (which includes the added mass) and the total damping (including the damping due to the radiation force) are frequency dependent. The control force is represented by the load voltage V_L, the damping coefficient B_L corresponds to the load resistance R_L, while the reactive control component M_L corresponds to the inductance X_L/ω.

7.5.2. Transition to linear motion

The proposed reference machine is a rotating one: a pinion converts the linear motion of a buoy through a gearbox (the ratio is 1:25). The characteristic are listed in Table 7.11.

The force which corresponds to torque sizing of the machine on the pinion side is then in equation (7.4). It will be considered as the Thrust reference to apply the linear

modules under study. The stack length of one module is $200mm$.

$$F = \frac{1000}{0.2} \cdot 25 = 125000\text{Nm} \tag{7.4}$$

The necessary number of modules is shown in Table 7.12. Generally speaking, more modules are required if rare earth PMs are replaced with ferrite PMs. The most compact solution with rare earth PMs is the IPM topology. The most compact solutions with ferrite PMs are the IPM topology and the double-sided DSFPMfe topology. The double-sided structure has the best value of power factor between the topologies which employs ferrite. A cost comparison is then necessary to have more information to properly choose the topology to adopt.

Table 7.12: Number of modules required by wave application

	SPM	SPMfe	IPM	IPMfe	SFPM	SFPMfe	DSFPMfe	SFPMb	SFPMfeb
Basic module slots-poles/teeth	12-10	12-10	12-10	12-10	12-10	12-10	12-10	12-14	12-14
Thrust (N) with Lstk=0.2 m	12100	4400	15300	6500	9000	4000	6800	10000	4600
Airgap thrust density %	100	37	126	54	75	33	57	83	38
Power factor	0.82	0.44	0.90	0.48	0.63	0.29	0.8	0.55	0.25
Required number of modules	10	28	8	19	14	30	18	13	27

7.6. Final Comparison

The study deals with cost estimation of the active material to evaluate the compared machines in term of USD/kg, both for rare earth and ferrite PMs, considering the standard magnet characteristics presented in Section 7.3.1 and 7.3.2. Following quotations are considered, starting from literature [46, 47, 93]:

- Cost of NdFeB PMs average grade: 60 USD/kg;

- Cost of ferrite PMs: 10 USD/kg;

- Cost of copper: 11.2 USD/kg;

- Cost of iron lamination: 2.2 USD/kg;

- Cost of power electronics: 65 USD/kVA (only one third is proportional to apparent power, two third is proportional to active power);

To evaluate the specific cost referred to thrust of power electronics 1 m/s average speed is chosen. The results of the cost comparison are shown in Table 7.13, including the demagnetization behavior. It results:

- There is no economical convenience if ferrite PMs are employed in SPM structure, without acting on machine geometry, because the total cost per thrust increases from 0.38 USD/Nm up to 0.43 USD/Nm.

- Referring to the IPM structures, the economical impact is almost the same if rare earths or ferrite PMs are employed. This structure is one of the most competitive, thanks to the flux concentration principle.

- It could seem there is a convenience in employing ferrite with SFPM or SFPMb structure, because the active cost per thrust drops down. Otherwise the poor power factor of these structures let the cost of power electronics grows and the total cost is not competitive at the end. These structure is also very sensitive to demagnetization: particular care must be given during the design phase and special ferrite with lanthanum or strontium should be used;

- The economical convenience of the double-side flux switching machine with ferrite is evident. The proposed configuration has the lowest specific cost 0.28 USD/Nm, good power factor and much lower sensitivity to demagnetization in respect to the single–sided switching flux modules. It is worth remembering that the structure is more complex and that the airgap is halved in respect to the other modules under study.

The over–length factor is then considered starting from Table 7.1 in order to guarantee overlapping between the armature and the translator of the module, during the working operations. This factor $Ov = 1.6$ is applied to the translator of each modules and the armature part with windings is considered fixed (no brushes are required with advantages on maintenance and reduction of the fault probability).

A new cost scenario is generated, because the possibility to pack all the "precious material" (PMs and copper) in the armature part of the switching flux topology gives the advantage of not increasing the mass of PMs. Their specific cost remains practically constant. The increasing of the specific cost of the modules with ferrite is then reduced in respect to the rare earth ones.

Table 7.13: Evaluation of the specific cost for each topology

	SPM	SPMfe	IPM	IPMfe	SFPM	SFPMfe	DSFPMfe	SFPMb	SFPMfeb
Basic module slots-poles/teeth	12-10	12-10	12-10	12-10	12-10	12-10	12-10	12-14	12-14
Thrust (N) with Lstk=0.2 m	12100	4400	15300	6500	9000	4000	6800	10000	4600
Airgap thrust density %	100	37	126	54	75	33	57	83	38
Power factor	0.82	0.44	0.90	0.48	0.63	0.29	0.8	0.55	0.25
Demag. area PM demag1 %	0	1	0.33	2	2.6	14	8	1.65	0.8
Demag. area PM demag2 %	0.2	2.6	3.4	4.6	98	30	12	98	17
Required number of modules	10	28	8	19	14	30	18	13	27
Active cost on thrust USD/N	0.31	0.33	0.24	0.22	0.41	0.34	0.21	0.37	0.31
Electronics cost on thrust USD/N	0.07	0.10	0.07	0.09	0.08	0.12	0.07	0.09	0.13
Total cost on thrust USD/N	0.38	0.43	0.31	0.31	0.49	0.46	0.28	0.46	0.44
Cost on thrust, overlength USD/N	0.51	0.48	0.42	0.35	0.49	0.48	0.30	0.47	0.46

Conclusions

Conclusions of this doctoral study are then summarized

This doctoral study started to answer the will of the company Leitwind A.G. to choose the proper winding for a new direct drive permanent magnet generator with large diameter ($D \backsim 4m$), called LW30A. The will to implement a method to predict rotor losses in large machines with permanent magnet and fractional slot windings was the key basic point to be solved. The computation of these losses according to standard procedures (e.g. Steinmetz equation or models for massive body within homogeneous field) is not satisfactory.

As a first step the analysis and modeling of the existing Leitwind LW15C generator ($D \backsim 3m$) for 1.5 MW wind turbine has been done, both with analytical and finite elements models. The same has been done for the SFA motor ($D \backsim 2m$) for direct drive ropeway traction,built by Leitner A.G. Leitwind and Leitner belong to the Leitner Technologies Group. The activity on the Back-to-Back test bench has shown the good agreement between the models and the real machines. The models are a suitable starting point for the the LW30A generator design.

As a second step the detailed computation of rotor losses has been faced. The space harmonics of the magneto motive force (MMF) due to the fractional–slot windings lead to considerable rotor losses, even in the rare earth permanent magnets (PMs) themselves. They act on their working temperature which is strictly related to the performance of the machine.

The finite element current sheet method and the analytical straight–lined model have first been applied to the existing large diameter machine of the Leitner Technologies group. The current sheet method have been validated by the activity on the Back-to-Back test bench: the rise of the temperature in the different part of the rotor structure has provided the terms of comparison to use it on large direct drive machines.

With the same method it has been shown that if a basic fractional slot PM machine is scaled according to a factor l, the losses in rotor vary with the seventh power, l^7. This highlights the importance of implementing the method for computation of losses on the existing machines in order design the larger new one.

The analytical straight–lined model has been used together with the Index of Rotor

Losses to make a first analysis of the possible windings for LW30A generator. The winding factor has then been computed for each considered winding and used as an index of the electromagnetic torque.

A deeper investigation has finally been done with finite element current sheet method to fix the choice of the final winding. The number of slot and poles chosen is according the 12–10 single layer winding, which resulted to be the best compromise between rotor losses reduction and torque production. A machine periodicity suitable for the new diameter has been chose.

The torque capability of different topologies of PM machines with fractional slot winding have then been investigated and compared with the switching flux configuration (SFPM), both with rare earths and ferrite PMs. Despite their interesting cost, the machines employing the flux concentration principle have resulted to be sensitive to demagnetization in PMs, especially if ferrite replaces rare earth. The SFPM topology is the most affected by this phenomenon.

To extend the scenario of renewable energy, linear direct drive modules for wave energy conversion have been considered. Different topologies have been analyzed, including the possibility of employing a double-side structure. The using of ferrite PMs is also considered: despite their low energy in respect to rare earth ones they have a lower impact on environment and human health. The double–side topology with ferrite has resulted to be interesting in cost and demagnetization behavior.

Ringraziamenti–Acknowledgements

Arrivato alla fine di questo lavoro di tesi desidero innanzi tutto ringraziare la Leitwind e Matteo Casazza per la possibilità concessami e per avermi trasmesso la capacità di vedere lavoro e studio come un'evoluzione, in cui saper mettere in dubbio è importante come riuscire a trovare certezze.

Assieme a lui ringrazio sentitamente il mio supervisore Nicola Bianchi, per il suo modo di sapersi meravigliare e perdere nel mondo dell'elettromagnetismo, nonchè per le situazioni di vita passate assieme che mi hanno fatto maturare.

Voglio esprimere la mia gratitudine a Georg Folie, per la pazienza e la disponibilità che mi ha sempre mostrato, aiutandomi ad essere saldo nelle situazioni difficili.

Desidero ringraziare le persone con cui condivido la quotidianità in Leitwind, perchè ognuna di loro mi ha dato qualcosa.

Ringrazio in modo speciale Alessandro Venturoli, per avere dato il via alla mia vita professionale, e Thomas Kässner per avermi portato a lavorare nell'affascinante ambito delle energie rinnovabili.

Da quando mi sono laureato fino ad oggi vi sono quelli che considero i miei Maestri di Elettromagnetismo: il Prof.Gaetano Malesani, il Prof.Augusto Morini, il Prof.Andrea Tortella, il Prof.Nicola Bianchi, il Prof.Konrad Reichert, l'Ing.Gianni Regazzi, l'Ing. Harri Vihriälä e l'Ing.Otto Pabst. A loro va il mio pensiero e la mia gratitudine.

Viene ora il Laboratorio di Azionamenti e con questo il Prof.Silverio Bolognani e i ragazzi con cui ho diviso questi tre anni. Ringrazio Mosè Castiello per la sua presenza in Laboratorio. Ringrazio Emanuele (con la 'E!') Fornasiero per la pazienza e la disponibilità infinite, nonchè per il sapere che mi ha trasmesso. Ringrazio Mattia Morandin e Massimo Barcaro perchè mi hanno ripetutamente sostenuto nella mia situazione di dottorando part–time. Ringrazio sentitamente Dario Durello per il sostegno e l'amicizia nei miei confronti. Un grazie va a Matthias Preindl per la sua continua disponibilità e le chiacchierate assieme.

Un pensiero va a Luigi Alberti per la grande amicizia e ad Elisabetta Tedeschi, che mi hanno coinvolto nel mondo dell'energia da moto ondoso.

Un grazie non può mancare al Prof.Mauro Andriollo.

Ringrazio Giuseppe Olivato per tutti i suoi suggerimenti su questa tesi.

Nel ringraziare tutti gli amici devo ricordare Stefano 'Cino' Aldegheri per essere sempre presente e per i suoi consigli, qualunque cosa mi sia servita.

Voglio ringraziare Giampaolo, Antonietta, Chiara e Francesca per il loro sostegno da sempre. Voglio ringraziare Paolo, Gabriella ed Elena per essere entrati a far parte del sostegno di cui sopra.

Ancora ringrazio Elena per l'inesauribile tenacia che la contraddistingue e per avermela insegnata.

Padova, 31 January 2013   Alessandro Fasolo

This Thesis is written in LaTeX.
An electronic version is available at: *http://paduaresearch.cab.unipd.it*

Bibliography

[1] EWEA, *Wind energy and EU climate policy, Achieving 30 per cent lower emissions by 2020.* A report by the European Wind Energy Association, October 2011.

[2] ——, *Wind in our Sails, The coming of Europe's offshore wind energy industry.* A report by the European Wind Energy Association, 2011.

[3] ——, *Green Growth, The impact of wind energy on jobs and the economy.* A report by the European Wind Energy Association, April 2012.

[4] Leitwind, "www.leitwind.com."

[5] Leitner, "www.leitner.com."

[6] F. d. O. Falcao, "Wave energy utilization: a review of the technologies," *Renewable and Sustainable Energy Reviews, Elsevier*, pp. 900 –915, october 2009.

[7] A. Muetze and J. Vining, "Ocean wave energy conversion - a survey," in *Industry Applications Conference, 2006. 41st IAS Annual Meeting. Conference Record of the 2006 IEEE*, vol. 3, oct. 2006, pp. 1410 –1417.

[8] J. Vining and A. Muetze, "Economic factors and incentives for ocean wave energy conversion," *Industry Applications, IEEE Transactions on*, vol. 45, no. 2, pp. 547 –554, march-april 2009.

[9] EWEA, *Delivering offshore electricity to the EU Spatial planning of offshore renewable energies and electricity grid infrastructures in an integrated EU maritime policy.* Seanergy2020, May 2012.

[10] D.Durello, "Comparison between different wind generators configurations (in italian)," july 2010, Supervisor N. Bianchi,University of Padua.

[11] N. Bianchi, M. D. Pré, L. Alberti, and E. Fornasiero, *Theory and Design of Fractional–Slot PM Machines*, ser. IEEE IAS Tutorial Course notes, IAS'07 Annual Meeting. CLEUP, Padova (Italy), New Orleans, LA, September 23, 2007, (info@cleup.it).

[12] D.Meeker, "www.femm.info/wiki/homepage."

[13] GL, "Rules and guidelines, industrial service," in *GL IV*, 2010.

[14] IEC, "Rules and guidelines, industrial service," in *International Standard IEC 60034-1*, apr. 2004.

[15] ——, "Rules and guidelines, industrial service," in *International Standard IEC 60034-29*, mar. 2008.

[16] Leitner, "www.leitner-technologies.com, *http://paper.holzweg.tv/title/Drive+System /pdf/http:/it.leitner-lifts.com/content/download/8679/373376/version/4/file /TechInfo_Antrieb_en_komplett.pdf*."

[17] J. Cros and P. Viarouge, "Synthesis of high performance pm machines with concentrated windings," *Energy Conversion, IEEE Transactions on*, vol. 17, no. 2, pp. 248–253, jun 2002.

[18] A. Williamson, E. Spooner, and L. Thompson, "Large modular pm generators," in *New Topologies for Permanent Magnet Machines (Digest No: 1997/090), IEE Colloquium on*, jun 1997, pp. 4/1 –4/6.

[19] Z. Chen and E. Spooner, "A modular, permanent-magnet generator for variable speed wind turbines," in *Electrical Machines and Drives, 1995. Seventh International Conference on (Conf. Publ. No. 412)*, sep 1995, pp. 453 –457.

[20] E. Spooner and A. Williamson, "Modular, permanent-magnet wind-turbine generators," in *Industry Applications Conference, 1996. Thirty-First IAS Annual Meeting, IAS '96., Conference Record of the 1996 IEEE*, vol. 1, oct 1996, pp. 497 –502 vol.1.

[21] H. Polinder and M. Hoeijmakers, "Eddy-current losses in the permanent magnets of a pm machine," in *Electrical Machines and Drives, 1997 Eighth International Conference on (Conf. Publ. No. 444)*, sep 1997, pp. 138 –142.

[22] D. Ishak, Z. Q. Zhu, and D. Howe, "Eddy–current loss in the rotor magnets of permanent–magnet brushless machines having a fractional number of slots per pole," *Magnetics, IEEE Transactions on*, vol. 41, no. 9, pp. 2462–2469, sep. 2005.

[23] M. Andriollo, G. Bettanini, G. Martinelli, A. Morini, and A. Tortella, "Pm losses evaluation by harmonic analysis of the magnetic vector potential perturbation," in *Power and Energy Society General Meeting - Conversion and Delivery of Electrical Energy in the 21st Century, 2008 IEEE*, july 2008, pp. 1 –6.

[24] D. Ishak, Z. Q. Zhu, and D. Howe, "Permanent magnet brushless machines with unequal tooth widths and similar slot and pole numbers," *Industrial Application, IEEE Transactions on*, vol. 41, no. 2, pp. 584–590, mar.-apr. 2005.

[25] L. Alberti, E. Fornasiero, N. Bianchi, and S. Bolognani, "Impact of rotor losses in a 12-slot 10-pole axial flux pm machine," in *Industry Applications Society Annual Meeting, 2008. IAS '08. IEEE*, oct. 2008, pp. 1 –8.

[26] P. Salminen, "Fractional slot permanent magnet synchronous motor for low speed applications," Dissertation, 198, Lappeenranta University of Technology, Lappeenranta, Finland, 2004, iSBN 951-764-982-5(pdf).

[27] N. Bianchi, S. Bolognani, and E. Fornasiero, "A general approach to determine the rotor losses in three–phase fractional–slot pm machines," vol. 1, 2–5 May 2007, Antalya, Turkey, pp. 634–641.

[28] H. Polinder and M. Hoeijmakers, "Eddy-current lossesin the permanent magnets of a pm machine," in *IEE Proceedings of Electr. Power Appl.*, vol. 146, no. 3, may 1999, pp. 261–266.

[29] E.Fornasiero, "Advanced design of direct drive pm machines," Dissertation, 2728, University of Padova, Padova, Italy, 2004, (pdf).

[30] N. Bianchi and E. Fornasiero, "Impact of MMF Space Harmonic on Rotor Losses in Fractional-slot Permanent-magnet Machines," *IEEE Transactions on Energy Conversion*, vol. 24, no. 2, pp. 323–328, Jun. 2009.

[31] E. Fornasiero, N. Bianchi, and S. Bolognani, "Slot harmonic impact on rotor losses in fractional-slot permanent-magnet machines," *Industrial Electronics, IEEE Transactions on*, vol. 59, no. 6, pp. 2557 –2564, june 2012.

[32] E. Spooner and A. Williamson, "Parasitic losses in modular permanent-magnet generators," *Electric Power Applications, IEE Proceedings -*, vol. 145, no. 6, pp. 485 –496, nov 1998.

[33] E. Spooner, "Measurement of parasitic losses in modular permanent-magnet generators," in *Testing of Electrical Machines (Ref. No. 1999/161), IEE Half Day Colloquium on*, 1999, pp. 4/1 –4/6.

[34] B. Mecrow, A. Jack, and J. Haylock, "Fault–tolerant permanent–magnet machine drives," *IEE Proc., Electr. Power Applications*, vol. 143, no. 6, pp. 437–442, dec. 1996.

[35] A. El-Refaie and T. Jahns, "Optimal flux weakening in surface pm machines using concentrated windings," in *Industry Applications Conference, 2004. 39th IAS Annual Meeting. Conference Record of the 2004 IEEE*, vol. 2, oct. 2004, pp. 1038 – 1047 vol.2.

[36] K. Atallah, D. Howe, P. H. Mellor, and D. A. Stone, "Rotor loss in permanent-magnet brushless AC machines," *IEEE Transactions on Industry Applications*, vol. 36, no. 6, pp. 1612–1618, Nov./Dec. 2000.

[37] M. Shah and S. Lee, *IEEE Transactions on Industry Applications*, vol. 42, no. 3, pp. 642–649, may–june 2006.

[38] H. Nakano, M. Kometani and M. Kawamura, "A study on eddy-current losses in rotors of surface permanent-magnet synchronous machines," *Transactions on Industry Applications*, vol. 42, no. 2, pp. 429–435, mar.-apr. 2006.

[39] A. Boglietti, A. Cavagnino, D. Staton, M. Shanel, M. Mueller, and C. Mejuto, "Evolution and modern approaches for thermal analysis of electrical machines," *IEEE Transactions on Industrial Electronics*, vol. 56, no. 3, pp. 871 –882, mar. 2009.

[40] P. Milanfar and J. Lang, "Monitoring the thermal condition of permanent-magnet synchronous motors," *IEEE Transactions on Aerospace and Electronic Systems*, vol. 32, no. 4, pp. 1421–1429, oct. 1996.

[41] F. Briz, M. Degner, P. Garcia, and A. Dicz, "Induction machine diagnostics using zero sequence component," in *Industry Applications Conference, 2005. Fourtieth IAS Annual Meeting. Conference Record of the 2005*, vol. 1, oct. 2005, pp. 34 –41.

[42] S. Rajagopalan, W. Roux, T. Habetler, and R. Harley, "Dynamic eccentricity and demagnetized rotor magnet detection in trapezoidal flux (brushless dc) motors operating under different load conditions," *IEEE Transactions on Power Electronics*, vol. 22, no. 5, pp. 2061–2069, sep. 2007.

[43] J. Rosero, L. Romeral, J. Ortega, and J. Urresty, "Demagnetization fault detection by means of hilbert huang transform of the stator current decomposition in pmsm," in *IEEE International Symposium on Industrial Electronics, 2008. ISIE 2008.*, vol. 3, jun.-jul. 2008, pp. 172–177.

[44] M. Prieto, A. Espinosa, J. Ruiz, J. Urresty, and J. Ortega, "Feature extraction of demagnetization faults in permanent-magnet synchronous motors based on box-counting fractal dimension," *IEEE Transactions on Industrial Electronics*, vol. 58, no. 5, pp. 1594–1605, may 2011.

[45] N. Bianchi and E. Fornasiero, "Index of rotor losses in three-phase fractional-slot permanent magnet machines," *Electric Power Applications, IET*, vol. 3, no. 5, pp. 381 –388, september 2009.

[46] R. Gupta and N. Mohan, "A three-phase permanent magnet brushless dc motor for low-power low-speed fan applications - optimizing cost and efficiency," in *Industry Applications Conference, 2007. 42nd IAS Annual Meeting. Conference Record of the 2007 IEEE*, sept. 2007, pp. 846 –852.

[47] J. Li and K. Chau, "Performance and cost comparison of permanent-magnet vernier machines," *IEEE Transactions on Applied Superconductivity*, vol. PP, no. 99, p. 1, 2011.

[48] E. Fornasiero, L. Alberti, N. Bianchi, and S. Bolognani, "Considerations on selecting fractional–slot windings," in *Energy Conversion Congress and Exposition (ECCE), 2010 IEEE*, sept. 2010, pp. 1376 –1383.

[49] V. H. J. Pyrhonen, T. Jokinen, *Design of Rotating Electrical Machines*. John Wiley and Sons, 2008.

[50] W. Schuisky, *Berechnung Elektrischer Machinen*. Springer Verlag, Wien, 1967.

[51] S. Ooi, S. Morimoto, M. Sanada, and Y. Inoue, "Performance evaluation of a high power density pmasynrm with ferrite magnets," in *Energy Conversion Congress and Exposition (ECCE), 2011 IEEE*, sept. 2011, pp. 4195 –4200.

[52] J. Chen, Z. Zhu, S. Iwasaki, and R. Deodhar, "Low cost flux-switching brushless ac machines," in *Vehicle Power and Propulsion Conference (VPPC), 2010 IEEE*, sept. 2010, pp. 1 –6.

[53] Z. Zhu and J. Chen, "Advanced flux-switching permanent magnet brushless machines," *IEEE Transactions on Magnetics*, vol. 46, no. 6, pp. 1447 –1453, june 2010.

[54] Z. Zhu, Y. Pang, D. Howe, S. Iwasaki, R. Deodhar, and A. Pride, "Analysis of electromagnetic performance of flux-switching permanent-magnet machines by nonlinear adaptive lumped parameter magnetic circuit model," *IEEE Transactions on Magnetics*, vol. 41, no. 11, pp. 4277 – 4287, nov. 2005.

[55] A. Thomas, Z. Zhu, G. Jewell, and D. Howe, "Flux-switching pm brushless machines with alternative stator and rotor pole combinations," in *International Conference on Electrical Machines and Systems, 2008. ICEMS 2008.*, oct. 2008, pp. 2986 –2991.

[56] J. Chen and Z. Zhu, "Comparison of all- and alternate-poles-wound flux-switching pm machines having different stator and rotor pole numbers," *IEEE Transactions on Industry Applications*, vol. 46, no. 4, pp. 1406 –1415, july-aug. 2010.

[57] L. Huang, H. Yu, M. Hu, J. Zhao, and Z. Cheng, "A novel flux-switching permanent-magnet linear generator for wave energy extraction application," *IEEE Transactions on Magnetics*, vol. 47, no. 5, pp. 1034 –1037, may 2011.

[58] J. Wang, W. Wang, K. Atallah, and D. Howe, "Design considerations for tubular flux-switching permanent magnet machines," *IEEE Transactions on Magnetics*, vol. 44, no. 11, pp. 4026 –4032, nov. 2008.

[59] R. Cao, M. Cheng, C. Mi, W. Hua, and W. Zhao, "A hybrid excitation flux-switching permanent magnet linear motor for urban rail transit," in *Vehicle Power and Propulsion Conference (VPPC), 2011 IEEE*, sept. 2011, pp. 1 –5.

[60] A. Thomas, Z. Zhu, R. Owen, G. Jewell, and D. Howe, "Multi-phase flux-switching permanent magnet brushless machine for aerospace application," in *Industry Applications Society Annual Meeting, 2008. IAS '08. IEEE*, oct. 2008, pp. 1 –8.

[61] Y. Pang, Z. Zhu, D. Howe, S. Iwasaki, R. Deodhar, and A. Pride, "Comparative study of flux-switching and interior permanent magnet machines," in *International Conference on Electrical Machines and Systems, 2007. ICEMS.*, oct. 2007, pp. 757 –762.

[62] A. Vagati, G. Pellegrino, and P. Guglielmi, "Comparison between spm and ipm motor drives for ev application," in *2010 XIX International Conference on Electrical Machines (ICEM)*, sept. 2010, pp. 1 –6.

[63] G. Pellegrino, A. Vagati, P. Guglielmi, and B. Boazzo, "Performance comparison between surface-mounted and interior pm motor drives for electric vehicle application," *IEEE Transactions on Industrial Electronics*, vol. 59, no. 2, pp. 803 –811, feb. 2012.

[64] A. S. Thomas, Z. Q. Zhu, and G. Jewell, "Comparison of flux switching and surface mounted permanent magnet generators for aerospace applications," in

5th IET International Conference on Power Electronics, Machines and Drives (PEMD 2010), april 2010, pp. 1 –5.

[65] A. Thomas, Z. Zhu, and G. Jewell, "Comparison of flux switching and surface mounted permanent magnet generators for high-speed applications," *Electrical Systems in Transportation, IET*, vol. 1, no. 3, pp. 111 –116, september 2011.

[66] W. Hua, M. Cheng, Z. Zhu, and D. Howe, "Design of flux-switching permanent magnet machine considering the limitation of inverter and flux-weakening capability," in *Industry Applications Conference, 2006. 41st IAS Annual Meeting. Conference Record of the 2006 IEEE*, vol. 5, oct. 2006, pp. 2403 –2410.

[67] M. Barcaro, N. Bianchi, and F. Magnussen, "Faulty operations of a pm fractional-slot machine with a dual three-phase winding," *IEEE Transactions on Industrial Electronics*, vol. 58, no. 9, pp. 3825 –3832, sept. 2011.

[68] M. Barcaro, L. Alberti, and N. Bianchi, "Thermal analysis of dual three-phase machines under faulty operations," in *IEEE International Symposium on Diagnostics for Electric Machines, Power Electronics Drives (SDEMPED), 2011*, sept. 2011, pp. 165 –171.

[69] M. Barcaro, A. Faggion, N. Bianchi, and S. Bolognani, "Sensorless rotor position detection capability of a dual three-phase fractional-slot ipm machine," in *Energy Conversion Congress and Exposition (ECCE), 2011 IEEE*, sept. 2011, pp. 3037 –3044.

[70] M. Barcaro, N. Bianchi, E. Fornasiero, and F. Magnussen, "Experimental comparison between two fault-tolerant fractional-slot multiphase pm motor drives," in *2010 IEEE International Symposium on Industrial Electronics (ISIE)*, july 2010, pp. 2160 –2165.

[71] M. Barcaro, N. Bianchi, and F. Magnussen, "Analysis and tests of a dual three-phase 12-slot 10-pole permanent-magnet motor," *IEEE Transactions on Industry Applications*, vol. 46, no. 6, pp. 2355 –2362, nov.-dec. 2010.

[72] Arnold-Magnetics, "Arnox permanent magnet catalog 101117 www.arnoldmagnetics.com."

[73] L. Fang, B. Lee, J. Lee, H. Kim, and J. Hong, "Study on high-efficiency characteristics of interior permanent magnet synchronous motor with different magnet material," in *International Conference on Electrical Machines and Systems, 2009. ICEMS 2009.*, nov. 2009, pp. 1 –4.

[74] Float-Incorporated, "www.floatinc.org."

[75] P. Holtedahl, "Wind and ocean: a european market study, energiuka, oslo," in *www.innovasjonnorge.no*, feb. 2008.

[76] S. Chevailler, "Comparative study and selection criteria of linear motors," Dissertation, Ecole Polytechnique Federale de Lausanne, july 2006, (pdf).

[77] B. Gysen, E. Lomonova, J. Paulides, and A. Vandenput, "Analytical and numerical techniques for solving laplace and poisson equations in a tubular permanent magnet actuator: Part i. semi–analytical framework," *Magnetics, IEEE Transactions on*, vol. 44, no. 7, july 2008.

[78] ——, "Analytical and numerical techniques for solving laplace and poisson equations in a tubular permanent magnet actuator: Part ii. schwarz–christoffel mapping," *Magnetics, IEEE Transactions on*, vol. 44, no. 7, pp. 1761 –1767, 2008.

[79] L. Encica, J. Paulides, E. Lomonova, and A. Vandenput, "Electromagnetic and thermal design of a linear actuator using output polynomial mapping," in *Industry Applications Conference, 2006. 41st IAS Annual Meeting. Conference Record of the 2006 IEEE*, vol. 4, 2006, pp. 1919 –1926.

[80] H. Polinder, M. Damen, and F. Gardner, "Linear pm generator system for wave energy conversion in the aws," *Energy Conversion, IEEE Transactions on*, vol. 19, no. 3, pp. 583 – 589, 2004.

[81] H. Polinder, B. Mecrow, A. Jack, P. Dickinson, and M. Mueller, "Conventional and tfpm linear generators for direct-drive wave energy conversion," *Energy Conversion, IEEE Transactions on*, vol. 20, no. 2, pp. 260 – 267, june 2005.

[82] M. G. Prado, F. Gardner, M. Damen, and H. Polinder, "Modelling and test results of the archimedes wave swing," *Proceedings of the I MECH E Part A Journal of Power and Energy*, vol. 220, no. 8, pp. 855 – 868, 2006.

[83] G. Bracco, E. Giorcelli, F. Marignetti, and G. Mattiazzo, "Iswec: application of linear tubular generators," in *Industrial Electronics (ISIE), 2010 IEEE International Symposium on*, july 2010, pp. 2426 –2430.

[84] G. Bracco, E. Giorcelli, G. Mattiazzo, F. Marignetti, S. Carbone, and C. Attaianese, "Design and experiments of linear tubular generators for the inertial sea wave energy converter," in *Energy Conversion Congress and Exposition (ECCE), 2011 IEEE*, sept. 2011, pp. 3864 –3871.

[85] T. Brekken, A. von Jouanne, and H. Y. Han, "Ocean wave energy overview and research at oregon state university," in *Power Electronics and Machines in Wind Applications, 2009. PEMWA 2009. IEEE*, june 2009, pp. 1 –7.

[86] J. Vining, T. Lipo, and G. Venkataramanan, "Experimental evaluation of a doubly-fed linear generator for ocean wave energy applications," in *Energy Conversion Congress and Exposition (ECCE), 2011 IEEE*, sept. 2011, pp. 4115 –4122.

[87] H. Polinder, B. Mecrow, A. Jack, P. Dickinson, and M. Mueller, "Linear generators for direct-drive wave energy conversion," in *Electric Machines and Drives Conference, 2003. IEMDC'03. IEEE International*, vol. 2, june 2003, pp. 798 – 804 vol.2.

[88] SEAQUEST, "Development of a wave energy converter," in *Leading Organization, Mecànica Industria Buelna, Meeting Eurogia+, Madrid*, feb 2010.

[89] A. Serena and M. Molinas, "Design of an arch-shaped fspm generator for the seaquest concept," in *Electrical Machines (ICEM), 2012 XXth International Conference on*, sept. 2012, pp. 627 –632.

[90] ——, "Design of direct drive wave energy conversion system for the seaquest concept," in *Ocean Energy (ICOE), 2012 4th International Conference on, Dublin*, oct. 2012.

[91] L. Alberti, E. Tedeschi, N. Bianchi, M. Santos, and A. Fasolo, "Effect of the generator sizing on a wave energyconverter considering different control strategies," *The International Journal for Computation and Mathematics in Electrical and Electronic Engineering (COMPEL)*, jan 2013.

[92] K.Reichert, "www.femag.de."

[93] A.Fasolo, "Switching flux and fractional slot pm modules for direct drive application," in *Femag User Meeting 2012, Hanau, Germany*, presentation, www.femag.de/downloads/category/14-vortraege-2012.html♯.

[94] P. Shiraishi, "The rare earths revolution: The dirty secret of green technologies," *ETH Zürich*, 2010.

[95] J. Lovelock, *Gaia. A New Look at Life on Earth.* Oxford University, 1979.

[96] J. Wang, W. Wang, K. Atallah, and D. Howe, "Demagnetization assessment for three-phase tubular brushless permanent-magnet machines," *IEEE Transactions on Magnetics*, vol. 44, no. 9, pp. 2195 –2203, sept. 2008.

[97] A. Gandhi and L. Parsa, "Double-sided flux-switching linear synchronous machine with yokeless translator," in *ECCE 2012*, oct. 2012.

[98] E. Tedeschi and M. Molinas, "Wave-to-wave buoys control for improved power extraction under electro-mechanical constraints," in *Sustainable Energy Technologies (ICSET), 2010 IEEE International Conference on*, dec. 2010, pp. 1 –6.

[99] ——, "Impact of control strategies on the rating of electric power take off for wave energy conversion," in *Industrial Electronics (ISIE), 2010 IEEE International Symposium on*, july 2010, pp. 2406 –2411.

[100] E. Tedeschi, M. Carraro, M. Molinas, and P. Mattavelli, "Effect of control strategies and power take-off efficiency on the power capture from sea waves," *Energy Conversion, IEEE Transactions on*, vol. 26, no. 4, pp. 1088 –1098, dec. 2011.

[101] W. Cummins, *The impulse response function and ship motions.* Schiffstechnik, 1962.

[102] J. Falnes, *Ocean Wave Energy and Oscillating Systems: Linear Interaction Including Wave-Energy Extraction.* Cambridge Univ. Press., 2002.